Technische Universität Wien

Fakultät für Maschinenwesen und Betriebswissenschaften

Diplomarbeit

Sekundärzementit - Charakterisierung und Modellierung in hypereutektoidem Stahl

im Masterstudium
Wirtschaftsingenieurswesen-Maschinenbau - Schwerpunkt Materialwissenschaften

Markus Führer

zur Erlangung des akademischen Grades eines Diplom-Ingenieurs (Dipl.-Ing.)

Die vorliegende Arbeit wurde am Institut für Werkstoffwissenschaft und Werkstofftechnologie im Forschungsbereich Werkstofftechnik durchgeführt. Diese Arbeit wurde vom Bundesministerium für Digitalisierung und Wirtschaftsstandort und der Nationalstiftung für Forschung, Technologie und Entwicklung innerhalb des Projekts Christian Doppler Labor für Grenzflächen- und Ausscheidungs-Engineering (CDL-IPE) unterstützt.

Thema:	Sekundärzementit - Charakterisierung und Modellierung in hypereutektoidem Stahl
Autor:	Markus Führer MatNr. 01426252
Version vom:	July 12, 2021
Hauptbetreuung:	Assoc. Prof. Dr.sc.ETH Erwin Povoden-Karadeniz
Mitbetreuung:	Projektass. Dipl.-Ing. Marko Vogric

Secondary cementite, characterisation and modelling in hypereutectoid steel

Markus Führer

Master Thesis

Vienna University of Technology

Faculty for Mechanical and Industrial Engineering

Institute of Materials Science and Technology

Christian-Doppler Laboratory - Interface & Precipitation Engineering

July 2021

Declaration

I declare in lieu of oath, that I wrote this thesis and performed the associated research myself, using only literature cited in this volume. If text passages from sources are used literally, they are marked as such. I confirm that this work is original and has not been submitted elsewhere for any examination, nor is it currently under consideration for a thesis elsewhere. I acknowledge that the submitted work will be checked electronically-technically using suitable and state-of-the-art means (plagiarism detection software). On the one hand, this ensures that the submitted work was prepared according to the high-quality standards within the applicable rules to ensure good scientific practice "Code of Conduct" at the TU Wien. On the other hand, a comparison with other student theses avoids violations of my personal copyright.

Vienna, July 12, 2021

(Markus Führer)

Acknowledgements

In the preamble of this thesis, I want to thank all the people who have helped and accompanied me so far in my life.

Regarding this work, first I would like to thank my supervisors Marko Vogric and Erwin Povoden-Karadeniz for continuously looking over my shoulder. You have broadened my view and encouraged me to see the big picture. I want to thank the whole department for being open-hearted and helpful from the first moment on, especially Christian Zaruba and Edith Asiemo from the laboratory at Karlsplatz for their helping hands during the metallographic analysis of the samples.

I am very pleased that I have had the opportunity to get to know a big number of amazing colleagues during my studies. I dearly hope we stay in touch in the future.

I want to thank my girlfriend Kathy for being so much more than a partner. You helped me up when I was down but always kept my feet grounded in moments of euphoria. I hope we continue taking care of each other.

Last but not least, I want to thank my family and especially my parents, who provided the basis for what I am today. You have always covered my back.

Abstract

Steel is the most often used construction material. The properties of steel can be varied in a wide range by either varying the composition or production process. These properties are influenced in a wide range by the existing microstructure. Computer-aided simulation is used to forecast these properties and to shorten the material development process. Therefore models are developed which represent reality and try to treat this issue. Providing an accurate prediction of the microstructure of an alloy is of great economic interest.

In this work, we dealt with the formation of secondary grain boundary cementite in hypereutectoid steel. Secondary grain boundary cementite is a key phase in hypereutectoid steel and has a huge influence on its properties. We wanted to give insight into the formation process of secondary grain boundary cementite and evaluate the influence of substitutional alloying elements such as Silicon, Manganese or Chromium. With the gained data from the experiments, we verified an already existing thermokinetic simulation model.

In the experimental part of this research, we carried out a systematic heat-treatment procedure. We analysed the gathered microstructure in the metallographic laboratory. We classified the microstructure and evaluated the growth kinetics of the secondary cementite. In the theoretical part, we validated the existing model with the gained data from the experiments. We classified the model on its accuracy in predicting reality. We were looking for explanations for deviations between model and reality.

In the physical experiments, we found out that cementite formation follows an exponential growth till it reaches saturation. Alloying elements, such as Silicon, Chromium or Manganese, influence the continuity of the secondary grain boundary network or retard the nucleation and growth of cementite to later times and therefore strongly influence the growth kinetics. Our research showed that cementite growth stops before it reaches the equilibrium fraction and that further growth stagnates.

The validation of the simulation results with the experiments showed that the simulation is accurate for less complex steel. We also saw that substitutional alloying elements lead to a retardation of the cementite formation. The simulation results exceeded the values of the experiments by a factor of two.

Further research on this topic can be done by executing additional heat treatments with different alloy compositions or accomplishing a material analysis of the samples with energy dispersive X-ray analysis (EDX) or electron energy loss spectroscopy (EELS). One should aim to increase the understanding of the influence of the alloying elements and the trajectories of the atoms of the substitutional alloying elements during the transformation process.

Contents

List of Figures

List of Tables

ACRONYMS

EELS electron energy loss spectroscopy

EDX electron dispersive X-rax spectroscopy

SEM scanning-electron microscopy

w% weight percent

C chemical element carbon

V chemical element vanadium

Cr chemical element chromium

Si chemical element silicon

Cu chemical element copper

Ni chemical element nickel

Nb chemical element niobium

Mn chemical element manganese

Co chemical element cobalt

Zn chemical element zinc

Al chemical element aluminum

B chemical element boron

N chemical element nitrogen

Ta chemical element tantalum

Ti chemical element titanium

P chemical element phosphorus

bcc body-centered cubic

fcc face-centered cubic

$\mathbf{T_{SC}}$ temperature during heat treatment in the dilatometer to grow secondary cementite

$\mathbf{t_{SC}}$ duration of isotherm for building secondary cementite

γ iron phase austenite

SC secondary cementite

GOC grade of completeness of the cementite grid

$\mathbf{T_{aust}}$ temperature during the autenitisation annealing

$\mathbf{t_{aust}}$ duration of austenitisation annealing

$\mathbf{t_H}$ duration of homogenisation annealing

$\mathbf{Fe_3C}$ chemical formula for cementite

Calphad calculation of phase diagrams

α greek letter alpha

γ greek letter gamma

SC secondary cementite

GUI graphical user interface

CDL-IPE Christian Doppler-laboratory - interface- & precipitation engineering

1 Introduction

Steel is still the most important material in a continuously evolving world. In 2018 more than 1,8 billion tons of crude steel were produced all over the world, which makes it the most often used metallic raw material[10]. Steel has laid the foundation for our modern world and accompanied the industrial evolution like no other material. The world we are living in would be crucially different without steel and its alloys. The reason is on one side its huge varying characteristics, only depending on the composition of the alloying elements and the applied treatment. On the other side, steel is very attractive for usage as a construction material due to its high cost-effectiveness and availability. The dependence of the properties on the composition and heat treatment make it necessary to understand the underlying mechanisms. In some cases, even nowadays, knowledge about the emerging characteristics is more phenomenological than based on accurate prediction. In order to avoid this and to increase the quality of the predictions, thermodynamic models are developed.

The goal of this work is to help increasing the understanding of the formation of secondary grain boundary cementite in hypereutectoid steels. We wanted to verify the predictions from the simulation with MatCalc with the results from experiments. We reviewed experimentally observed trends and their consistency. The phase fraction and thus the secondary grain boundary cementite film thickness were of special interest. We, therefore, heat-treated four alloys with two different isothermal reaction temperatures. The used steel alloys contained about 1 w% C and were grouped into two main categories. The first one was technologically used in the railway industry and had a wide range of different alloying elements, containing at least in small amounts Cr, Mn, Si, V, Nb, Ni and Cu. The second was a model candidate to investigate the role of Cu for phase transformation in hypereutectoid steel containing only Cu and Mn next to Fe and C. The specimens were metallographically prepared and analysed with optical and electron microscopes. We used the gathered data of the growth kinetics to verify the simulation results performed in MatCalc. For the simulation with MatCalc, we assumed a nucleation and growth approach. We made a comparison between the experimental results and the simulation results in MatCalc in terms of accuracy and confirmability.

1.1 Problem Definition

Steel is an alloy containing up to a wide range of different alloying elements. Iron provides the basis. The properties are varied in a wide range by whether changing the composition or applying variable heat treatments. Hypereutectoid steel has its field of application in rails and steel for tools. This steel, with a carbon content between 0.8 w% and 1.5 w%, pleases with its high strength, hardenability and wear resistance. To achieve this characteristics a high carbon content is needed. With an increasing amount of carbon, also the amount of secondary cementite increases. Secondary grain boundary cementite, therefore, plays an important role in hypereutectoid steel. It is a hard and brittle compound, with the stochiometry Fe_3C and nucleates at the austenite grain boundaries. It leads to an increase in strength of the steel alloy mainly due to retardation of dislocation movement but also decreases the formability and increases the brittleness. Because of this negative influence on the mechanical properties of steel, it is tried to avoid or decrease secondary cementite in technologically used steel alloys. Increasing the discontinuity of the grain boundary cementite film provides another possibility for improvement in terms of minimizing the negative influence of SC on the mechanical properties of steel.

An exact simulation of the grain boundary cementite formation therefore allows a more accurate prediction of the properties. The first comparison of growth rates of secondary cementite in hypereutectoid steel between a simulation and experimental results was made by Heckel and Paxton [9]. They reported that the experimental cementite thickening would not reach the calculated diffusion-controlled growth. Ando and Krauss [11] also reported a sluggish isothermal thickening of cementite. The cementite films would only reach about one-third of the values simulated considering a diffusion-controlled growth. They also suggested that Cementite allotriomorphs would thicken by a ledge mechanism and that partitioning of Cr or Si might be the reason for the retardation. They found some evidence of a ledge-wise growth in TEM micrographs that confirmed this suggestion. Spanos et.al [8] concluded that the reason for the sluggish thickening rates of cementite allotriomorphs has to be an interfacial structure barrier to growth. They attribute the decrease in growth rate at late reaction times to an interfacial structure barrier, probably due to the ledge mechanism [12]. This was reasoned because all other possibilities had been ruled out, like soft impingement of carbon diffusion fields or a retarding influence of substitutional alloying elements. In total, there have not been performed many studies regarding the formation of secondary grain boundary cementite. The actual formation mechanism is not yet understood completely. Neither do simulation results fit with reality. All studies had in common that the cementite thickening stopped long before the value,

calculated with diffusion-controlled growth, was reached. The importance of this topic can be seen by the need for fast and correct predictions of material properties. An accurate simulation saves money, time and gains a huge benefit for the user, whereas a trial and error approach gulps a huge amount of resources.

2 Review of the literature

This chapter will provide the theoretical background for this work. Therefore I will give a general overview of the Iron-Carbon-system and especially of the metastable Fe-Fe_3C system. I will explain the characteristics of the phase cementite and the influence of substitutional alloying elements, where I will especially take the effects on hypereutectoid steels into account. Another part of this chapter is the material calculation, where the general approach (Calphad) is explained.

2.1 Iron-carbon equilibrium

Iron is the principal component of steel and therefore has a big influence on its characteristics. Iron has a fraction of 4.7% in Earth's crust and ranks in second place behind Aluminum. Alloys based on Iron are versatile due to the mixture with alloying elements and applied heat treatments[1]. Iron is a polymorphic metal and therefore occurs in different states at different temperatures. Figure 2.1 shows the different allotropes of iron and their crystallographic structure. Pure iron solidifies at 1536°C as bcc δ iron. At 1392°C iron changes it structure to fcc γ-iron. At 911°C it then again changes to bcc α-iron. The crystallographic structure of α is identical to δ. The fcc crystallographic structure is more densely packed than the bcc structure. A sudden change in volume during the phase transformation between different crystallographic structures occurs. The Curie temperature for pure iron lies at 769°C. This represents a second order phase transformation. Below that temperature ferrite is magnetic. [1]

The binary Fe-C system provides the base for all technologically used alloy steels. Carbon is the most important alloying element in steel and affects the formation and properties of the material. A general understanding of its basic features is of huge importance. Up to a carbon content of 2.06w%, the alloy is known as steel and forgeable. With further increasing content of C, it then is known as cast iron, which is not forgeable and brittle. The fraction of C influences mechanical properties in a wide range. Carbon is interstitially dissolved in Iron. Ferrite has a lower carbon solubility at equilibrium than austenite. This results from different crystallographic structures. During the transformation from austenite to ferrite the carbon is partitioned into the austenite [13]. The bcc cell is less densely packed than the fcc cell. Therefore diffusion

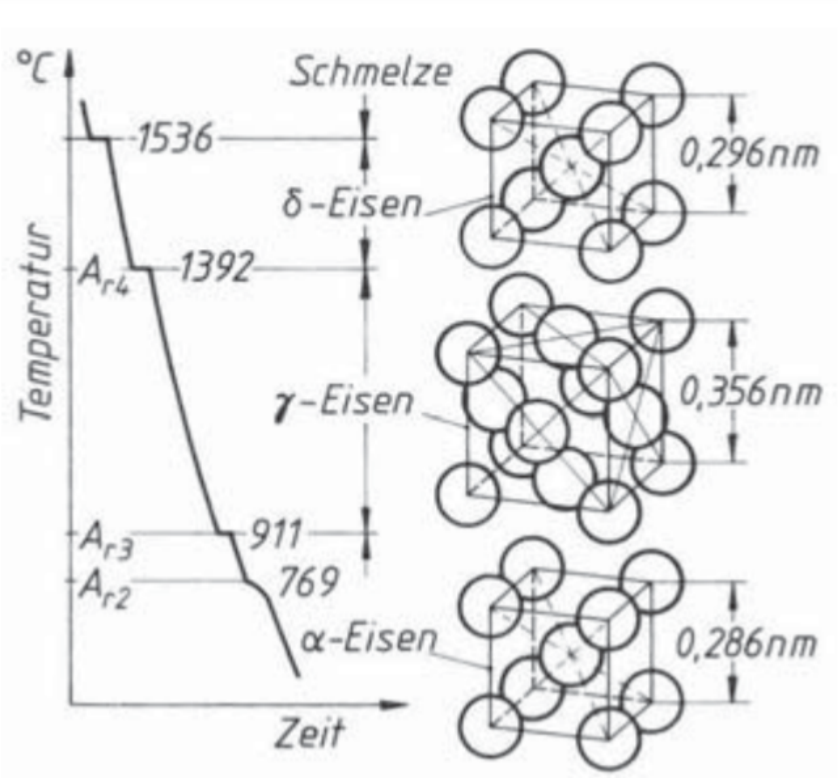

Figure 2.1: cooling curve of pure iron and its crystallographic structures [1, p.72]

of interstitial and substitutional atoms in bcc crystallographic structures is about 100 to 1000 times faster [4].

2.1.1 The metastable Fe-Fe_3C-diagram

When talking about the Iron-Carbon diagram, in many cases actually the metastable Fe-Fe_3C diagram is meant. Theoretically, under full equilibrium conditions graphite would form. But from experience, we know that cementite is the relevant phase in technologically used steel alloys. Cementite is only a metastable phase. For typically used steels, with 0.03-1.5w% C, graphite would form only after long annealing treatment. The metastable Fe-Fe_3C-diagram is the relevant one for nearly all types of steel. For systems with a higher fraction of carbon, such as cast iron, the Fe-C diagram has a higher relevance. A distinction in the field of application exists [3, chapter 8]. The relevant diagram regarding this topic is the metastable Fe-Fe_3C-diagram, which will be dealt with in the following. Its phase boundaries change with substitutional alloying elements. The gradient of temperature during phase transformation also plays an important role in its shape. Figure 2.2 shows the metastable Fe-Fe_3C-Diagram. The microstructure will change with a variation of C. The relevant area for this work is the hypereutectoid area with more than 0.8w%C.

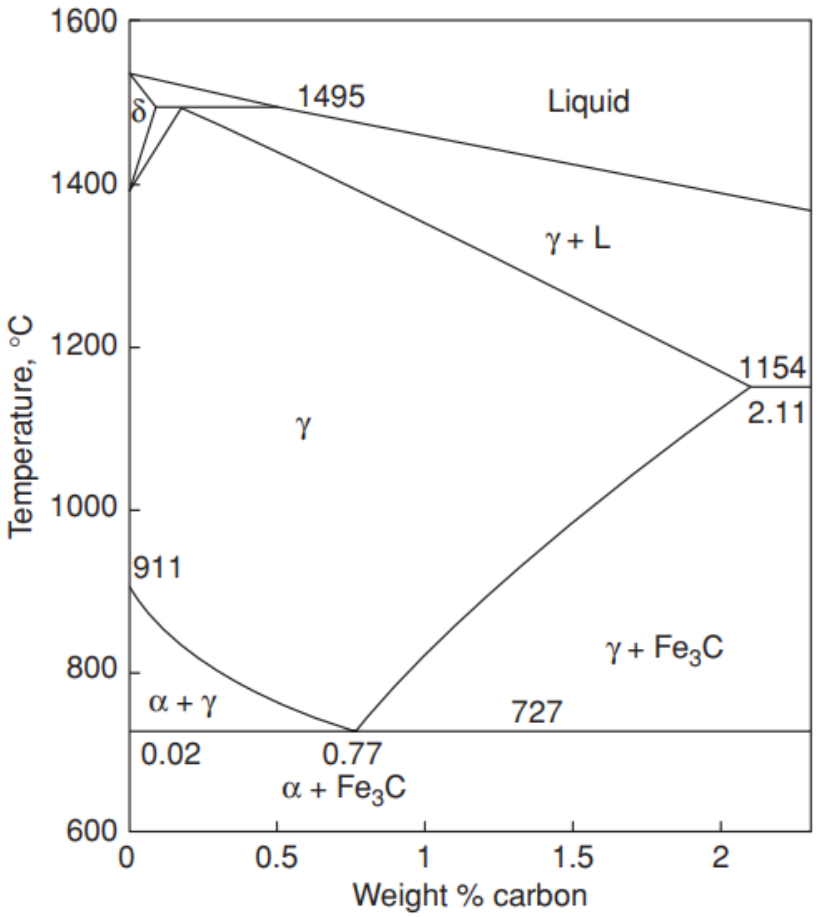

Figure 2.2: metastable Fe-Fe_3C-diagram [2]

I will now shortly describe the evolution of the microstructure of hypereutectoid steel during cooling down. Figure 2.3 shows schematically the development of hypereutectoid steel. At the starting point in the γ phase field we have 100% austenite under

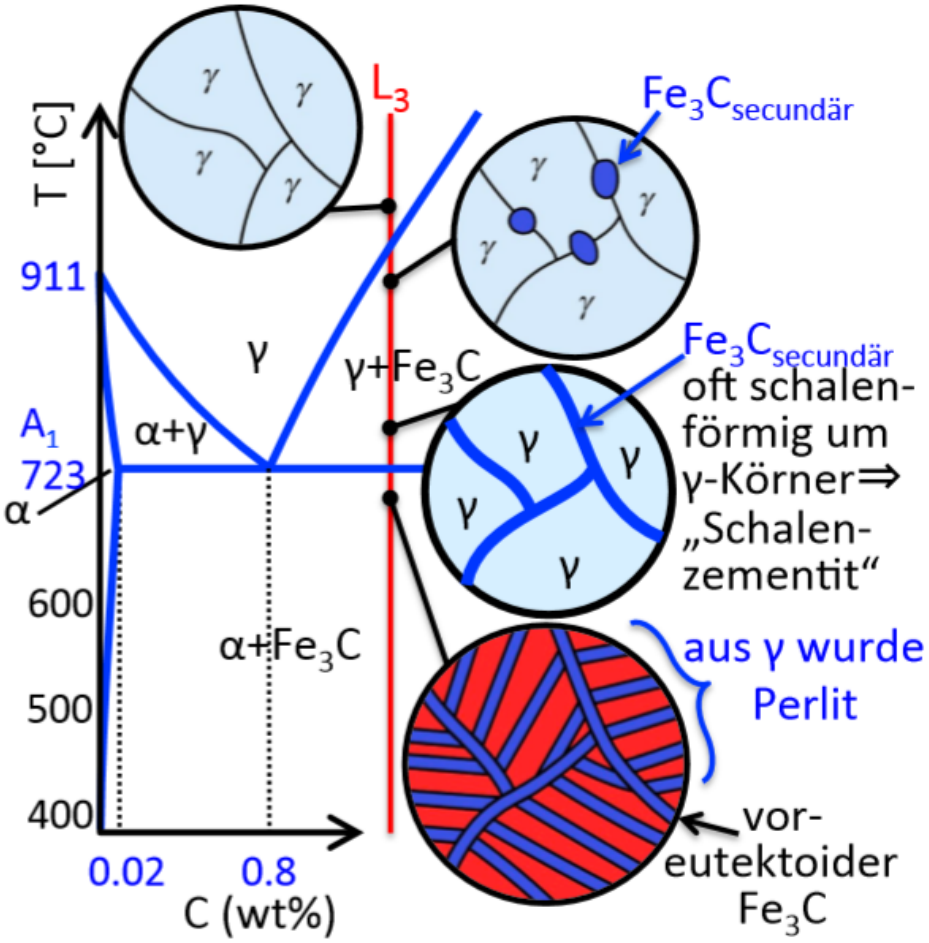

Figure 2.3: evolution of the microstructure in hypereutectoid steel[3, chapter 8]

equilibrium condition. With decreasing temperature, the solubility of C also decreases. After reaching a certain temperature the austenite is saturated by carbon and carbon is consequently partitioned in the subsequent cooling. A grain boundary cementite film forms, wrapping the austenite grains. With further progress the cementite fraction increases and the amount of carbon in the austenite decrease following the line S-E (see Figure 2.4) till it reaches the eutectoid point, which lies for unalloyed steel at 723°C and 0.8w%C[14, S.41]. Various values varying narrowly about 0.8w% are reported and accepted, respectively for the temperature 723°C. At the A1 temperature, the remaining austenite transforms into pearlite. At room temperature, the microstructure of hypereutectoid steel consists out of pearlite surrounded by grain boundary cementite[1, S.81].

2.2 Cementite Fe_3C

There are some investigations using cementite based material. In this work cementite as an intermetallic phase in steel will only be investigated. Cementite (Fe_3C) has an orthorhombic unit cell containing 12 Fe and 4 C atoms. It is metallic and ferromagnetic with a Curie temperature of about 187°C. The properties of cementite are mostly anisotropic[15]. Cementite is hard and brittle (800HV). With increasing cementite fraction in steel the tensile strength increases and the ductility decreases[p.181 4].

Cementite can be classified from which phase it forms. Primary cementite forms out of the liquid phase in cast iron with more than 4.3w%C. Secondary Cementite (SC) forms in hypereutectoid steels with more than 0.8w%C from the austenite phase. Tertiary cementite forms from the ferrite phase in steels with less than 0.8 w%C, due to the lower solubility of C in ferrite at lower temperatures. SC is the type forming in hypereutectoid steel. Fe_3C always nucleates at austenite grain boundaries [16] and forms in a temperature range above the eutectoid temperature but below the A_{cm} line S-E, Figure 2.4. Figure 2.4 shows an overview of the different types and their emergence in a Fe-Fe_3C-diagram.

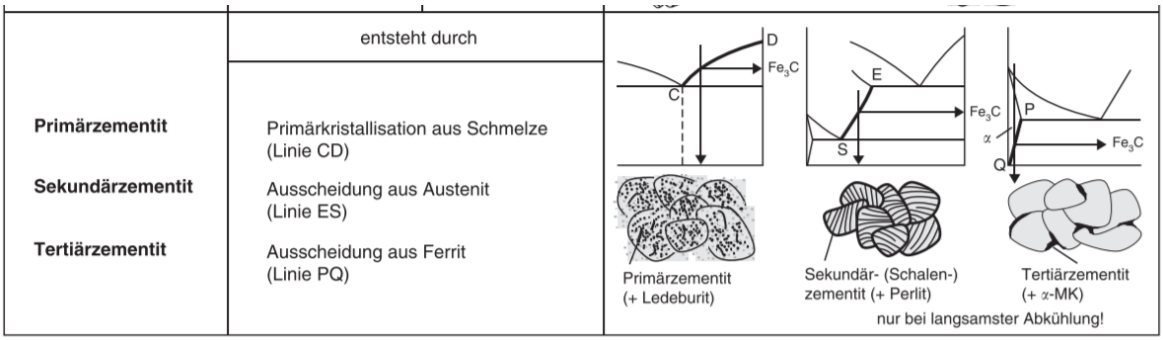

Figure 2.4: classification of cementite [4, p.178]

Aaronson [17] modified a classification system developed from Dube [18] for SC morphology. In this work a distinction between grain boundary cementite, which forms a film at the austenite grain boundaries and Widmanstätten cementite, which forms as plates or laths inside the grain, is made. There it is suggested that Widmanstätten cementite not only nucleates at austenite grain boundaries but also forms intragranularly. Spanos and Kral [12] reported that cementite would always precipitate at the grain boundary. Only when analysing in a 2D intersection plane the structure seems to be intragranularly. It was also found in 3D that grain boundary proeutectoid cementite nucleates at austenite grain corners and edges and then grows along the grain edges. The further growth of Fe_3C is dendritic along the grain boundary.
Widmanstätten cementite would nucleate at the austenite grain boundary or at already existing grain boundary cementite. Widmanstätten cementite especially forms

at higher cooling rates or lower isothermal reacting temperatures and short durations[4, p.180].

2.3 Hypereutectoid Steel

Hypereutectoid steels have a carbon content between 0.77 w%C and approximately 1.5 w%C, which is the limit for carbon solubility in austenite [19]. These steels are typically used for the production of tools for metal forming or rails. Hypereutectoid steel reaches a high strength via hardening followed by a tempering step, but also tends to be brittle[20]. The main requirements for hypereutectoid steels are high strength, hardenability and wear resistance[21]. When using steel as a material for rails, it has to fulfil special requirements, because of fast and heavy axle loads. Structural integrity, wear resistance, weldability and cost efficiency are some of the needs[22]. Figure 2.5 shows a typical micrograph of hypereutectoid steel with pearlite and grain boundary cementite at the former austenite grain boundaries. It is a hard and brittle compound,

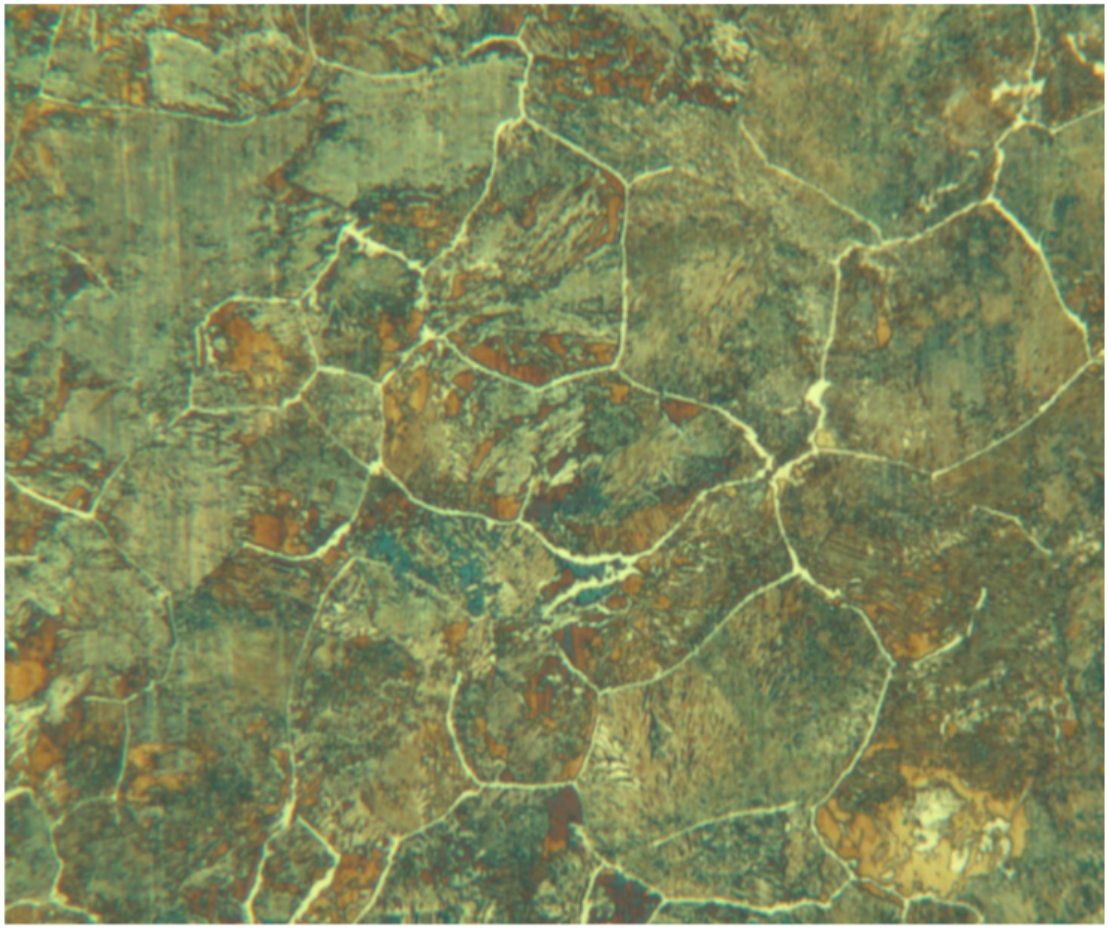

Figure 2.5: micrograph of hypereutectoid steel, pearlitic grains surrounded by grain boundary cementite (white) [3, chapter 8]

with the stochiometry Fe_3C and nucleates at the austenite grain boundaries. Secondary grain boundary cementite in hypereutectoid steel leads to an increase in strength of the steel alloy mainly due to retardation of dislocation movement but also decreases the formability and increases the brittleness. Because of this negative influence on the mechanical properties of steel, it is tried to avoid or decrease secondary cementite in technologically used steel alloys. Increasing the discontinuity of the grain boundary cementite film provides another possibility for improvement in terms of minimizing the negative influence of SC on the mechanical properties of steel.

2.4 Substitutional alloying elements

Alloying elements have a big influence on steel and its properties. Alloying elements influence the relative free energies of relevant phases. This affects the transformation processes and also leads to the occurence of new phases. Besides the influence on thermodynamics, the change in kinetics tends to be a much more complex interaction. For example, the partitioning of alloying elements leads to retardation of transformation processes. The influence of a single substitutional alloying element does not sum up when mixed with others. A comprehensive discussion of the influence of a certain element in an alloy is impossible. But it is possible to describe some generic effects. This will, especially in multicomponent systems, only be simplifications, but still provides basic insights. Modern-day thermodynamic simulations allow to calculate the phase diagram even of multicomponent system and give insight into the kinetics of phase transformations. Understanding the general influence of an element is useful. The following classification of substitutional alloying elements is orientated on Bhadeshia [14].

2.4.1 Influence on the α and γ phase field

Wever [5] classified alloying elements on their influence on the austenite and ferrite phase field, in binary mixtures. Wever [5] splits it up into four categories.
Figure 2.6 **a**): Elements such as Ni,Mn or Co open up the γ-field. The temperature where austenite transforms into ferrite is lowered. If the concentration is high enough the formation of ferrite can be completely suppressed. These elements are used in austenitic steels.
Figure 2.6 **b**): C, Ni, Cu or Zn expand the γ-field but the range of their technological use is restricted.
Figure 2.6 **c**): Cr, Al, Ti, Si or V restrict the area where austenite is stable and stabilize ferrite. In this case, the formation step from γ to α is prevented. The γ-field appears

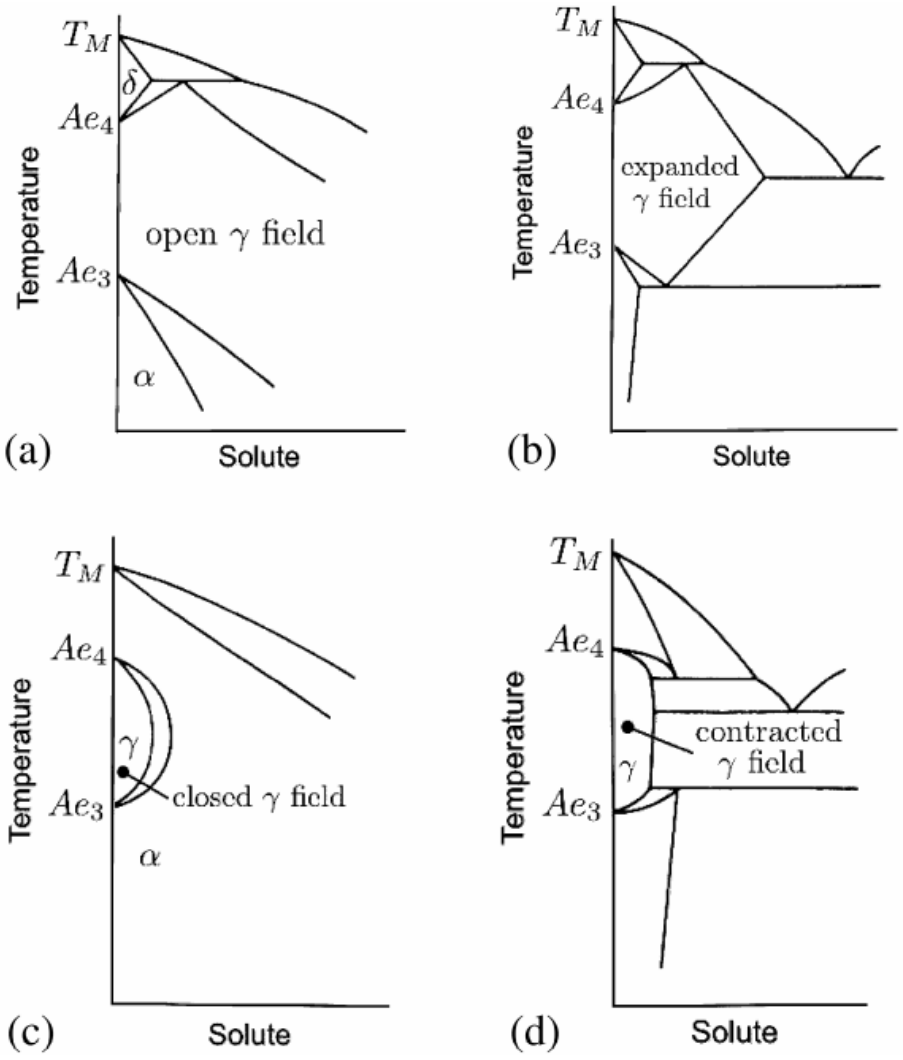

Figure 2.6: influence of alloying elements on austenite and ferrite phase field, **a**) open γ-field e.g.**Ni, Mn, Co**, **b**) expanded γ-field e.g.: **C, Ni, Cu, Zn**, **c**) closed γ-field e.g.**Cr,Al,Ti, Si, V**, **d**) contracted γ-field e.g. **Nb,Ta, B** [5]

narrow in the diagram.

Figure 2.6 **d**): Nb, Ta, B contracts the γ-field.

Following this, a subdivision in elements that stabilize ferrite (**case c,d**) such as Nb, Ta, B, Cr,Al, Ti, Si or V and austenite stabilizers (case **a,b**) such as Ni, Mn, Co, C, Ni, Cu or Zn can be made [4]. The resulting change on the eutectoid point has an important effect on the properties of the alloy. Figure 2.7 shows the influence of

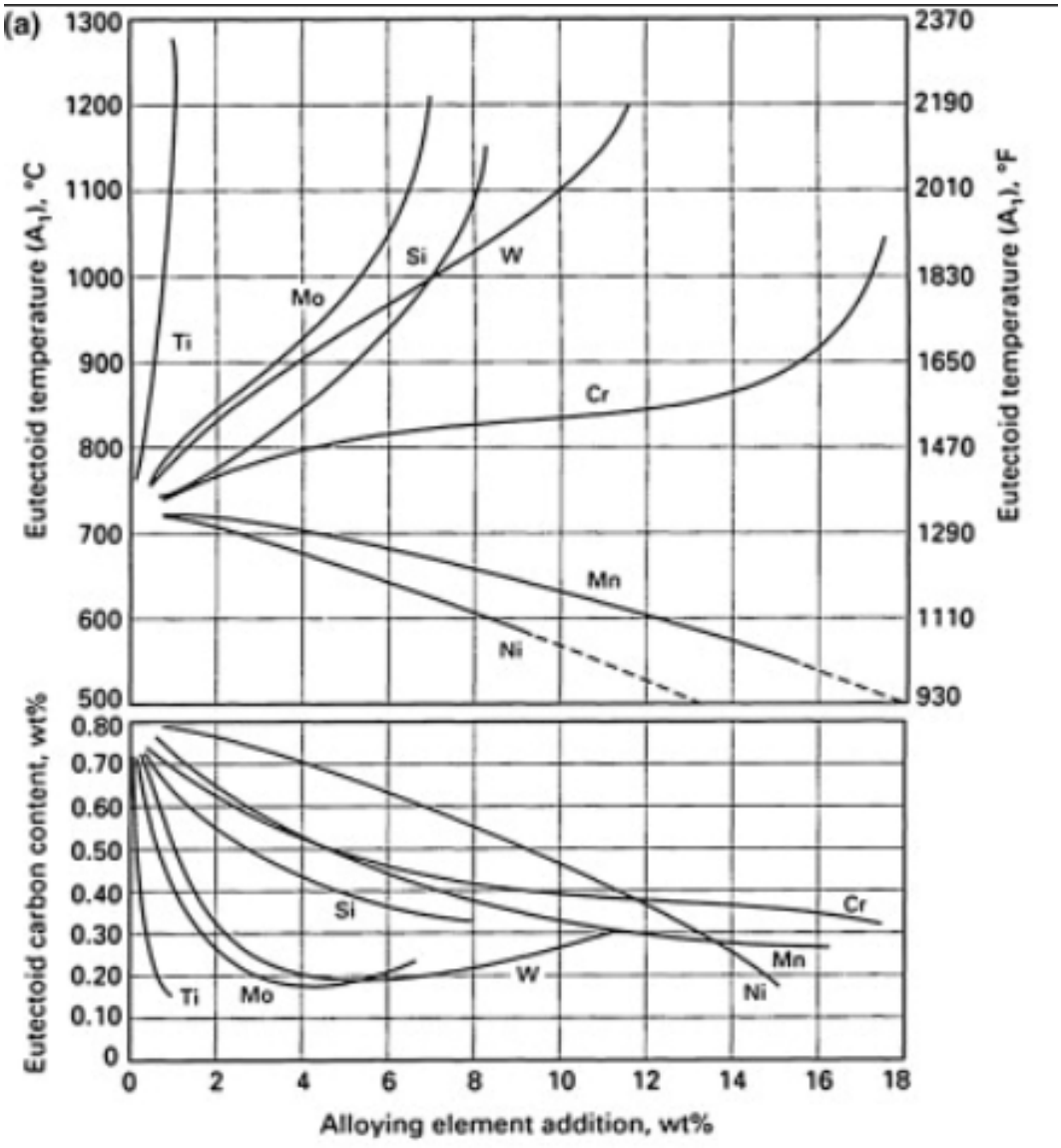

Figure 2.7: influence of alloying elements on eutectoid point [6]

different substitutional alloying element concentrations on the eutectoid point.

2.4.2 Distribution of alloying elements in steels

Another classification of alloying elements is made upon their behaviour whether they are found in solid solution in the ferrite phase or form carbides. Substitutional alloying leads to a decrease in carbon diffusion, which increases the hardenability of steel. Solid solution strengthening plays a minor role in terms of mechanical properties. Solid solution has a bigger influence on corrosion resistance or the formation of certain phases[4, p.229]. The important parameter regarding this effect is the solubility of a certain element in the matrix. Bhadeshia [14] classified into three categories:
(a): elements which enter only the ferrite phase, e.g. Ni, Cu, P, Si
(b): elements that form stable carbides and also enter the ferrite phase, e.g. Mn, V, Ti, P, W, Mo, Nb.
(c): elements that enter only the carbide phase, e.g.N

Elements such as Ni or Si are found in solid solution in the ferrite phase and have a low solubility in cementite or carbides. The elements of category **b** go in solid solution or form carbides, depending on the concentration. The carbide-forming elements (**b,c**) play an important role in the precipitation hardening of steel. Carbides are very hard and hinder dislocations to move. Appropriate heat treatments lead to fine dispersion of the carbides in the matrix and high strength, wear resistance and hardness[p.230 4]. Nitrogen plays an important because it builds carbo-nitrides, which are again extraordinary hard and increase wear resistance. Nitrogen forms hard nitrides with other alloying elements such as Ti, Al or Cr [23].
Binary phase diagrams can only give a rough overview of the encountered phases. Modern-day computer-based methods allow the simulation of ternary and multicomponent systems for a certain composition over a wide temperature range. This provides a more accurate prediction of the obtained system.

2.4.3 Effect of alloying elements on the kinetics of the γ/ α transformation

The transformation from austenite to ferrite plays an important role in technological heat treatment. Alloying elements influence the eutectoid point. In particular the diffusion of carbon is retarded. That leads to slower phase transformation for most of the alloying elements. The formation of bainite and martensite is achieved easier due to slower diffusion. The time-temperature transformation curve is displaced towards longer transformation times. Cobalt and Aluminum accelerate the transformation and therefore lead to shorter transformation times [24], [14].

2.4.4 Effect of alloying elements on the formation of secondary cementite in hypereutectoid steel

In the following, we will summarise the available literature on the influence of different alloying elements on the formation of SC. The addition of **Vanadium** leads to discontinuities of the grain boundary cementite. The secondary grain boundary cementite film is much more often broken in steel containing Vanadium than similar steels without Vanadium. Another effect of the addition of Vanadium is a decrease in austenite grain size, which leads to an increase in grain boundary area. Grain refinement leads to an improvement of mechanical properties[25]. Several alloying elements also influence the formation of globular cementite, similar to what appears after soft annealing. Ashida et al. stated that **Cobalt** suppresses the proeutectoid cementite. They referred this behaviour to the limited solubility of cobalt in cementite [24]. Zhang et al.[26] investigated the influence of **Manganese**, **Silicon** und **Chromium** on their solubility in cementite and the coarsening of cementite in hypereutectoid steels during austenitisation. Silicon breaks the grain boundary cementite up and spheroidises it. Manganese and Chromium retard the spheroidisation of cementite lamellae. The volume fraction of cementite decreases with increasing austenitisation duration. Silicon accelerates this process, whereas Manganese and Chromium retard it. The carbide forming elements Mn and Cr retard the coarsening of cementite and lead to grain refinement. Nakana et al.[27] reported that **Vanadium** and **Molybdenum** retard the formation of globular cementite. Beswick [28] described that **Chromium** in 1%C bearing steel would lead to grain refinement. Kim et al.[29] reported retardation of spheroidisation of cementite with increasing concentration of **Silicon**. The reason for this behaviour tends to be an increase of cementite volume fraction during austenitisation which leads to an incomplete spheroidisation. Kozeschnik and Bhadeshia [30] explain the retarding influence of **Silicon** on the cementite formation in austenite due to the trapping behaviour of cementite under paraequilibrium conditions. This leads to a decrease in free energy, which is the reason for the retardation of the transformation velocity. Yi et al. [31] declare that **Aluminum** accelerates the creation of spheroidised cementite in eutectoid steel. Al, a ferrite stabilising element, increases the eutectoid temperature and decreases the interlamellar spacing of pearlite.

2.5 Materials simulations of phase transformations

Material simulation plays an important role in modern-day materials science. Nowadays computational processing power has led to new possibilities in simulation processes. Cellier [32] defined a simulation as a replication of reality, where reality would

be too complex to analyse analytically. The simulation is carried out in a model. The choice of the right model and the definition of the parameters set the track for success. Phase transformation can only occur if two conditions are fulfilled. Motivation of the system to form a new phase and mobility of elements participating in the transformation. Mobility means the ability of the atoms to move in their environment, which is described as diffusion by Fick [33]. The motivation for phase transformation means the difference in free energy, as described in subsection 2.5.1.
Pippard [34] defines equilibrium as a state, where no further change would be perceptible, regardless how much time passes by . Meaning that, even with a non-zero driving force, transformation can stop.
In material simulations, differentiation between two different types of equilibrium, so-called ortho- and paraequilibrium, is made [35]. Under orthoequilibrium conditions, a full equilibrium of all elements is assumed. Paraequilibrium on the other hand is a form of constrained equilibrium. Substitutional elements stay in their position in the matrix whereas carbon atoms achieve a uniform chemical potential[36, p.120].

2.5.1 Gibbs Energy, G

Under the condition of the second law of thermodynamics, a process will only be carried out spontaneously if the overall entropy increases. The Gibbs energy, G, is a quantity that describes the energy of isobaric systems [37]. G is defined as follows:

$$G = H - TS \tag{2.1}$$

With H being the enthalpy, T the temperature and S the entropy of the system. Partial derivations of G deliver -S, the volume V and the chemical potential μ. The change of Gibbs free energy, $\triangle$G, predicts in which direction a change may lead. A $\triangle$G of a system is equal to zero points out that the states are in equilibrium and no change will be seen. The state with a lower value G will be the stable one[38, p.25]. Applying this to materials simulation gives us the knowledge to describe phase stabilities and driving forces. The stable phase after mixing two components can be evaluated via the common tangent construction method if the G of the single phases is known. Figure 2.8 shows the tangent construction applied on a binary alloy with the individual Gibbs energy curves for the three phases in the Gibbs energy/mole fraction diagram(G-X). The phases α and γ have stable regions, but the phase β does not. The chemical potentials can be read at the vertical y-axis.

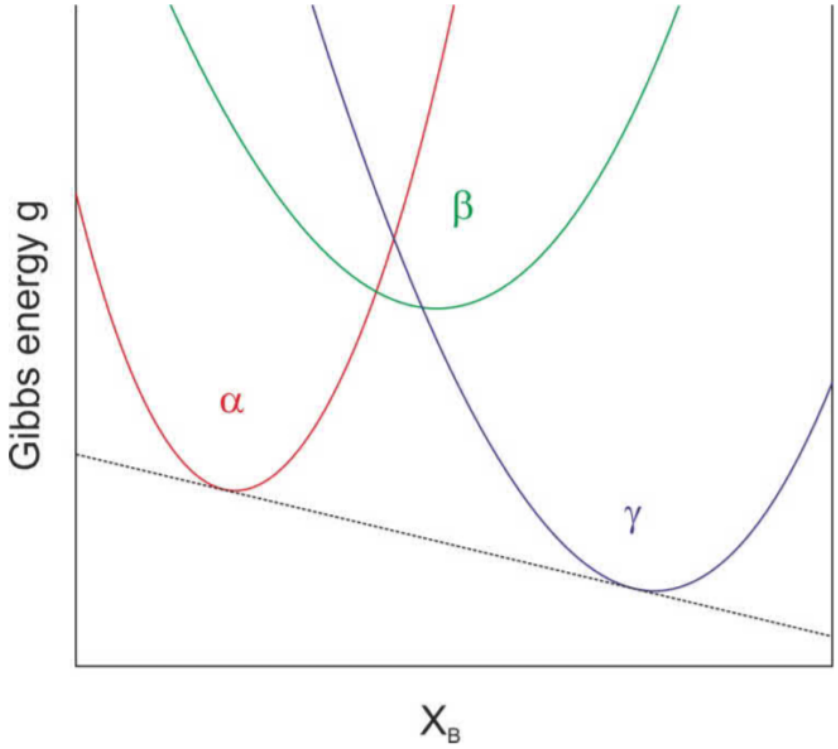

Figure 2.8: Gibbs energy in a binary A-B alloy with three possible phases [7]

2.5.2 Calphad

Calphad, literally calculation of phase diagrams, is nowadays the standard approach for material simulations. It provides a powerful framework for the numerical calculation of phase equilibria, especially for multicomponent systems. In the previous subsection 2.5.1, simplified binary systems were discussed, where the equilibrium composition could be evaluated via the tangent construction in a G-X diagram. The Calphad approach takes the complex chemical interactions of real thermodynamic systems into account. The molar Gibbs energy of a general solution can be described as the sum of the molar Gibbs energy of an ideal solution, g_{is}, and the excess Gibbs energy, g_{ex}.

$$g = g_{is} + g_{ex} \tag{2.2}$$

g_{is} represents the Gibbs energy of an ideal solution. Between the atoms in an ideal state, no mechanical or chemical interaction occurs. Thus the solution of A and B is completely stochastic. In relation, g_{ex} describes the Gibbs energy of a solution in excess of what it would be if it were ideal[37].

These terms stem from the influence of magnetism, chemical interactions or short-range ordering effects. The necessary data are stored in databases. The parameters of

the model can be easily optimised by thermochemical experiments. Gathering data for improving the model can be gained from simple binary or ternary systems. From this fundament predictions of the thermodynamics of higher order system can be made. Accurate databases, therefore, provide the basis for good simulations [39].

2.5.3 Ledge-wise growth

Spanos et al. [8] claimed that the lengthening rates of proeutectoid cementite in the experiments observed in their work would lie several orders of magnitude below the predictions made by Zener and Hillert [40], [41]. They stated that the interface structure needs to be taken into account and that such an interfacial structure barrier could be a reason for the difference in the cementite thickening between simulation and reality. They showed under the assumption of ledge-wise growth that a small value of h/λ (Figure 2.9) could explain the interfacial barrier to SC thickening. Equation 2.3 shows the overall growth rate of a planar interphase boundary advancing by the lateral migration of ledges [42], [43]. h, λ and V_s are the ledge height, ledge spacing and step velocity, respectively.

$$G_L = \frac{h}{\lambda} V_s \tag{2.3}$$

Figure 2.9 shows a two-dimensional representation of the ledge-wise growth mechanism, with G_L representing the overall growth rate. Ando and Kraus [44] stated, following

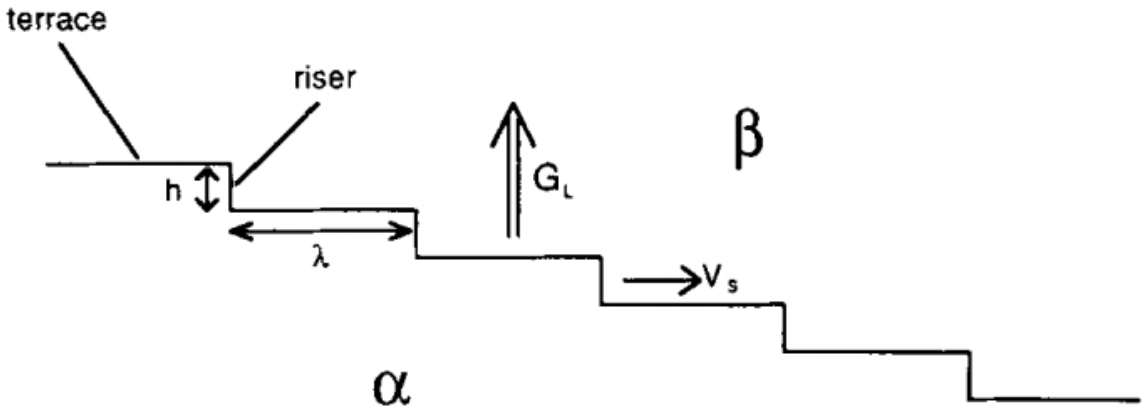

Figure 2.9: schematic illustration (two-dimensional) of growth by the ledge mechanism: G_L = the overall boundary migration or growth rate; V_s = the individual lateral ledge velocity; h = the ledge height; λ = the interledge spacing; α = the precipitate phase; β = the matrix phase [8]

their ledge growth calculations, that an increase in interledge spacing (λ) could only be partially responsible for the observed sluggish cementite grain boundary film growth kinetics. Combining the results from the experiments in this work and the results regarding retardation by the ledge-mechanism from other authors [44], [8], [12] we

suggested that the ledge-mechanism, at least partially, contributes to the stagnating grain boundary cementite growth kinetics.

Spanos et al. [8] stated that soft impingement (diffusion field overlap), another possibility for the discrepancy between simulation and reality, does if any only play a minor role and therefore can be neglected.

3 Methods

In the following chapter, the used approach for a deeper understanding of cementite evolution will be explained. After executing heat treatment experiments, the specimens were metallographically analysed under the use of an optical and a scanning electron microscope. We performed thermokinetic simulations and validated the simulation results with the experiments.

3.1 Material

In the following chapter 3.1, the chosen material will be presented. The positioning of the samples within the raw material and the preparation of the samples will be explained. All the results will be presented in chapter 4.

The used materials are hypereutectoid alloys with more than 0,8 w% C and additions of other alloying elements. The constituent elements are listed in Table 3.1.

Table 3.1: composition of the alloys, given in w%

alloy	C	Cr	Cu	Mn	Nb	Ni	Si	V
FeCu1	1,2		0,5	1				
4-1	1,01	x	x	x	x	x	x	x
FeCu3	1,2		2	1				
5-2	1,055	x		x			x	x

Steels 4-1 and 5-2 in Table 3.1 represent alloys typically used in the railway industry. The exact composition of these two technologically used alloys is kept secret. The "x" in Table 3.1 mark the occurrence of an element in the respective alloy. FeCu1 and FeCu3 are model candidates to investigate the role of Cu for phase transformation in hypereutectoid steel. The material was available as railhead (4-1), forged material (5-2) and as a cast material(FeCu1, FeCu3). To distinguish the alloys, their abbreviations, as seen in Table 3.1, will be used in the following sections.

Alloy 4-1 and 5-2 have a wider range of different added alloying elements and are typically used for railheads. Alloy FeCu1 and FeCu3 have a narrower list of added

alloying elements and were specially produced for experiments in the framework of fundamental research. The alloys 4-1 and 5-2 have due to their similar composition related properties. The same can be said about the alloys FeCu1 and FeCu3.

We wanted to make a comparison between the material before and after the heat treatment, to see the influence of the applied heat treatment on the austenite grain size or inclusions. Therefore we took reference samples of each material. We evaluated the microstructure of the raw material with an optical microscope after etching with picric acid etchant and Nital. The evaluation of the size of the former austenite grains was made indirectly via the grain boundary cementite. The applied method is described in chapter 3.2.3. The results are shown in chapter 4.1.1.

The samples were taken with a cutting machine from the base material. The used cutting machine types were CUTO 20 from the company Jean Wirtz with a thickness of the cut-off wheel of 1.5 mm and Accutom 100 from Struers [45] with a cutting width of 0.5 mm. We defined the dimensions of the specimen to be quadratic with 5 mm and with a height of 10 mm. The outermost samples were taken at a 7 mm distance from the surface. From the railheads, the upper part of about 20 mm was not used because of the high applied stresses in this area, which results in inhomogeneities. The available railheads were about 20 mm thick. The cast material was available as a block of the size of 85 mm x 85 mm x 80 mm. To get an unambiguous assignment of each specimen within the basic material an identification system has been applied. In figures 3.1, 3.3 and 3.2 the position of the sample in the basic material for alloy 4-1, alloy 5-2 and the cast iron alloys are explained. The cast blocks for alloy FeCu1 and FeCu3 had the same dimension, therefore the same identification system was applied. Note the following important distinction between capital- and small letters. Capital letters mark a row inside the plane whereas small letters mark the position of the specimen in the original block depth. Uneven numbers mark the position on the left half whereas even numbers tag the right half of the sample. The expressions RU, LU, RO and LO mark the four quadrants.

While cutting the samples our main goal was, besides getting the right shape and size, to keep the material cooled in order not to influence the microstructure due to ageing effects. Therefore we kept the cutting speed low and made sure to provide water as the cooling agent. We did the cutting work with machines from the metallographic laboratory of WWWT. Before the actual heat treatment, we applied a homogenisation annealing. For alloys FeCu1 and 4-1, we made this step directly with the dilatometer. For the alloys FeCu3 and 5-2, we made the homogenisations annealing in a separate step in an vacuum oven. Therefore we primarily cut the material in cubes with a length of 10mm to decrease the number of necessary turns. Afterwards, we quartered the annealed samples of alloy FeCu3 and alloy 5-2.

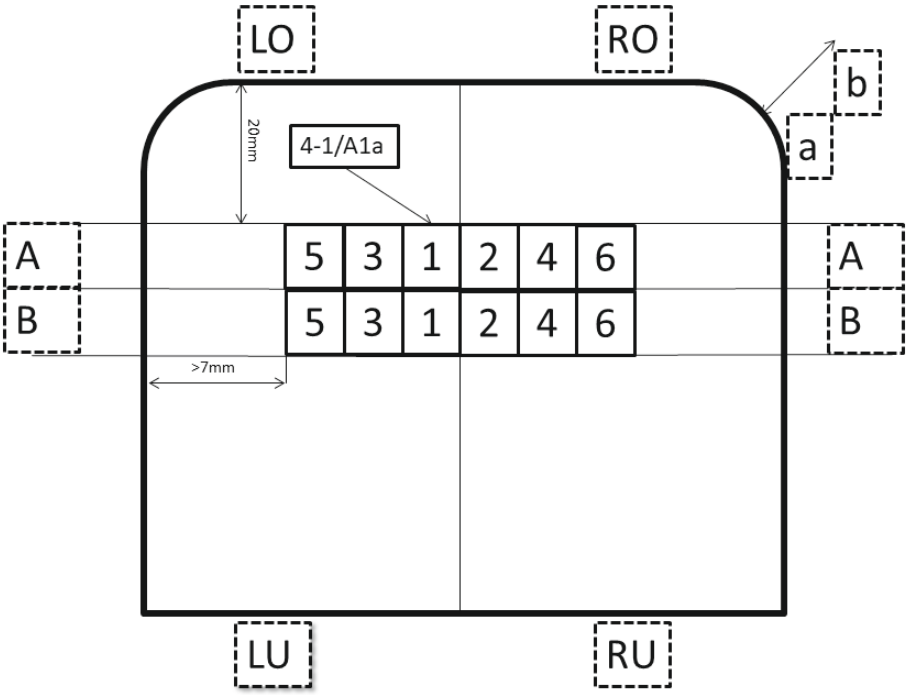

Figure 3.1: position of the samples in the railhead, alloy 4-1

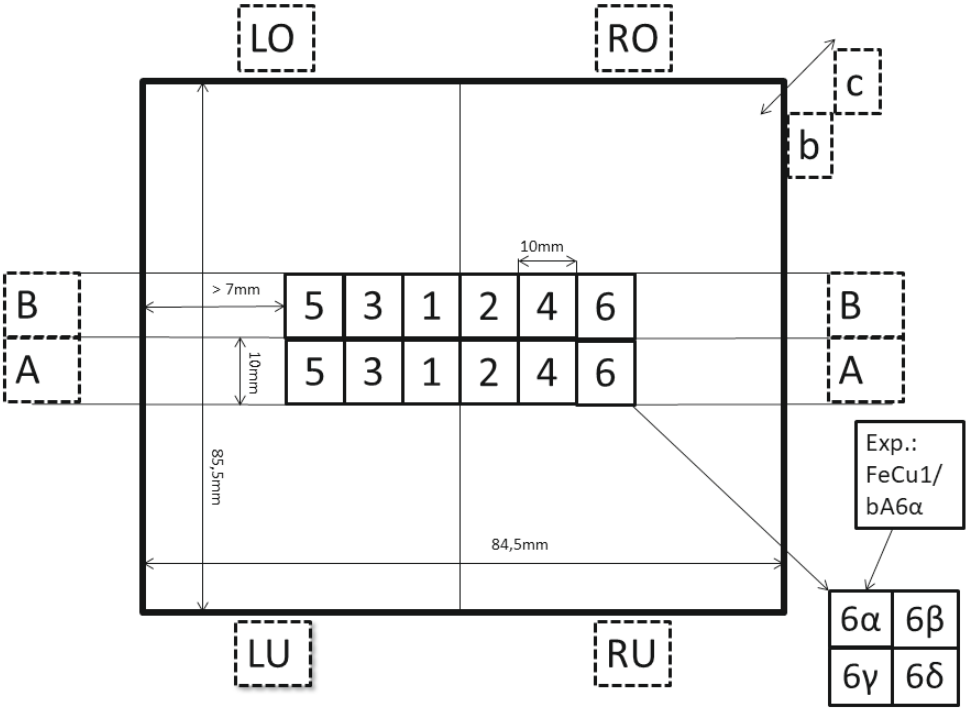

Figure 3.2: position of the samples in the cast material of alloy FeCu1 and FeCu3

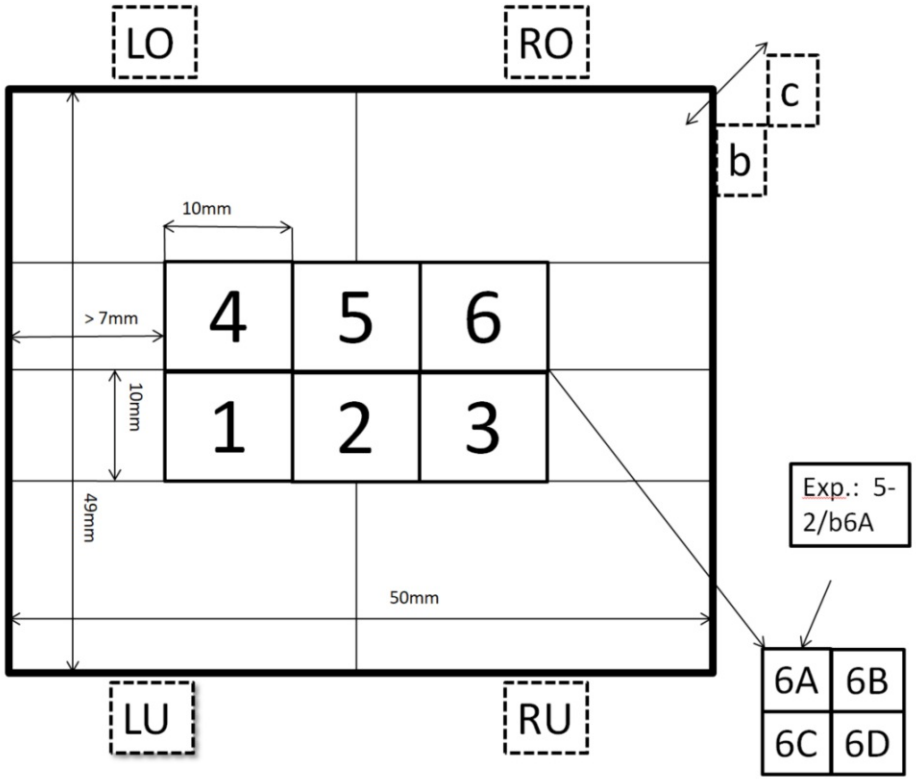

Figure 3.3: position of the samples in the railhead of alloy 5-2

3.2 Experimental setup

The experimental setup was split up into three parts. 1) preparation and heat treatment of the specimen, 2)metallographic analysis with the use of an optical microscope and SEM, and 3) analysis and examination of the gathered images. The targets of the examination were to evaluate the thickness of the *SC*, the phase fraction of the cementite and the average grain size of the former austenite grains.

3.2.1 Heat treatment

The preparation of the samples has already been explained in section 3.1 on page 19. The heat treatment was carried out in a dilatometer, type Baehr 805. The big advantage of this machine was the good temperature control which was realised via a control loop with a direct connection to the sample. The temperature control was realised via thermocouples. The thermocouples were connected with the surface by resistance welding. The sample heating was made via induction. Another big advantage of the dilatometric heat treatment was that experiments were executed under vacuum conditions, which was done to avoid interactions of the sample with oxygen and nitrogen. Figure 3.4 shows the principle experimental arrangement with the dilatometer in the vacuum chamber. The sample is in the induction coil. The thermocouples are installed.

The definition of the actual heat treatment to get the desired outcome has been an

Figure 3.4: experimental arrangement at the dilatometer

important step. The goal of the heat treatment was to provide samples with different evolution steps of secondary grain boundary cementite throughout its formation process. Afterwards, we analysed the samples metallographically and mapped the cementite formation. Hereby the grain boundary cementite film thickness and the phase fraction were the important parameters.

We took the theoretical background of hypereutectoid steel, see chapter 2.3, knowledge from former experiments and similar experiments found in the literature ([9], [11], [8]) into account to define the heat treatment parameters. In the context of published data of *SC* evolution, one of the most relevant contributions is from Heckel and Paxton [9]. To make the gathered data comparable, the time steps of the chosen isotherm for the cementite formation are similar to the time steps as in the paper from Heckel and Paxton [9] and follow a logarithmic path with 9 steps from 50 to 200000 seconds. The experiments with longer t_{SC}, 5e+04 and 2e+05 seconds, were carried out to obtain phase fraction and cementite film thickness after very long reaction times, which may be expected to approach thermodynamic equilibrium. Experiments with such long annealing have not been realised before and it is to date thus not clear when the evolution of the cementite would reach the equilibrium state.

In order to gain meaningful results from heat treatment experiments, we recommend

a careful preparation. We did a lot of preparatory work

In order to gain meaningful results from heat treatment experiments, we recommend careful preparation. We did a lot of preparatory work like reviewing phase diagrams and taking the influence of additional alloying elements into account. Before the actual heat treatment, we executed a preliminary heat treatment experiment study where we checked the parameters of the heat treatment. The chosen parameters of the heat treatment have been compared with a MatCalc prediction of cementite formation. We used stepped equilibrium calculation to evaluate the phase fraction of the occurring phases over the temperature under equilibrium conditions. We also executed a microstructure simulation to get an estimation about the expected grain size and also estimate at which temperatures cementite would start to precipitate. Further information about the approach with MatCalc is given in chapter 3.3.

Figure 3.5 shows the basic principle route of the applied heat treatments. After the

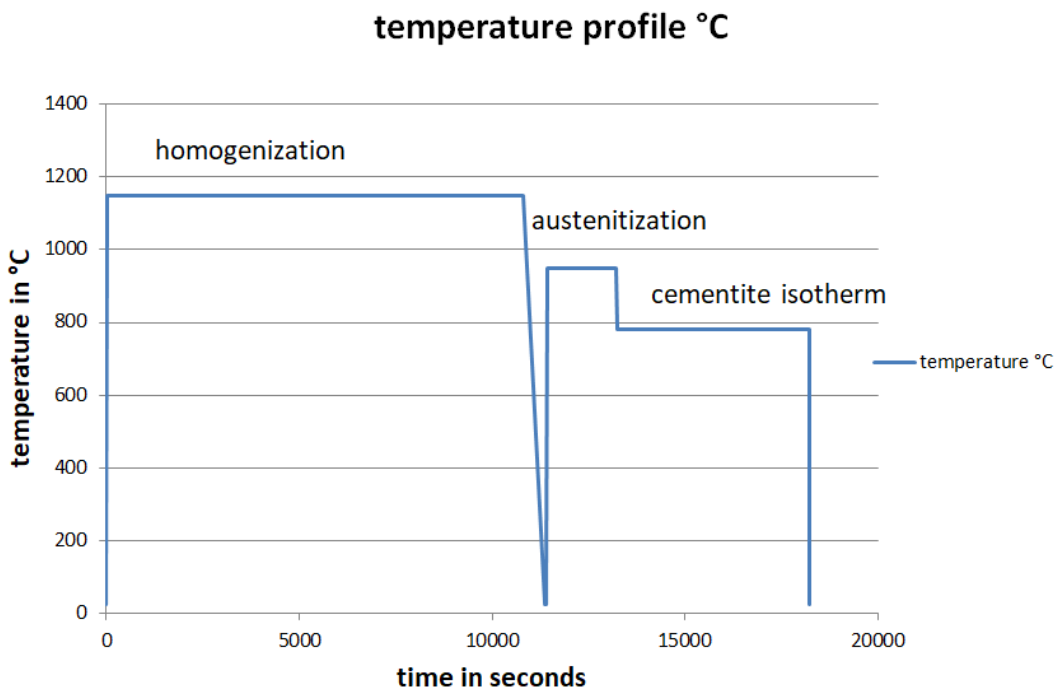

Figure 3.5: temperatur profile of the heat treatment

homogenization isotherm at 1150°C for three hours the samples are cooled down to room temperature with a cooling rate of 2 K per second. This is done to decrease the size of the grains by allowing recrystallisation. Moreover cooling has to be slow to allow the pearlite to grow. For alloys 5-2 and FeCu3, the homogenisation annealing was carried out in a separate step in a homogenisation oven. After reheating to 950°C the specimen is austenised for 30 minutes and then cooled with a rate of 15 K per second to the temperature of the cementite isotherm. The last step of the heat treatment

is for all experiments quenching to room temperature with a cooling rate of 100°C per second. We chose 100K/s because this was the fastest possible quenching rate, which allows to freeze a high temperature cementite appearance. By quenching down from the temperature of the cementite isotherm we wanted to freeze the prevailing secondary grain boundary cementite by transforming the austenite into martensite. For this quenching step Helium is used as cooling gas. The homogenisation and the austenisation step were the same for all samples. The homogenisation step was varied as described in section 3.2.1. All parameters kept constant during the heat treatment are listed in table 3.2.

Table 3.2: constant parameters of the heat treatments

shortcut	value	meaning
T_h	1150°C	temperature of homogenisation
t_h	10800 s	duration of homogenisation
dT_h/s	2K/s	cooling rate after homogenisation
T_A	950°C	temperature of austenisation
t_A	1800 s	duration of austenisation
dT_A/s	15K/s	cooling rate after austenisation
dT_c/s	100K/s	cooling rate after *SC* isotherm

Homogenisation

The homogenisation annealing has been included preliminary to the regular heat treatment. One task was to make sure that the specimens were as homogeneous as possible. This built the basis for meaningful interpretations of the tests. Experiments on the same material before this study have shown that the untreated basic material contained severe inhomogeneities. After defining the homogenisation annealing parameters we carried out some validation heat treatment experiments followed by a metallographic analysis where we checked the assumptions(see Table 3.2) regarding the homogenisation annealing.

During the definition of the homogenisation parameters, we had to make a compromise between a high level of homogeneity due to a long annealing time and a not too large grain size, as explained in the following. The average grain size increases with a longer homogenisation annealing time. After 6 hours at 1200°C, the number of grains per sample decreased to only three per polished surface. The polished area, in this case, was about 5 mm x 10 mm big. To increase the significance of the planned experiments more grain boundaries and therefore more grains were needed. For this purpose, the appropriate homogenisation annealing was defined to be 3 hours at 1150°C, representing a good compromise between grain growth and achieving a ho-

mogeneous microstructure. In the preliminary study, we found out that a temperature of 1150°C for 3 hours is adequate for the homogenisation of the microstructure. We controlled the homogeneity of the microstructure by reviewing the etched samples in the optical microscope. The resulting grain size also turned out to be smaller than 200µm. Preliminary experiments with this material have shown that due to the production process microstructural zones or bands seem to be oriented in a preferential direction. During the actual heat treatment experiments, it turned out that the homogenisation treatment reduces the zones with microstructural orientation and turns it into an equiaxed microstructure. It should be noted that the existence of carbides can be negated due to the low amounts of alloying elements. We therefore neglected the influence of carbides on the formation of SC [13, p.120].

Austenisation

The austenitisation was carried out at 950°C for 30 minutes. 30 minutes turned out to be sufficiently long to austenitise the whole microstructure and 950°C was low enough to prevent excessive grain growth. During the determining of the cementite isotherm, it was shown that at 800°C cementite would not form in some samples or that the cementite network around the austenite grains would by far not be complete even after a long annealing time. Therefore the highest eligible temperature for cementite growth was adapted to 780°C.

Isothermal reaction

The temperature and the duration of the cementite isotherm varied. Experiments were carried out at 780°C or 750°C. The hypothesis was that the driving force for cementite formation would differ sufficiently between the two chosen temperatures to observe a significant difference in the cementite thickness. The obtained results would further serve as validation data for the thermokinetic simulation of the cementite kinetics. 780°C was chosen under the assumption that cementite would form but that the temperature should be close to the thermodynamic dissolution equilibrium temperature of cementite, which is about 880°C, depend on the composition. The lower temperature was chosen to be far enough from the first one, but higher than the pearlite start temperature. In terms of duration of the cementite isotherm, we tried to define the values of annealing time by logarithmic variations. The shortest value was first defined as 10s, but this would be too short to be able to see any cementite formation. We then increased this value up to 50 seconds.

Table 3.3 shows the summary of all planed heat treatments for one alloy. The values are given in degrees Celcius, seconds and degrees Celcius per second. The majuscule

T stands for temperature and the minuscule t for time. In total we carried out 18 heat treatment experiments per alloy.

Table 3.3: planned heat treatments

count	1	2	3	4	5	6	7	8	9
T_{SC}[°C]	780	780	780	780	780	780	780	780	780
t_{SC}[s]	50	100	500	1000	3000	5000	10000	50000	200000
count	10	11	12	13	14	15	16	17	18
T_{SC}[°C]	750	750	750	750	750	750	750	750	75 0
t_{SC}[s]	50	100	500	1000	3000	5000	10000	50000	200000

Before the actual experiments were made, a preliminary study was carried out to test and to adapt the parameters of the planned experiments. In this preliminary study, we made 18 heat treatment experiments to verify our assumptions regarding the heat treatment parameters. We controlled the microstructure after the homogenization for grain size and homogeneity. The formation of cementite after an isothermal reaction annealing proved our assumptions regarding the isothermal reaction parameters to be true. The experiments 1 to 18 in table 5.1 in the appendix were part of the preliminary study.

Critical assessment of experimental route: While executing the heat treatment experiments the temperature control was not stable throughout the experiment or the applied temperature was not correct. These problems probably occurred mainly due to bad contact of the thermocouple with the surface of the sample. At first sight, the temperature control looked right, but later, during the analysis of evolved microstructures, it turned out that these would not fit with the expectations from theoretic considerations of phase stabilities and phase transformations (thermodynamic MatCalc pre-investigations). This was for example the case when pearlite occurred or no cementite at all was seen.

Especially those experiments with T_{SC} 780°C, and particularly T_{SC} 800°C (thus restricted to preliminary study) appeared to be more often problematic, which probably stemmed from the fact that 780°C is close to the temperature where cementite starts to form, and the temperature control is thus particularly critical. Experiments presenting the documented and obvious problems with T-control were then repeated. We checked the plausibility of all obtained results in the scope of the metallographic analysis. The influence of temperature control problems on remaining experiments (i.e. excluding some first problematic runs from further interpretations) is unlikely, but cannot be guaranteed. This has to be kept in mind when inconsistencies of analysed results

arise (experimental outliers). Table 5.1 in the appendix lists all the executed heat treatments.

3.2.2 Metallographic analysis

For the metallographic analysis of the samples, we followed the suggestions of Struers [45]. The specimens were prepared in a hot mounting process with the mounting media Polyfast, which is conductive and therefore can be used for SEM. In the following step, we ground and polished the mounted specimen. We had to etch the polished samples to be able to analyse them in the microscope.

We applied different etching methods, which act on different microstructural features of the material as discussed in the following. Table 3.4 shows the used etching methods, the applied temperature and the etching duration. The picric acid etchant

Table 3.4: used etching methods

etching agent	temperature[°C]	duration	reps.	intermediate step
0,5% Nital	ambient temp.	30s-60s	1-2	Ethanol
2% Nital	ambient temp.	15s	1-2	Ethanol
picric acid etchant	55-65°C	12-15 min	1-2	20s polishing
Bechet und Beaujard	ambient temp.	45s	3-5	20s polishing

contained 75ml water, 25g sodium hydroxide and 2g filtrated picric acid. Etching with picric acid etchant was done to highlight the cementite. The etching solution by Bechet and Beaujard contained 100ml of filtrated picric acid, 1,6g cupric chloride and 0,5ml Aegon wetting agent and was used to point out the former austenite grain boundaries. Different concentrations of nital solutions were used to get a quick overview of the material and its different phases and were also used as an etching method for SEM. Nital mainly removes the ferrite whereas the more stable cementite remains and protrudes from the surface. This acts as a diffraction grating and makes boundaries between phases visible[46]. Mainly Nital with 0,5% concentration was used for about 45s. If the etching was done for a subsequent SEM analysis then the duration was about 60 seconds to get a higher etching grade. For the technologically used alloys (4-1, 5-2) the duration had to be a bit longer than for the model candidates (FeCu1, FeCu3) to get a high quality of etching. In an optical microscope, the cementite appears black in a white matrix when etched with picric acid. This etching was used to evaluate the cementite fraction, the cementite thickness and indirectly the prior γ grain size. Etching with picric acid etchant was carried out at about 65°C and for about 5 to 15 minutes depending on the alloy. Etching with picric acid etchant was especially successful when the solution was made directly before etching.

The etching solution by Bechet and Beaujard was used in cases where the picric acid etching did not work to evaluate the former γ-grain size. This etching method is elaborate and quite uncertain in the quality of its outcome, therefore we tried to prioritise the other options first. This technique was required when the *SC* fraction was small. In these cases, alternative etching could not uncover the former γ-grain boundaries. This etching method was carried out at ambient temperature for about 45s with 3 to 5 repetitions [46]. During each repetition, the specimen was cleaned with ammonia to remove the copper deposits from the surface and polished for about 20s. The polishing is necessary to increase the visibility of the former γ-grain boundaries. This is why this method is quite elaborate.

In general, it is advantageous to do the etching as soon as possible after the polishing. The longer the time is between both processes, the more likely it is that a stable oxide layer forms on the surface, which then prevents effective etching. To increase the potency of the etching method it is good to quickly clean the surface with ethanol and then repeat the etching step. We noticed that etching specimens of alloy 4-1 with the picric acid solution was especially difficult and did not lead to similarly good results as for alloy FeCu1. For alloy 4-1 the delicate optimum, i.e. a compromise between too short etching time leading to low visibility of the cementite and a too long etching time leading to over-etching of the surface, associated with no visualization of microstructural features, had to be found. I would like to emphasize that etching is a difficult task. Achieving good results depends upon many different parameters, and a lot of things need to be taken into account. Experience is to date the only thing that keeps you on track.

3.2.3 Examination of the images from SEM and optical microscope

Here the general approach of the examination of the images from SEM and optical microscope will be explained. The results will be presented in chapter 4. After successfully etching the specimens we analysed the microstructure in an optical microscope and SEM. The SEM was used because of the higher possible magnification, which was particularly necessary for microstructure characterisation of the experiments with a short t_{SC} and associated resulting small size of the cementite, and of the samples of finer grained alloys 4-1 and 5-2. More precise measures of the cementite film thickness could be made in images with higher magnification and resolution, which also led to a more accurate evaluation of the film thickness. Magnification up to 1000x and 8000x was possible with the available optical microscope and SEM, respectively. Gathered images were then used for the determination of the microstructure of the samples. The

characteristics of interest were the thickness of the *SC* at the former γ-boundaries, the phase fraction of the cementite and the γ-grain size. For the grain size and the phase fraction, a lower magnification was necessary, thus optical microscopy was sufficient. The images made with SEM were mainly used for the evaluation of the thickness of the *SC*. The evaluated data from the images were used for the calculation of the thickness of the *SC* at the former γ-boundaries, the phase fraction of the cementite and the γ-grain size. For this purpose, the software packages ImageJ ([47]) and Drawboard PDF [48] were used. Image J was used to measure the thickness and phase fraction of the cementite. Drawboard-PDF was used to evaluate the prior γ-grain size. Figure 3.6 shows a typical microstructure. Here the *SC* builds an almost complete grid around the γ-grains. The matrix is martensite due to the quenching at the end of the heat treatment. For example alloy FeCu1, in Figure 3.6, was treated at 780°C for 10000s. The specimen was etched for about 15 minutes at 60°C with the picric acid etchant.

For evaluating the thickness of the *SC*, at least 60 measurements with at least three different images per sample were made to achieve statistical pertinence. The measured thickness D_{2d} was defined as the shortest connection from one side of the cementite, through the cementite to the opposite side.

$$D_{2d} = 2 * D_{3d} \tag{3.1}$$

The expression (3.1), derived from Fullman [49], shows the lineal connection through the grain boundary cementite D_{2d} in 2D and the actual thickness D_{3d} of the *SC* in 3D. This expression is only an approximation, where it is assumed that the film thickness in 3D is on average half of the film thickness in 2D.

In chapter 4 the results of the real grain boundary cementite thickness in 3D are evaluated with the use of the formula (3.2) [50]. In this formula D_{2d} is the measured thickness in 2D, D_{3d} is the evaluated thickness in 3D and R is the austenite grain radius. It should be noted that this equation assumes the grains to be spherical. This formula is derived by integrating the SC thickness on a quadrant. A solution for D_{3d} can only be derived numerically, with D_{2d} and R being the input parameters.

$$D_{2d} = \frac{2}{\pi} \int_0^{\pi/2} ((R + D_{3d})cos(asin(\frac{\sin(\theta)R}{R + D_{3d}})) - R * cos(\theta))d\theta \tag{3.2}$$

The measurements spots in the images were taken randomly with a constant distance between them. Depending on the amount of SC in the image the number of measurements varies. ImageJ then provides the measured data as a CSV file. Images from the SEM and the optical microscope are taken. For images of specimens with short t_{SC}, taking 60 measurements from one image has not been possible, because of

the low amount of cementite. In these cases, some more images were analysed. With the gathered data the arithmetic mean, the standard deviation and the necessary parameter to generate a boxplot were calculated. The graphical visualization via charts was made in EXCEL.

Besides the cementite thickness, the grade of completeness of the cementite grid, in the following sections marked with G, was also evaluated. The variable GOC is defined as follows: the grade of completeness would be 100% if every grain in the 2D intersection plane were surrounded by a film of cementite. This scaling is important in order to compare the experimental values with the outcome from the simulations in MatCalc. An example of a complete grid of cementite surrounding the γ grains is figure 3.6. For the time being, GOC needs to be evaluated manually.

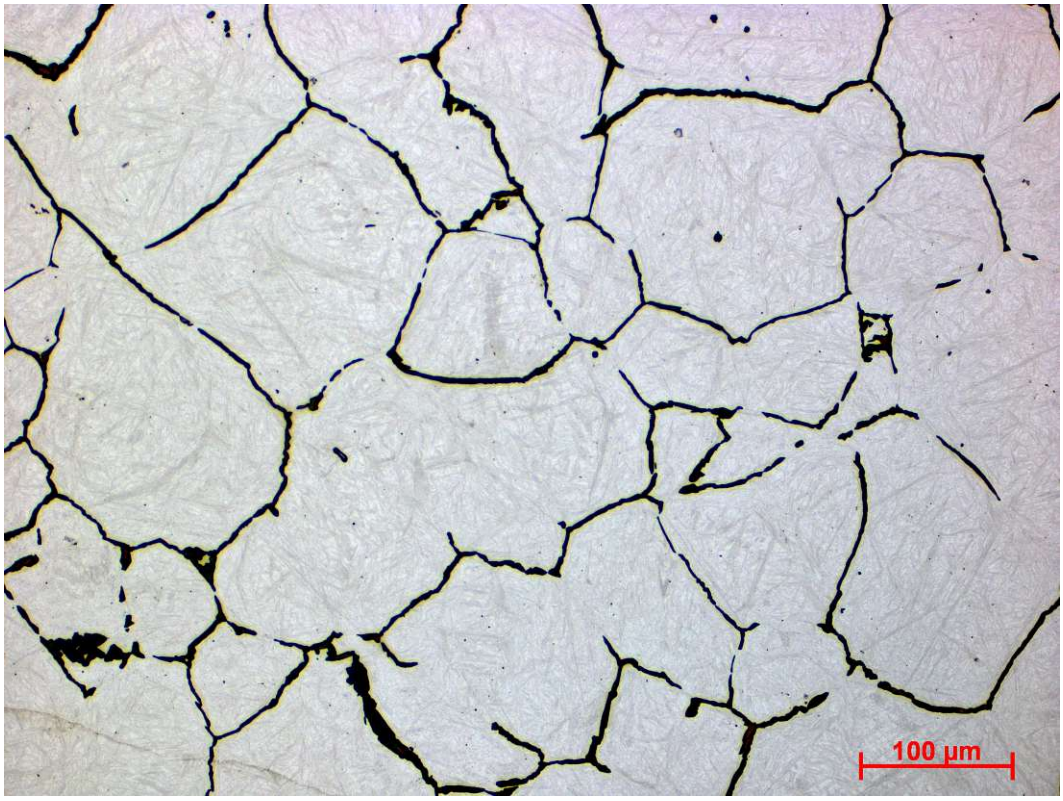

Figure 3.6: alloy FeCu1 reacted at 750°C for 10000s

One goal of this work is the evaluation of the formation of *SC* after different isotherm reaction durations and temperatures. Measuring the SC film thickness in 2D provides a good approach. For the desired outcome measuring in a 2D intersection planes will be accurate enough whereas measuring in 3D is too elaborate. Evaluating the *SC* film in 3D would be more accurate in terms of the actual form and dimension of the cementite but also much more complex (compare with [16]).

The calculation of the phase fraction of *SC* was made with the software ImageJ. With this tool, it is possible to evaluate the area of a given phase in an image. For

this purpose, images of the etched specimens with picric acid etchant appeared proper to get a good contrast between the cementite and the matrix and were preferentially used. After etching with picric acid etchant the cementite appears black and the matrix white, i.e. with good contrast between them. In the case of short t_{SC}, it was necessary to use images from SEM because of its higher magnification, which was necessary to visualise the much thinner cementite. In specimens where t_{SC} was shorter than 500s, it has been very difficult or nearly impossible to evaluate the phase fractions at all because of the low amount of cementite. Note that the contrast varied since etching can be quite tricky (compare with chapter 3.2.2) and therefore the quality of the images also varied up to a certain level. This handicap was also circumvented by using images from SEM. Three different images from different spots on the sample were taken and analysed to increase statistical significance. One big problem were inclusions because they also appeared black in the images, so they represented a possible source for an inaccuracy of the image evaluation. Those had to be removed manually in ImageJ before calculating the phase fraction.

The left half of Image 3.7 shows the intersection plane after etching with picric acid in the optical microscope. The right half shows the prepared image after removal of

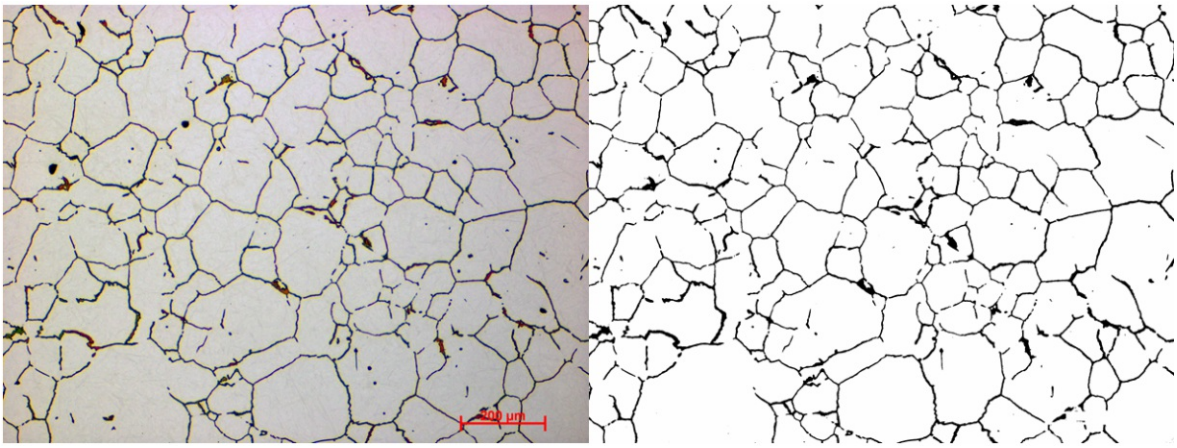

Figure 3.7: left half: image after etching with picric acid etchant in the optical microscope; right half: after binary conversion and preparation

inclusions and scale bar and conversion to binary format.

The prior γ-grain size was evaluated by making linear intercepts of the grain boundaries, as described by Macherauch and Zoch[51, p.75-81]. In this method, the two-dimensional image was cut with lines of a certain length. Then the grains cut by the line were counted. With the number of cut grains and the length of the line, the average grain size can be calculated. They [51] recommend working with at least 5 lines per image. The distance between the lines needs to be sufficiently wide so that two different lines do not cross the same grains. The grain where the line ended was not

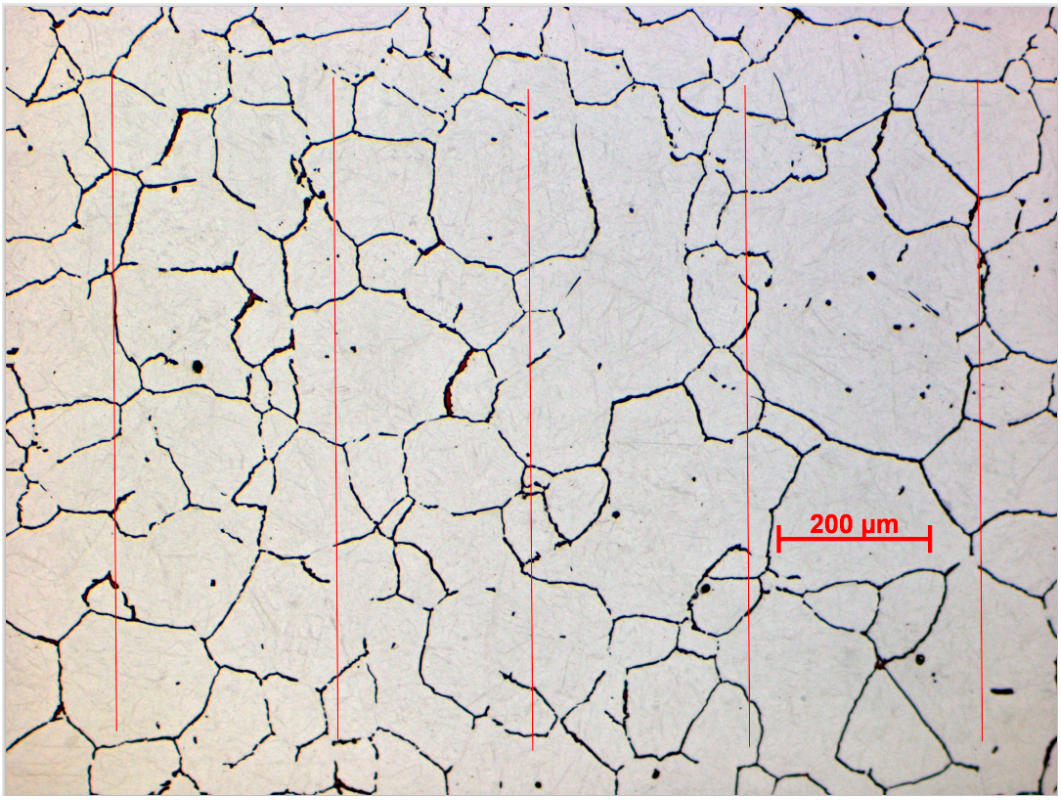

Figure 3.8: evaluation of the grain size

counted. To decrease the influence from possible local irregularities, images from three different positions of the same sample were taken and analysed.

The visualization of the γ-grain boundaries was realised indirectly via the grain boundary cementite of specimens having been preferably etched with the picric acid etchant. Because this method is executed only in a plane, the evaluated grain size will be smaller than the real one in 3D. Following the standard ASTM-E112-2010, the evaluated grain size is multiplied by the factor 1.57 to get the actual size in 3D[52]. Image 3.8 shows the principle approach of the preparation of the image.

3.3 Calphad-based MatCalc simulation

This work aimed to provide experimental data on the evolution of cementite in hypereutectoid steel. The data from the experiments, besides already existing data from the literature, was then compared to the results of thermokinetic simulations. In the following section, we will explain the general approach and especially the cementite precipitation simulation. We used the simulation software MatCalc with Calphad-based thermodynamic and diffusion databases and interfacial energies at two stages of this work. At first, it was used as a controlling tool during the determination of the heat treatment. The aim was to obtain simulative information at which temperature cemen-

tite would start to precipitate from the austenite phase and give a rough overview of the cementite evolution during the planned heat treatment. The proper temperature range for the heat treatment had to be found, where on one hand cementite would already precipitate but on the other hand, pearlite would not form. The magnitude of the incubation time between reaching the isothermal reaction temperature and the cementite precipitation start was also tested by simulation.

The second application was done during the comparison of the actual results from the experiments with the simulation of the cementite growth in MatCalc, i.e. the validation of the current precipitation model for cementite at the elaboration time of this work. The software packages MatCalc [53] and Thermo-Calc [54] were used with CDL-IPE thermodynamic databases. The used thermodynamic and diffusion database in MatCalc were version $mcfev2.060.tdb$ [55] and version $mcfev2.012.ddb$ [56], respectively. In Thermo-Calc we used the implemented thermodynamic database (FEDEMO).

Thermo-Calc was used for the visualisation of pseudo-binary phase diagrams, due to fast and easy handling for this task. These diagrams give a quick overview of the phase characteristics at equilibrium state. They show at which conditions, such as temperature, pressure or volume, thermodynamically distinct phases exist under equilibrium conditions. Pseudo-binary in this context means that the phase boundaries are calculated by variation of two of the elements, whereas the amounts of the others are kept constant. [57]

With this information, we were able to make basic predictions regarding the phase stability at given composition and temperature. It should be mentioned that evaluated steel compositions were simplified for the employment of Thermo-Calc, which was available only in the academic version, where only calculations with a maximum of three elements were possible.

We used MatCalc for thermokinetic simulations, especially for the precipitation simulation of cementite. During the simulations with MatCalc, cementite was treated as a heterogeneous precipitate at grain boundaries of the domain austenite. There is no model implementation in MatCalc with which we could simulate the evolution of a film surrounding grains. Therefore the grain boundary cementite half-thickness had to be evaluated via the cementite phase fraction and the austenite grain boundary area. The applied assumption behind the phase evolution of SC is that the shape plays no role in the simulation. In the simulation with MatCalc, it is assumed that the cementite forms as spherical precipitates.

$$D_{3d} = \frac{f_{SC}}{GA_{\gamma} * 2} \tag{3.3}$$

Equation 3.3 shows the evaluation of the grain boundary cementite film half-thickness(D_{3d}) via the phase fraction of cementite and the austenite grain area. The phase fraction of cementite (f_{SC}) was simulated in MatCalc. The evaluation of the γ-grain boundary area(GA_{γ}) was made via the initial grain diameter. The results from the experiments were adjusted with the parameter GOC from chapter 3.2.3 to increase the comparability between simulation and reality. In the simulative approach cementite homogeneously covers grain boundaries, and reevaluation of film thickness always results in an uniform film of constant thickness around grains. During the examination of the experiments, especially for short t_{SC}, it was however seen that grain boundary cementite does not show this continuity. High discontinuity was especially observed for alloy 4-1, where according adaption using GOC led to considerable improvements of the results.

The formation of new precipitates in MatCalc[58] follows the classical nucleation theory(CNT). In MatCalc, preferred nucleation sites such as "bulk", "dislocation", or grain boundaries can be chosen. Spanos and Kral [12] reported that grain boundary cementite predominantly nucleates at grain boundary corners. In contrast, the chosen nucleation sites for the present simulation of secondary cementite were the grain boundaries and not grain boundary corners. This deviating setup from observation was required to allow for the appropriate diffusion geometry during precipitation. The appropriate grain boundary diffusion geometry is as described by E. Kozeschnik et al. [59]. In MatCalc this setting is only possible if grain boundary is selected as a nucleation site and not grain boundary corners [60]. Indeed, grain boundary as nucleation site will lead to a higher number of nuclei than grain boundary corner, but the proper diffusion geometry outperforms the role of grain boundary site in terms of precipitation control in this case. The growth of the grain boundary cementite is widely influenced by the availability of carbon. Increasing grain size significantly retards precipitation at the grain boundary due to large diffusion distances inside the grain. Therefore, defining a proper diffusion geometry has a big influence on the simulation result, especially for larger grains.

The simulations were carried out under full equilibrium assumption(ortho-composition) and activating the option "use heterogeneous site energy in nucleation". We assumed full equilibrium composition because simulations under para-equilibrium conditions were not satisfactory, further information is given in chapter 4.2.3. "Use heterogeneous site energy in nucleation" has an influence on the grain boundary surface energy and therefore also on the driving force. It takes the areas of the grain boundary into account, where already some precipitates have grown and calculates the surface energy of thus reduced grain boundary and equally lowers the nucleation barrier for new nuclei. The simulation parameter "mdef" (matrix diffusion enhancement factor) adjusts the diffusion coefficient stored in the mobility database. This is necessary if the simula-

tion setting does not represent the conditions the diffusion database has been assessed for[61].

For the isothermal microstructure simulation, only the austenite and cementite phase were selected. For the simulations, the values for the grain size from the experiments were taken, see Table 4.3. The microstructure simulation in MatCalc was carried out under the following settings, see Table 3.5. All other parameters were kept as per

Table 3.5: simulation parameters

name	value	note
equilibrium dislocation density	1e12 m^{-2}	[62]
grain and subgrain diameter alloy FeCu1	180µm	Table 4.3
grain and subgrain diameter alloy 4-1	50µm	Table 4.3
grain and subgrain diameter alloy FeCu3	160µm	Table 4.3
grain and subgrain diameter alloy 5-2	50µm	Table 4.3
mdef	3	fitting parameter
austenite grain-elongation-factor	1	equiaxed grains

default. We carried out the microstructure simulations for 300000 seconds isothermally. The used MatCalc-script can be seen in the appendix.

For interpretations of the precipitation simulation results, the key quantities precipitate phase fraction, number density and radii were plotted. Another task during the examination with MatCalc was to evaluate and test alternative settings and parameters that would lead to a simulation result closest possible to reality.

All relevant parameters of the simulation, meaning those which showed an effect on the kinetic results when changed, were adapted, and the influence on the kinetic results was assessed, see chapter 4.2.3.

One of the main issues of the simulation was the unrealistically large retardation of cementite evolution due to alloying elements such as Si, Cu or Mn, among others. Another major effect on the simulation results is caused by changing the nuclei composition control. Here especially the influence of the para-equilibrium in combination with different substitutional elements in contrast to the ortho-equilibrium setting was tested, see chapter 4.2.3. Simulations in MatCalc were always carried out with at least three alloying elements, because of numerical inconsistencies with the choice of Iron and Carbon alone. This means that for “quasi” comparisons to pure Fe-C, still almost pure Fe-C, i.e. including traces of third element approximating zero concentration was required.

4 Results

In this chapter, the results obtained with the methods from chapter 3 will be presented. The discovered outcome will be split up into the results from the experiments and the findings from the adaptions in MatCalc. The differences between the investigated alloys will be presented.

4.1 Experimental results

The results from the experiments are split up into three subsections. In the end, an overall summary will be given. The applied methods are described in chapter 3.2.3. In this part, the ascertained values and graphs will be presented. For the reason of explanation and qualitative confirmation, images of the microstructure will also be presented.

4.1.1 Raw material

We first want to present the results of the investigations with the basic raw material. We did this to be able to compare the material before and after the heat treatment. Table 4.1 shows the notation of the alloys, the type of production, the number of specimen taken and the average austenite grain size of the raw material. Figure 4.1

Table 4.1: listing of the analysed alloys

identifier	type	number of specimen	reference sample	γ-grain size
FeCu1	cast material	40	bA3β	681µm
4-1	railhead	24	left upper half	166µm
FeCu3	cast material	24	former study	75µm
5-2	railhead	24	former study	25µm

shows a typical microstructure of the raw material of alloy FeCu1 after etching with the picric acid etchant. The microstructure was mainly perlitic with grain boundary cementite at the former autenite grain boundaries and Widmannstätten cementite in the grains. The interlamellar spacing of the pearlite can be seen at relatively low

Figure 4.1: untreated raw material from alloy FeCu1, etched with picric acid etchant, magnification 500x, cementite appears black, pearlite white

magnification, which is evidence for a relatively big interlamellar spacing and a low cooling rate during the production process of the material [4, p.215]. Figure 4.2 shows the microstructure of alloy 4-1. The former austenite grain size is smaller than for alloy FeCu1 (Figure4.1). Figure 4.3 shows the untreated raw material of alloy FeCu3, etched with Nital. It shows a typical pearlitic structure. The grain size of the untreated raw material of the different alloys varies. Besides a slightly different production method, another reason for the smaller grain size is caused by different additional alloying elements in alloys 4-1 and 5-2. Elements such as V or Nb form stable carbides that lock the austenite grain boundaries during the γ-α transformation. This leads to finer ferrite grains [14, p.95]. The cementite appears as grain boundary cementite at the former austenite grain boundaries or in pearlite. The observed microstructure is typical for hypereutectoid steel.

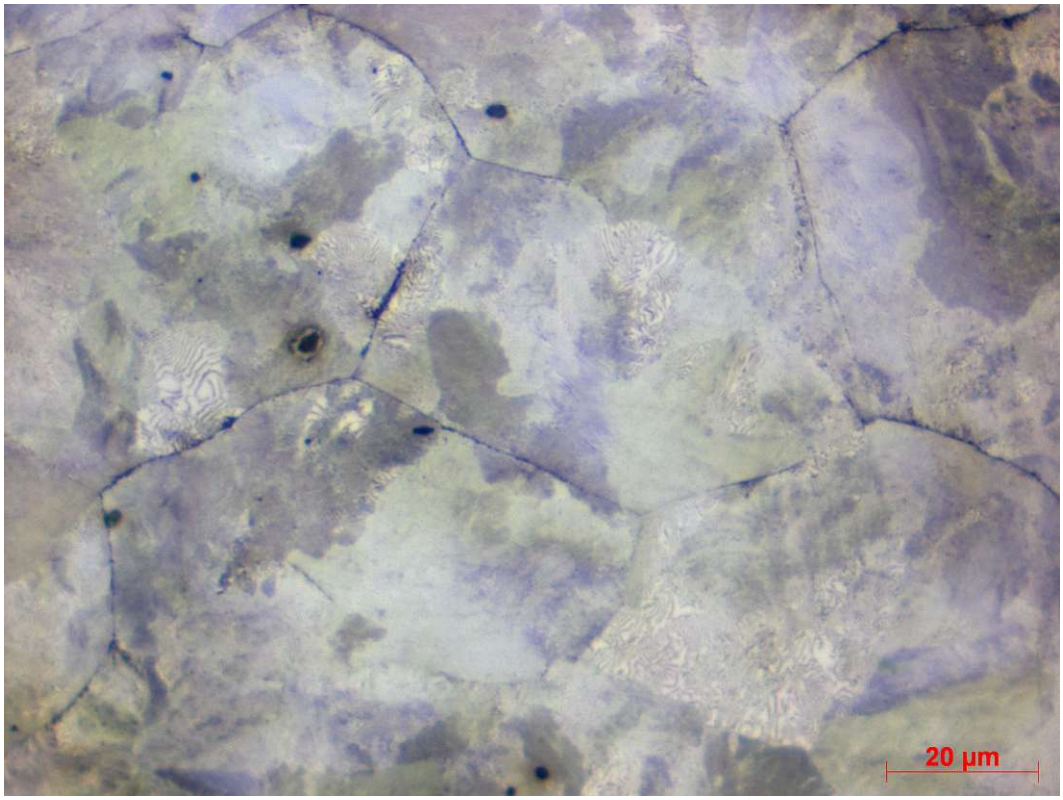

Figure 4.2: untreated raw material from alloy 4-1, etched with picric acid etchant, magnification 1000x, cementite appears black

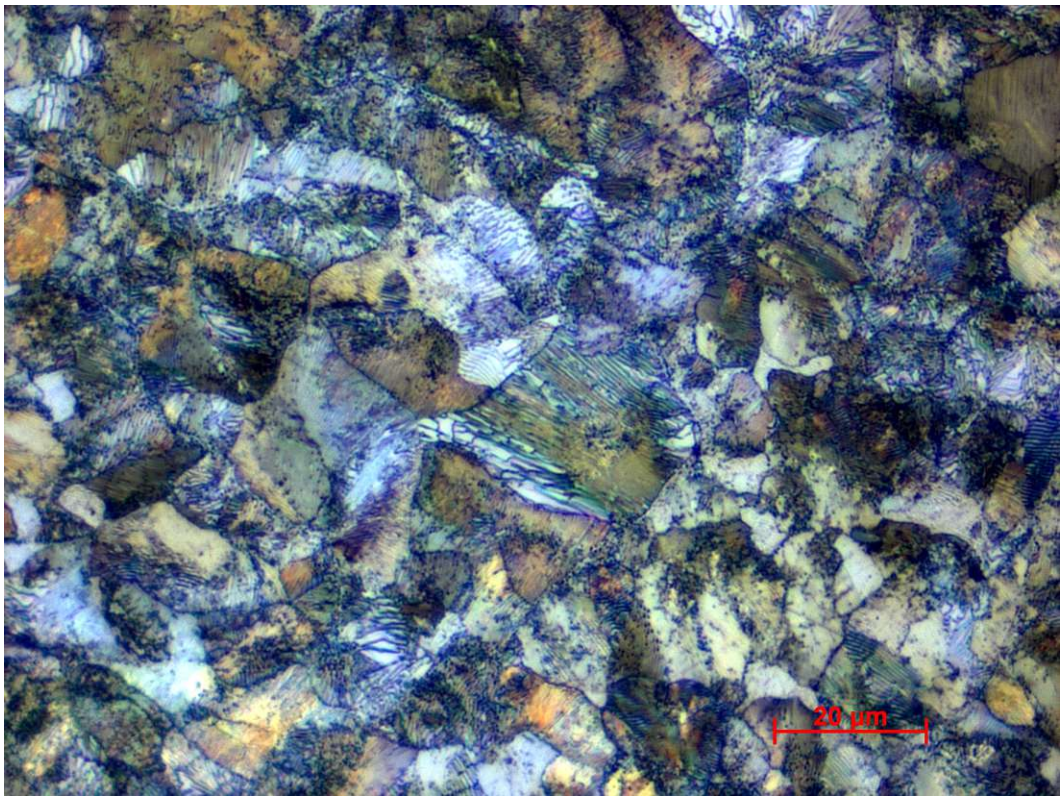

Figure 4.3: untreated raw material from alloy 5-2, etched with nital, magnification 1000x, cementite appears black

4.1.2 Secondary cementite thickness

Probably one of the most interesting aspects of this work was to evaluate the thickness of the forming *SC* at the γ-grain boundaries. We used particularly this parameter to evaluate thermokinetic simulations. Table 4.2 shows the evaluated values of the half film thickness D of the *SC* and the grade of completeness of the cementite network GOC at isothermal reaction temperatures T_{SC} 780°C and 750°C. Column D_{2D} contains the measured cementite half-thickness from the images made with the microscope in 2D and D_{3D} shows the converted grain boundary thickness in 3D, as explained in chapter 3.2.3.

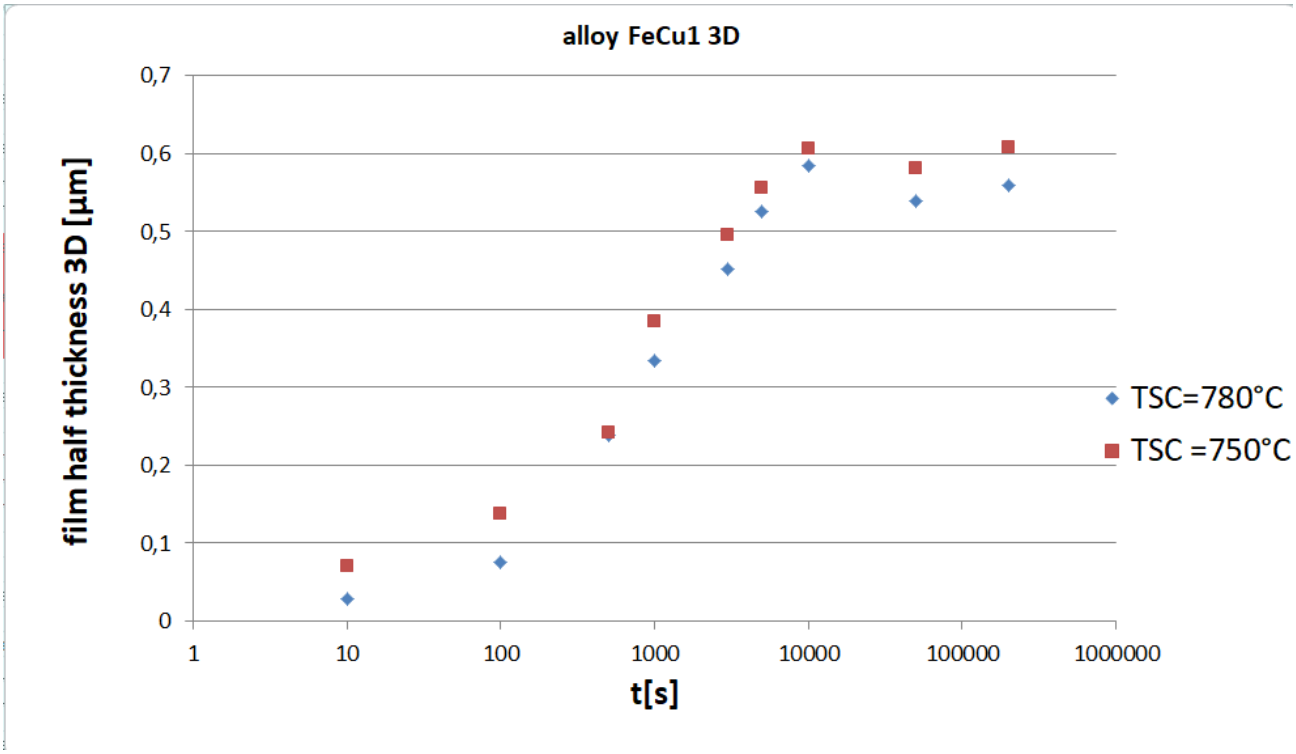

Figure 4.4: evolution of the *SC* half thickness in 3D of alloy FeCu1 at 780°C and 750°C

Figures 4.4, 4.5, 4.6 and 4.7 show the according plots of the *SC* half-thickness, of alloys FeCu1, 4-1, FeCu3 and 5-2, respectively, having been already converted to 3D. It can be seen that the thickness of the cementite grows until it reaches a certain level where growth stagnates. As expected the curves follow an exponential growth before saturation. Due to the higher driving force at lower temperatures, the amount of cementite was expected to be larger at T_{SC} 750°C than at 780°C. At first sight for alloy 4-1, Figure 4.5, and partially for FeCu3, Figure 4.6, the opposite seemed to be true. This unexpected behaviour needs some deeper inspection, as follows. Besides measuring the thickness of the grain boundary cementite the grade of completeness, GOC, of the grain boundary cementite grid in the 2D intersection plane was also evaluated. With the values of G, as listed in Table 4.2, the adapted average thickness values were

Table 4.2: grain boundary film half thickness D[µm], grade GOC,and converted thickness in 3D of *SC* at isothermal temperatures T_{SC} 780°C and 750°C

alloy	t_{SC}[s]	T_{SC}[°C]	D_{2D}	GOC[%]	D_{3D}	T_{SC}[°C]	D_{2D}	GOC[%]	D_{3D}
FeCu1	10	780	0.13	10	0.029	750	0.35	10	0.07
FeCu1	100	780	0.32	10	0.076	750	0.49	30	0.041
FeCu1	500	780	0.86	20	0.23	750	0.77	80	0.19
FeCu1	1000	780	1.03	70	0.33	750	1.15	90	0.34
FeCu1	3000	780	1.32	90	0.45	750	1.43	90	0.45
FeCu1	5000	780	1.53	80	0.52	750	1.59	90	0.50
FeCu1	10000	780	1.68	80	0.58	750	1.70	95	0.57
FeCu1	50000	780	1.51	100	0.54	750	1.63	100	0.58
FeCu1	200000	780	1.58	100	0.56	750	1.70	100	0.61
4-1	50	780	0.17	5	0.05	750	0.11	5	0.02
4-1	100	780	0.19	10	0.05	750	0.13	10	0.023
4-1	500	780	0.24	10	0.05	750	0.22	70	0.067
4-1	1000	780	0.31	20	0.08	750	0.33	90	0.11
4-1	3000	780	0.41	40	0.13	750	0.37	100	0.13
4-1	5000	780	0.46	60	0.15	750	0.38	100	0.14
4-1	10000	780	0.54	70	0.19	750	0.42	100	0.15
4-1	50000	780	0.49	90	0.17	750	0.42	100	0.15
4-1	200000	780	0.59	90	0.21	750	0.46	100	0.16
FeCu3	50	780	0.40	5	0.067	750	0.41	10	0.014
FeCu3	100	780	0.61	10	0.021	750	0.66	30	0.07
FeCu3	500	780	1.34	25	0.13	750	1.23	90	0.42
FeCu3	1000	780	1.48	40	0.23	750	1.43	100	0.56
FeCu3	3000	780	1.75	60	0.42	750	1.45	100	0.57
FeCu3	5000	780	1.76	75	0.53	750	1.51	100	0.60
FeCu3	10000	780	1.73	90	0.53	750	1.59	100	0.63
FeCu3	50000	780	1.73	90	0.63	750	1.61	100	0.64
FeCu3	200000	780	1.20	70	0.32	750	1.57	100	0.63
5-2	50	780	0.12	5	0.002	750	0.13	5	0.002
5-2	100	780	0.12	5	0.002	750	0.19	10	0.007
5-2	500	780	0.19	20	0.013	750	0.27	80	0.08
5-2	1000	780	0.32	40	0.047	750	0.55	90	0.20
5-2	3000	780	0.36	60	0.083	750	0.61	100	0.25
5-2	5000	780	0.36	70	0.095	750	0.64	100	0.26
5-2	10000	780	0.44	80	0.14	750	0.59	100	0.24
5-2	50000	780	0.46	100	0.18	750	0.56	100	0.23
5-2	200000	780	0.50	100	0.20	750	0.61	100	0.25

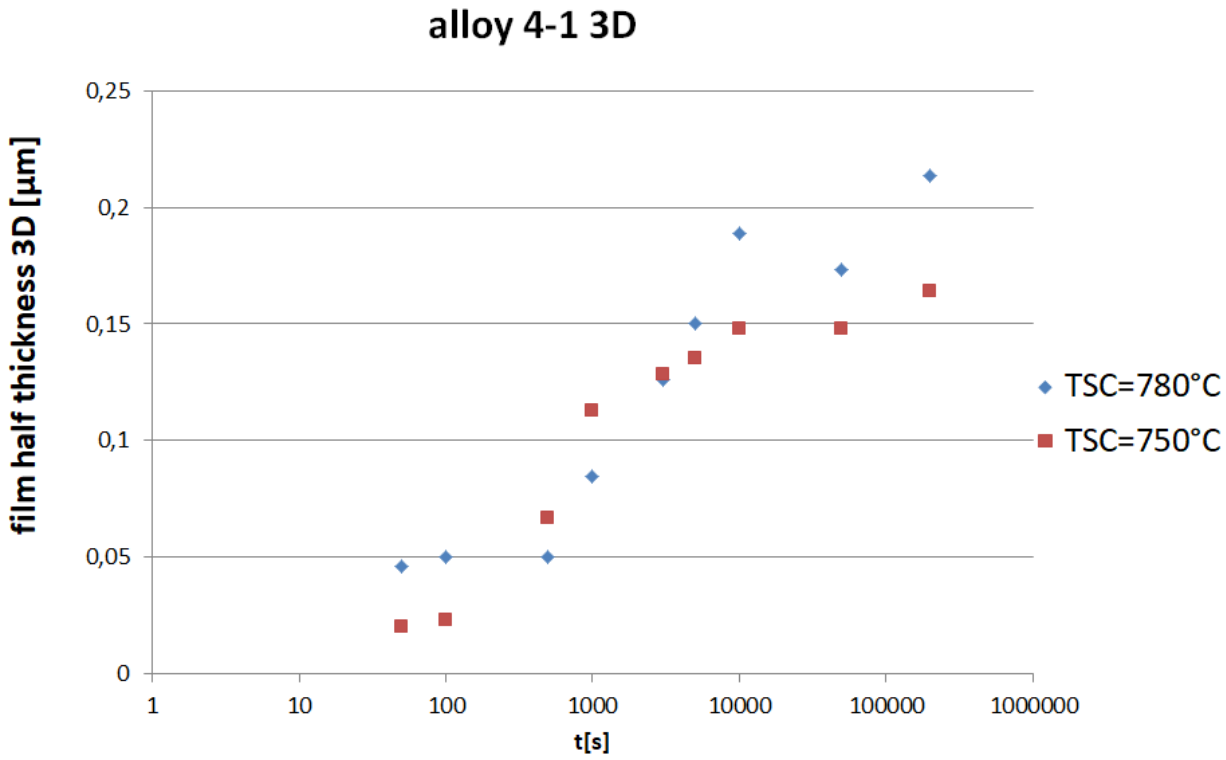

Figure 4.5: evolution of the *SC* half thickness of alloy 4-1 at 780°C and 750°C

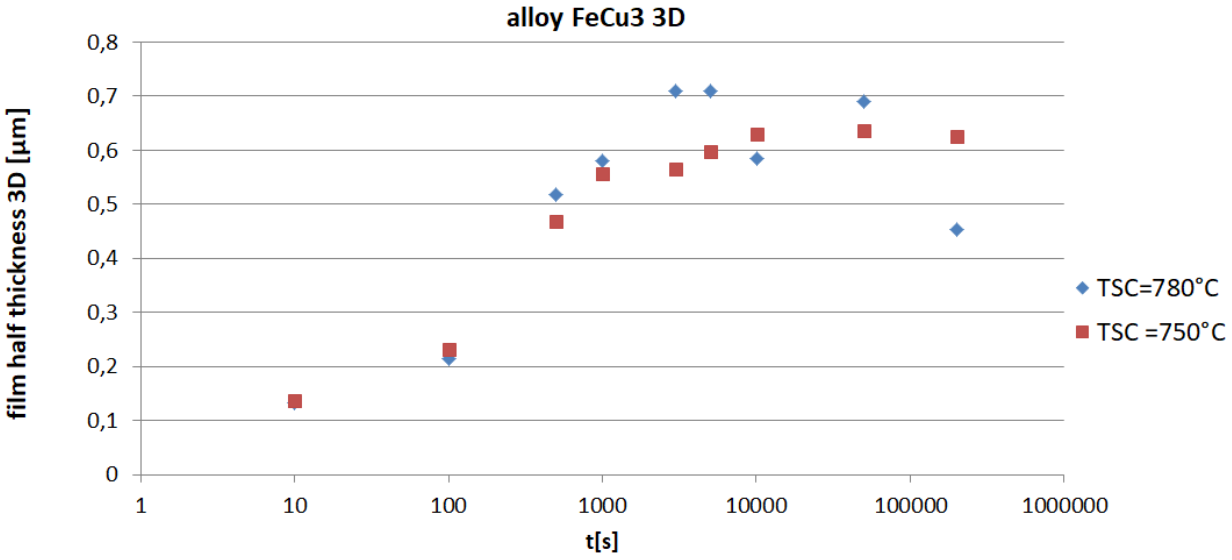

Figure 4.6: evolution of the *SC* half thickness of alloy FeCu3 at 780°C and 750°C

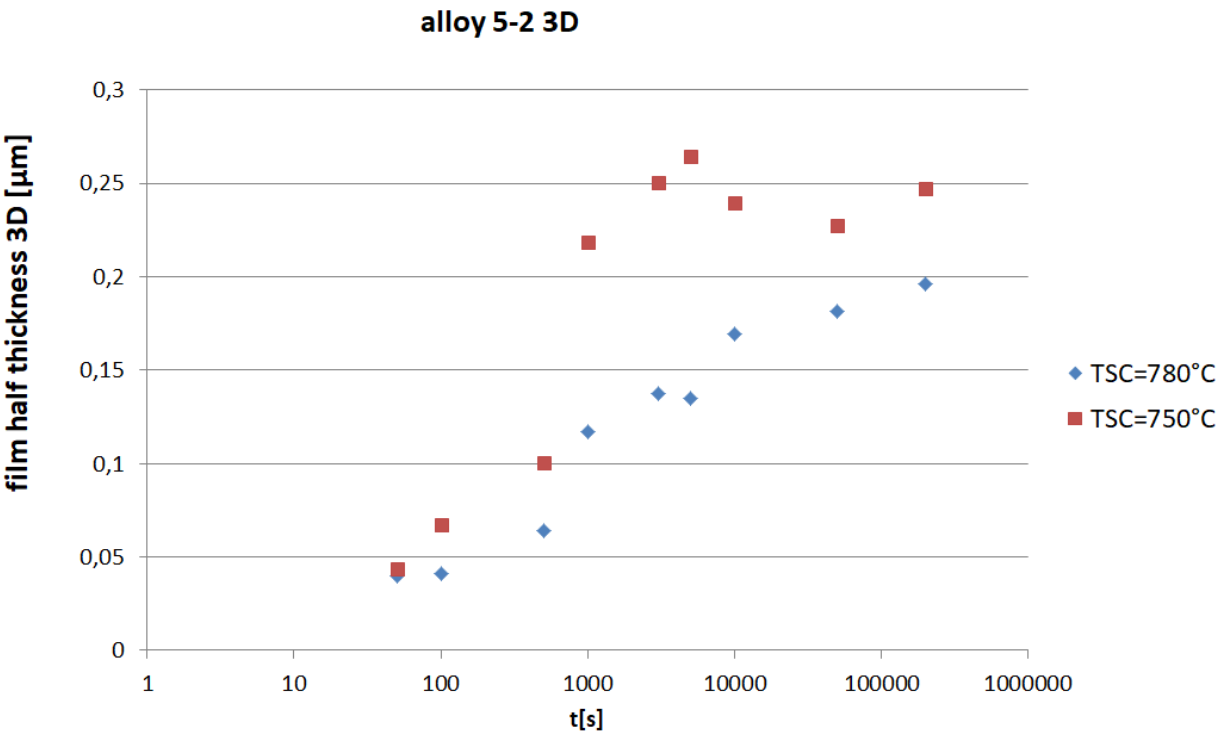

Figure 4.7: evolution of the *SC* half thickness of alloy 5-2 at 780°C and 750°C

calculated, which can be interpreted as if all austenite grains would be completely covered with a cementite film of constant thickness corresponding to the correct cementite fraction. When examining the resulting micrographs the influence of the T_{SC} on the evolution of the cementite then becomes immediately visible. The cementite network at 750°C was much more complete and pronounced. For alloy 5-2 and 4-1, the cementite network at T_{SC} 780°C by far is not complete, whereas at 750°C isothermal reaction time it appears to be even at lower duration times. Figures 4.8, 4.10, 4.11 and 4.9 show the evolution of the cementite film thickness, adapted by the parameter G. The curves again follow an exponential growth in terms of temperature control, based on driving force considerations, see section 4.2.2. The cementite thickness at T_{SC} 750°C then is also for alloys 4-1, Figure 4.9, and FeCu3, Figure 4.10, higher than at 780°C. The only exception remains for the longest isothermal treatments for alloy 4-1, where the temperature control on the cementite evolution reverses again (Figure 4.9). The reason for this is not clear, accepting that the temperature control of these experiments seemed to be correct. Potential measurement errors in the dilatometer due to connection problems regarding the thermocouple still have to be taken into account. The manual evaluation of GOC may also be an additional source of inaccuracies. Other explanations for the reversion at long isothermal reaction times in Figure 4.9 could be a coincidence regarding the taken spots for measurement of SC thickness and thus resulting deviations or an influence of the more complex alloying of 4-1. The evaluated

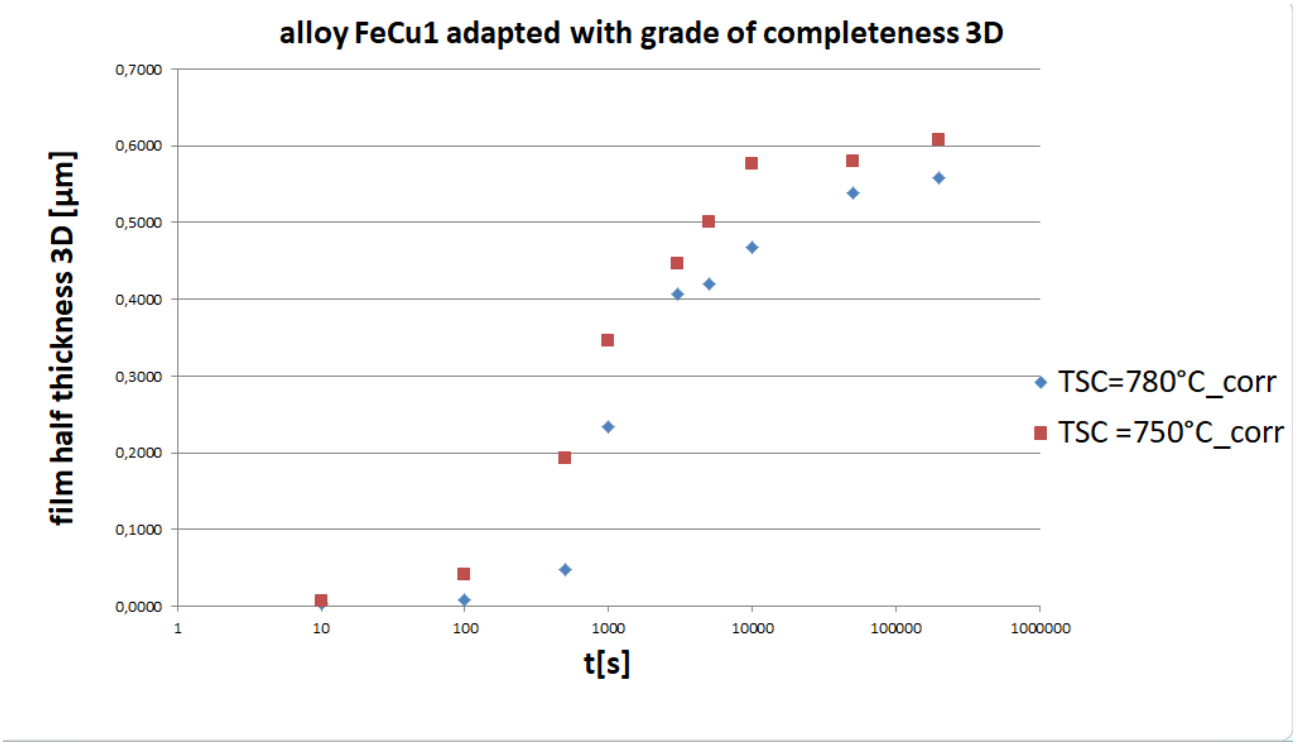

Figure 4.8: evolution of the *SC* half thickness of alloy FeCu1 at 780°C and 750°C, thickness values adapted with grade of completeness GOC

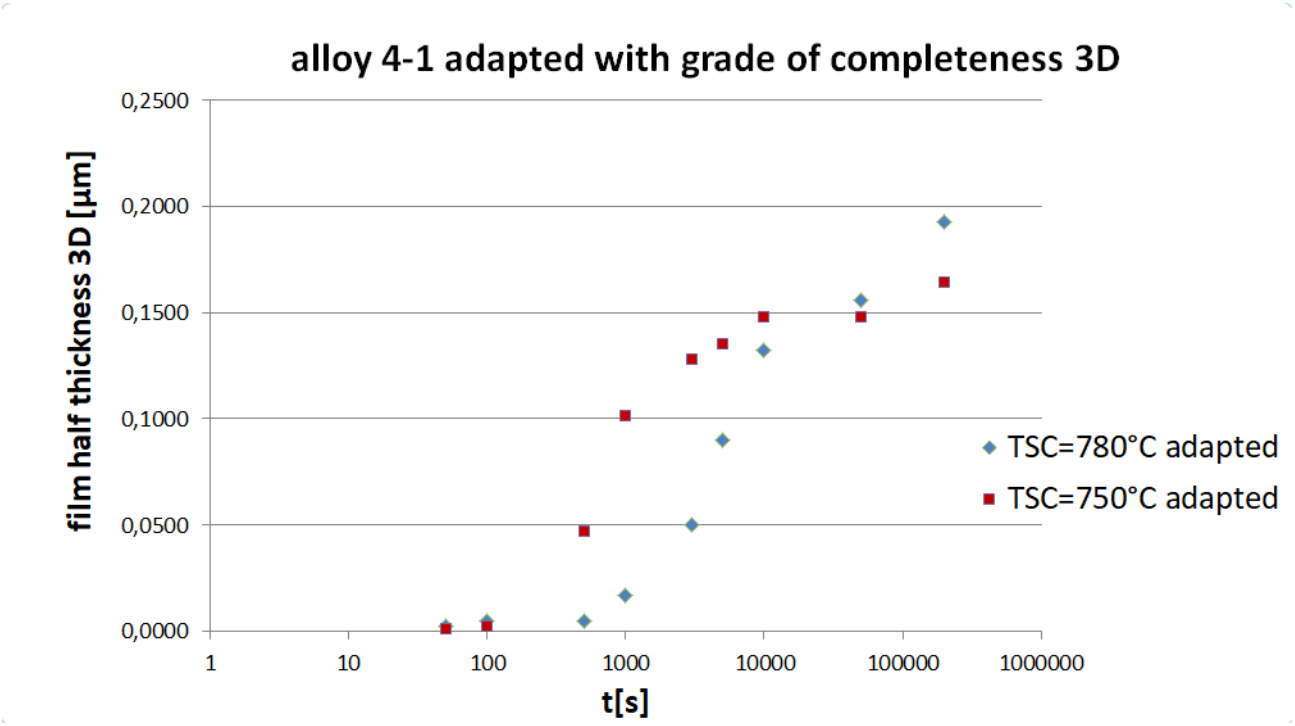

Figure 4.9: evolution of the *SC* half thickness in 3D of alloy 4-1 at 780°C and 750°C, thickness values adapted with grade of completeness GOC

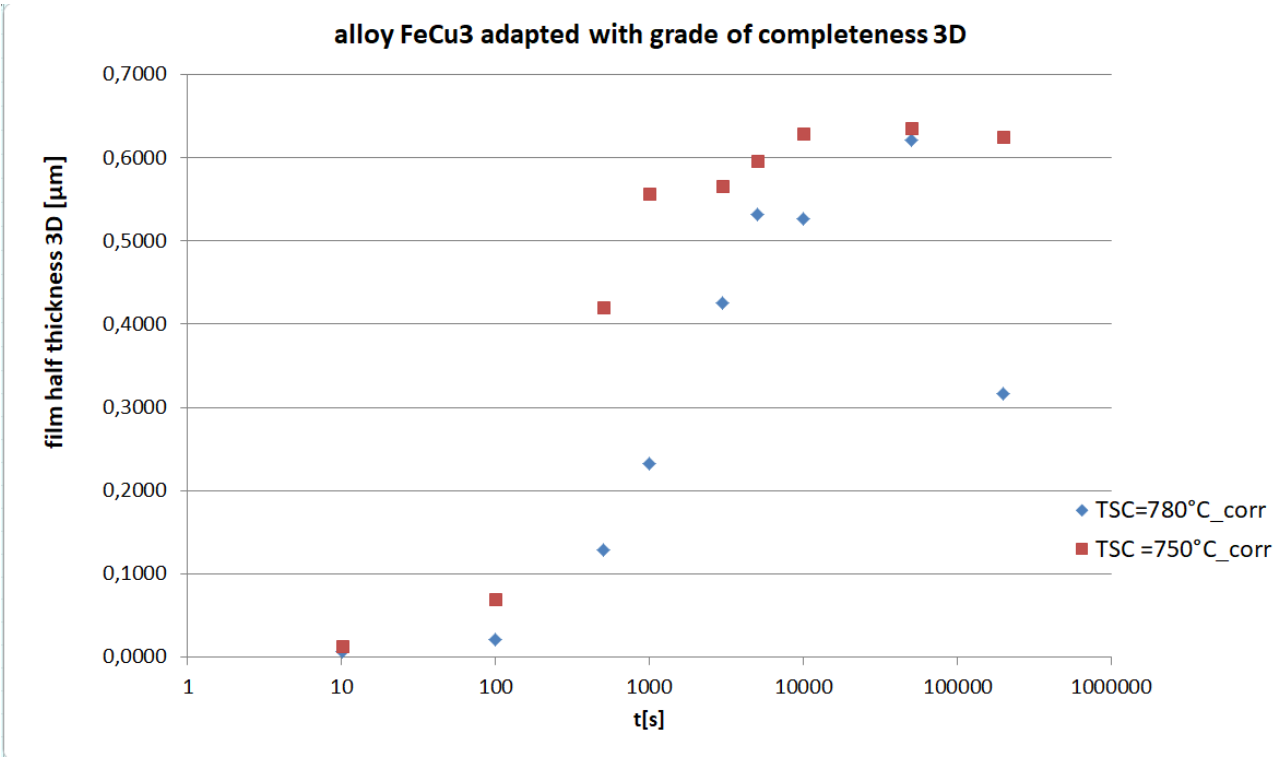

Figure 4.10: evolution of the *SC* half thickness in 3D of alloy FeCu3 at 780°C and 750°C, thickness values adapted with grade of completeness GOC

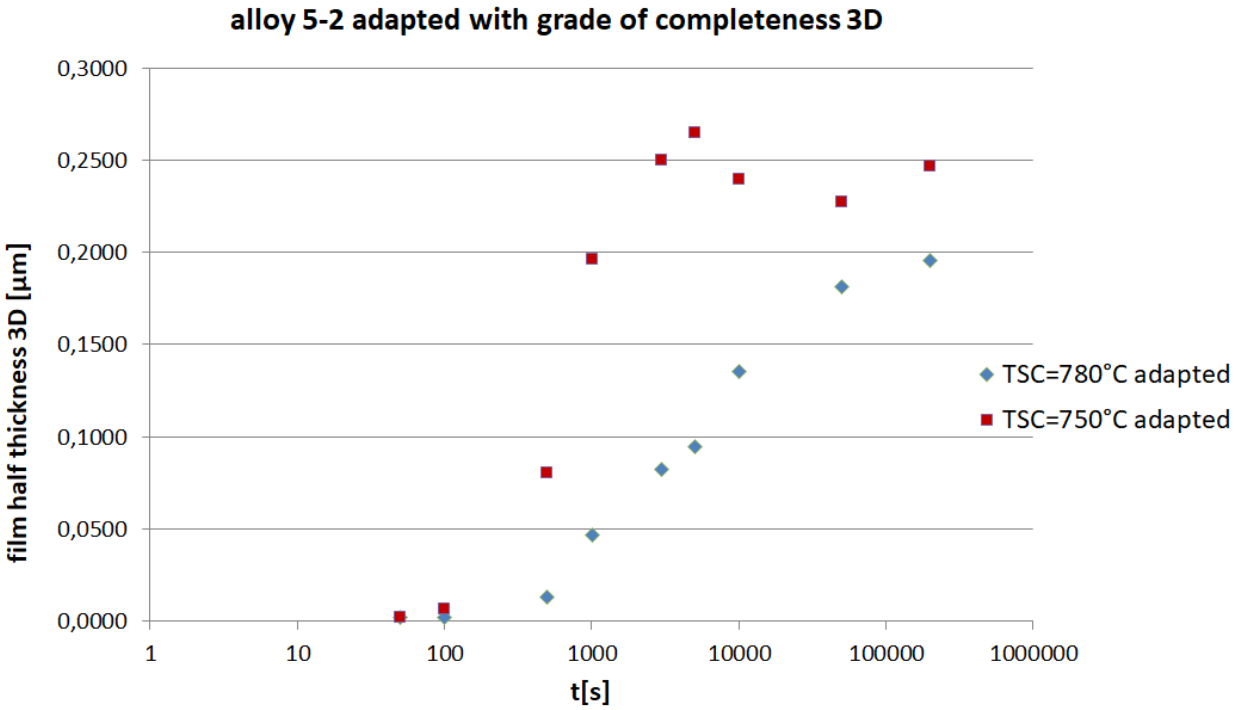

Figure 4.11: evolution of the *SC* half thickness in 3D of alloy 5-2 at 780°C and 750°C, thickness values adapted with grade of completeness GOC

phase fraction, see chapter 4.1.3 and subsection 4.1.3, also shows the higher amount of cementite for T_{SC} 750°C and confirms the thickness evaluation. This further points out that considering the distribution of the cementite in the sectional plane by GOC appears to be necessary to achieve meaningful results. Figure 4.10 shows a drop for the test with 200000s and 780°C. We made three heat treatment experiments which all led to results that would not fit with the rest of the test series. The reason for this behaviour is not clear. Problems with the temperature control are unlikely to be the main responsibility.

All the plotted diagrams show the arithmetic mean value of the cementite half thickness. In the appendix on page 81 boxplots of the measured values, without adaptions by GOC, are shown. This information was added to give more detailed information about the distribution of the measured values. This reveals that most of the data lie close, but the maximum thickness show a larger scater.

In the following, critical questions in the interpretation of observed cementite thicknesses are treated. In terms of continuity, alloy 5-2 behaved like 4-1 and FeCu3 as FeCu1, respectively. This is as expected because they contain similar alloying elements, see Table 3.1. Especially during examination in SEM, we noticed that the cementite in alloys 4-1 and 5-2 is much more discontinuous. Figure 4.12 a) shows an image of alloy FeCu1 with an area where the cementite is way bigger than in the surrounding area. It quite often occurred that the thickness was bigger when the size of

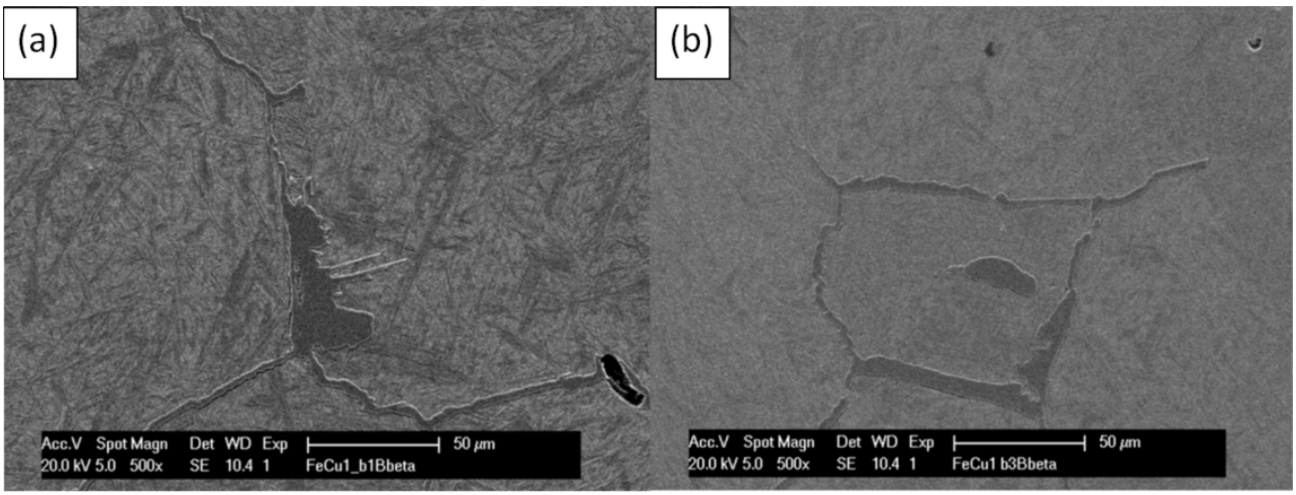

Figure 4.12: a)SEM image of alloy FeCu1 at magnification 500x, sample tested at 750°C for 3000s, locally increased thickness of cementite film / b)SEM image of alloy FeCu1 at magnification 500x, sample tested at 750°C for 10000s, virtually smaller grain in 2D sectional plane

the grain seemed to be small, such as in figure 4.12 b). This illustrates the need of converting the measured data from 2D to 3D. One should not forget that this is only a sectional plane of a three-dimensional object. So what looks like a smaller grain in

figure 4.12b), is probably just a corner of a bigger grain. This also explains up to a certain level the increase of cementite thickness around those areas. When coincidently putting the intersecting plane close to the corner, the cementite film around that grain appears to be bigger. Our investigations of the microstructure have in general shown that the microstructure is homogeneous and that the size of the grain size does not vary significantly, which confirms that virtually smaller "grains" represent corners of larger grains.

When taking into account the results from chapters 4.1.4 and 4.1.3 the influence of the grain size on the film thickness becomes obvious. This shows the direct influence of the available grain boundary area on the reached grain boundary cementite thickness. With decreasing grain size the available amount of carbon per grain decreases, which results in a lower cementite thickness. Due to the similar carbon content of different material studied, the respective phase fraction of cementite did not vary much.

Another interesting outcome was to see the influence of alloying elements Si, Mn and Cr in 4-1 and 5-2 on the continuity of the cementite film at the grain boundary. Figure 4.13 shows a comparison between alloy FeCu1 and alloy 4-1 examined for 10000s at 780°C. Besides the achieved grain size the frequent interruptions in the cementite film in

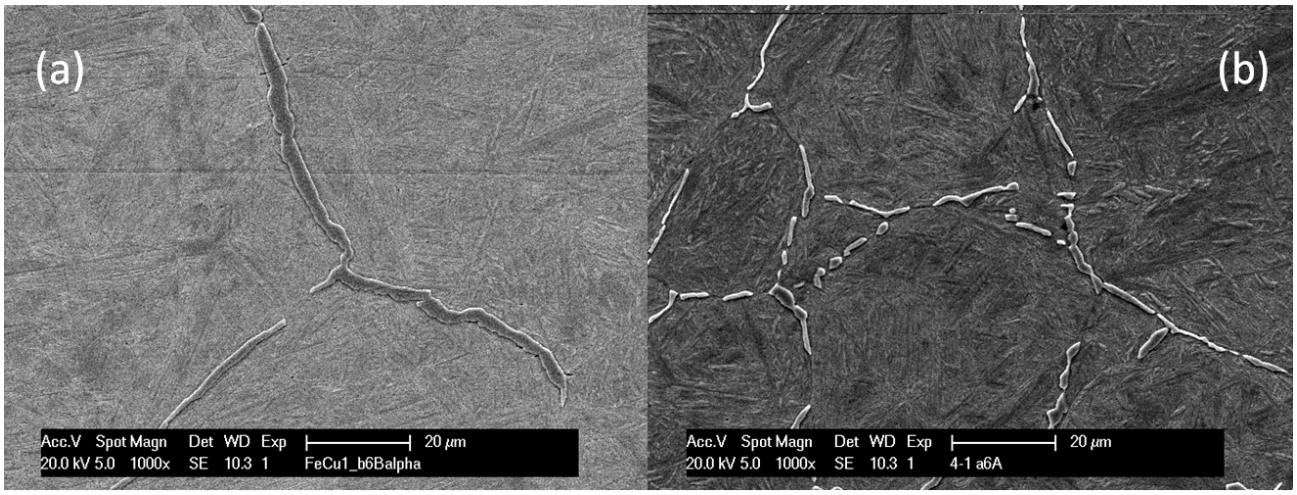

Figure 4.13: difference of continuity between alloy FeCu1 (a) and alloy 4-1 (b), both tested at T_{SC} 780°C and t_{SC} 10000s

alloy 4-1 (b) become obvious. In theory grain boundary cementite grows in a dendritic manner primarily along austenite grain boundaries. After a short duration, a complete cementite film around the austenite grains is formed [16], as seen in the left half of figure 4.13. Figure 4.14 shows similar results in terms of discontinuity for alloy 5-2 as for alloy 4-1. It is reported that Si leads to discontinuities whereas Cr and Mn are retarding the coarsening of cementite [26]. In terms of continuity, this statement fits quite well with the observations of the experiments. The grain boundary cementite in alloys 4-1 and 5-2 with 0.995 w% Si and 0.924 w% Si, respectively, was very discontinuous, compared

with alloys FeCu1 and FeCu3, which did not contain Silicon and showed a continuous grain boundary network. See figures 4.13 and 4.14. The alloys 4-1 and 5-2 contained 0.36 w% Cr and 0.209 w% Cr respectively whereas the alloys FeCu1 and FeCu3 did not contain any Cr, therefore an influence of Cr on the continuity can not be excluded. A combined influence of Si, Cr and Mn on the discontinuity of the SC can not be

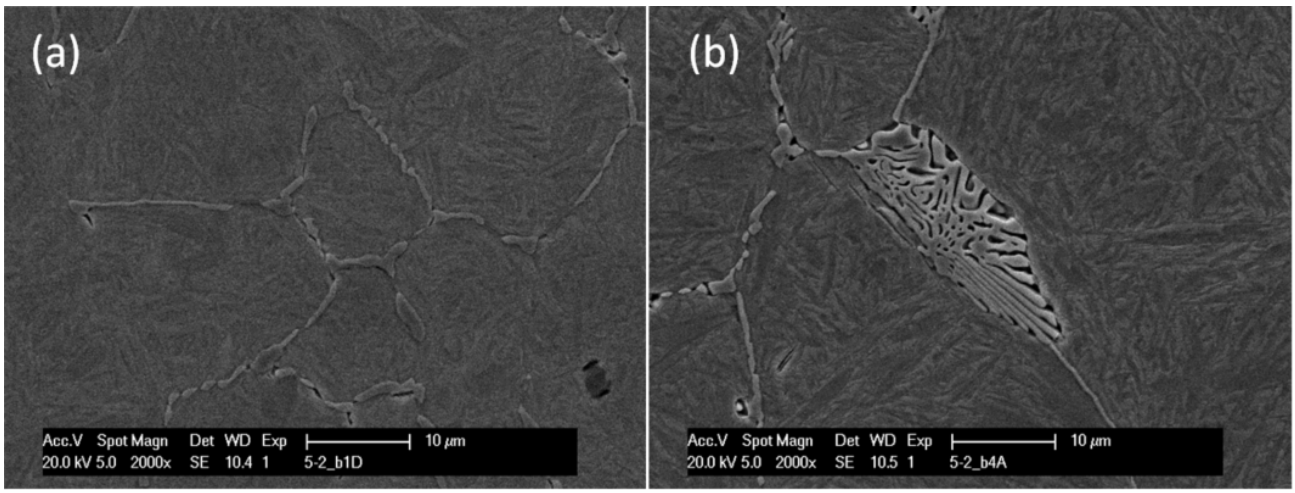

Figure 4.14: cementite form in alloy 5-2 isothermally reacted for 5000s at 780°C (a) and 750°C (b), half (b) shows the quasi-lamellar shape of cementite

characterised clearly in this study. The alloys FeCu1 and FeCu3 contained a similar amount of Mn as alloy 4-1 and 5-2, but no Cr or Si. Following this, we can conclude that Mn does not influence the continuity of SC, whereas for Cr a similar conclusion can not be made.

An explanation for the retardation through Cr is due to the peculiar partitioning of chromium between austenite and cementite under an equilibrium state, as stated by Ando and Krauss[11]. They declare that low late-stage thickening rates can be explained by retardation of ledge movement through Cr partitioning. Another possibility for sluggish thickening can be other alloying elements.

Regarding the retarding of coarsening of cementite growth by Cr and Mn, we can not make a clear statement, which results from the similar content of Cr and Mn of the four alloys. What can be said is that thickening stops before equilibrium is reached, independent of the alloy and especially for T_{SC} 780°C, see also chapter 4.1.3. The sluggish thickening of cementite allotriomorphs was already described [9] [11] [12].

Another interesting finding during the examination of the samples was the shape of the cementite in alloy 5-2 for isothermal reaction temperature 750°C, as seen in Figure 4.14 (b). The sample was isothermally reacted at 750°C for 5000s. We observed this quasi-lamellar shape of cementite systematic throughout the sample surface and also at all other samples reacted at 750°C and varying durations. This effect did not occur at 780°C. We did not find similar results in the literature. One explanation is that

the cementite grows together with vanadium-carbides of the form M-C. Vanadium is a strong carbide-forming element [p.120 14]. Bhadeshia [14] states that the limit where Vanadium cannot be dissolved in austenite and forms excess alloy carbides lies at about 1-2w%. The Vanadium content in alloy 5-2 is 0.143w%. We made some simulations about the precipitation of vanadium-carbides in alloy 5-2 which are presented in chapter 4.2.5.

4.1.3 Cementite phase fraction

In this chapter, the evaluated cementite phase fraction will be presented. The methods are explained in subsection 3.2.3. Figures 4.15, 4.16, 4.17 and 4.18 show the evolution of the *SC* phase fraction of the alloys at 780°C and 750°C.

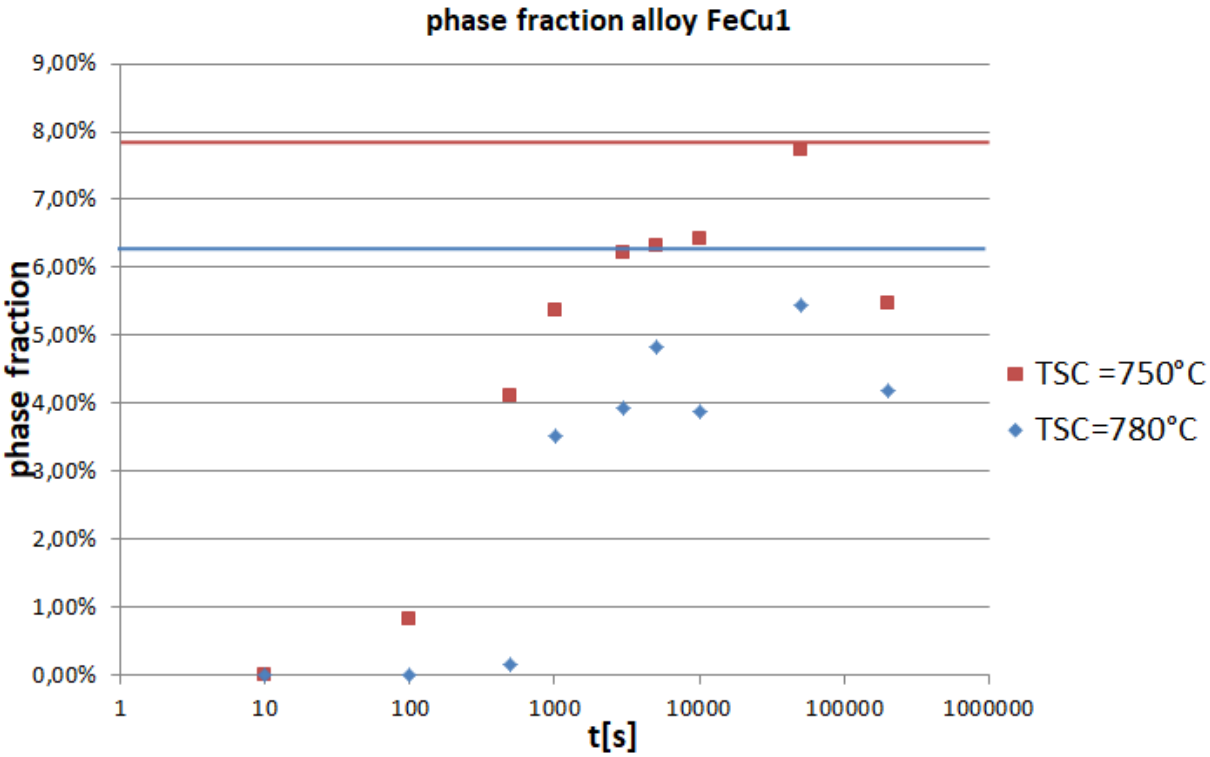

Figure 4.15: evolution of the *SC* phase fraction of alloy FeCu1 at 780°C and 750°C, with equilibrium phase fraction, blue and red line present equilibrium fraction for 780°C and 750°C, respectively

The blue and red horizontal lines show the equilibrium phase fraction at 780°C and 750°C, respectively. The equilibrium data were evaluated via stepped equilibrium calculations with MatCalc. Table 4.4 in chapter 4.2 shows the exact values. Explanations of the calculation are made in chapter 3.3. For the alloys, an exponential growth followed by saturation can be seen. For alloy FeCu1 a peak at 50000s for both temperatures can be seen. The reason for this is not clear, but it is probably just a coincidence

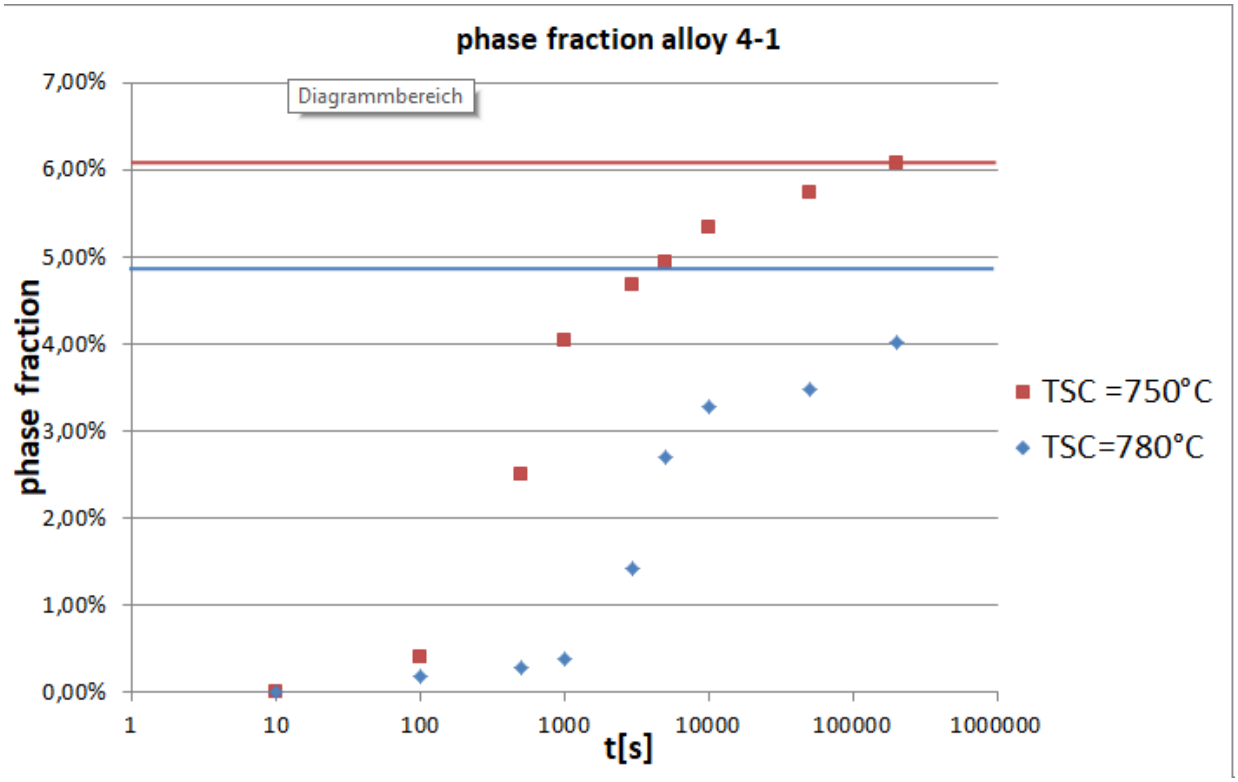

Figure 4.16: evolution of the *SC* phase fraction of alloy 4-1 at 780°C and 750°C, with equilibrium phase fraction, blue and red line present equilibrium fraction for 780°C and 750°C, respectively

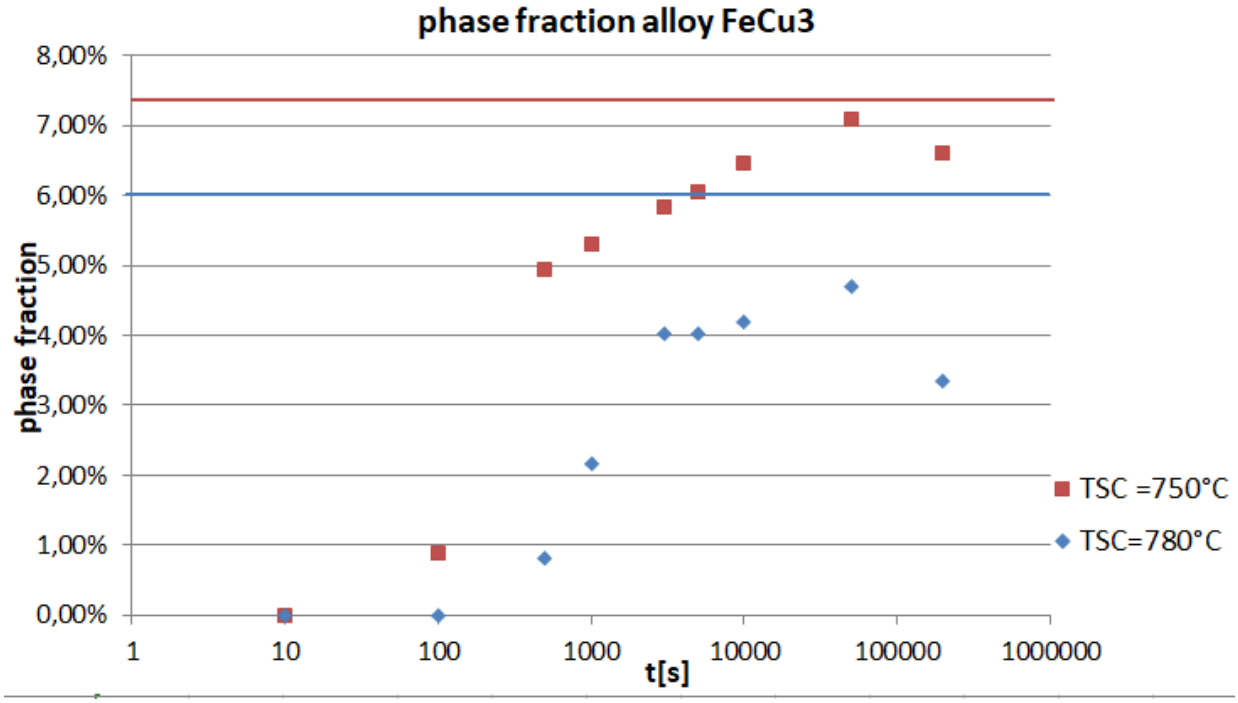

Figure 4.17: evolution of the *SC* phase fraction of alloy FeCu3 at 780°C and 750°C, with equilibrium phase fraction, blue and red line present equilibrium fraction for 780°C and 750°C, respectively

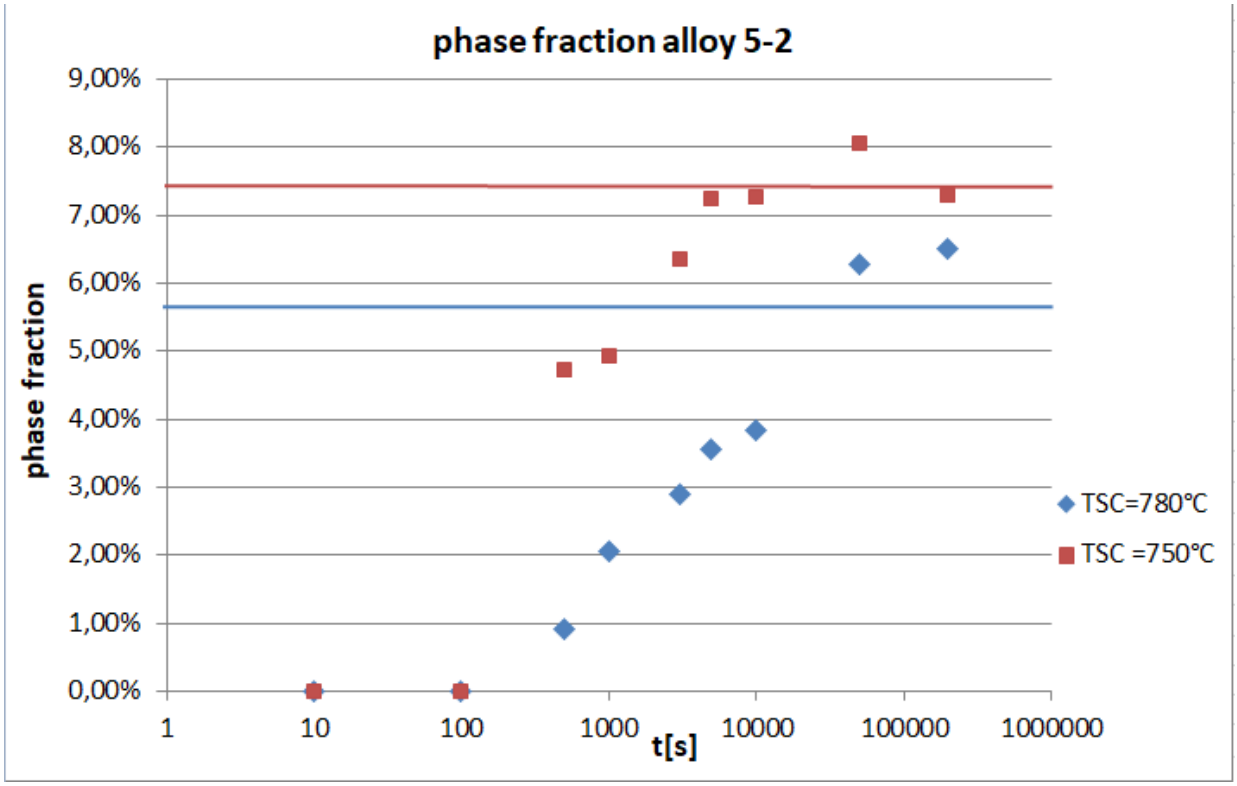

Figure 4.18: evolution of the *SC* phase fraction of alloy 5-2 at 780°C and 750°C, with equilibrium phase fraction, blue and red line present equilibrium fraction for 780°C and 750°C, respectively

that has to do with the considered position in the sectional plane. The microstructure at that certain spot possibly had some heterogeneities that led to deviation. To achieve higher statistical reliability more measurements at more spots would have to be considered.

In Figure 4.16 it can be seen that the developed phase fraction at T_{SC} 750°C is higher than at 780°C. This is as it was expected, see chapter 4.1.2, and leads, with support by the findings shown in Figure 4.9, to the conclusion that the irregularities shown in Figure 4.5 came from the high grade of discontinuity of the grain boundary cementite and the resulting misinterpretation by just measuring in a 2D sectional plane. Following this, the alloying elements in alloys 4-1 seem to lead to quick growth of single spots around the grain, especially at a higher temperature. It takes then much more time than in less complex steel concerning alloying, such as FeCu1 or FeCu3, until a continuous film may build. This effect could not be found for alloy 5-2, although alloying elements are similar, because of massive thickening and the quasi-lamellar shape of the cementite at 750°C isothermal reacting temperature.

Comparison of the equilibrium fraction of cementite calculated with MatCalc and the highest fraction from the experiments after 200000 seconds, which is thought to be sufficiently long to approach equilibrium, shows that growth stagnates after about 10000s annealing time and that the equilibrium fraction value is not reached. Some values, especially with T_{SC} 750°C, exceed the equilibrium fraction, e.g. Figure 4.18 or Figure 4.15. In these cases, we think that these spikes result from inaccuracies during the heat treatment or evaluation step and do not picture the actual growth. After reaching a certain SC fraction further growth becomes sluggish, which was already reported in other studies [9] [11] [12]. In this context it is remarkable that the SC formation at T_{SC} 780°C stabilises far from equilibrium, whereas for T_{SC} 750°C this is not the case. We noticed this behaviour also during the examination of the SC thickness. For further information, we refer to chapter 4.1.2 on page 47.

4.1.4 Austenite-grain size

For this evaluation, we used samples etched with the picric acid solution. For the specimens reacted for a short isothermal reaction time it was not possible to evaluate the former austenite grain size due to the lack of grain boundary cementite. The results of the other experiments showed that the values of the grain size were quite constant and that it was thus not necessary to make further investigations. We may assume that the austenite grain size of the samples for which we could not measure it showed the same behaviour, i.e. negligible variation of grain size.

Table 4.3 shows the values of the evaluated grain size in 3D and its standard deviation. It is seen that a varying T_{SC} between the two chosen isotherms has no significant

Table 4.3: former austenite grain size of the alloys at temperatures 780°C and 750°C

alloy	temperature [°C]	average grain size 3D [µm]	standard deviation 3D
FeCu1	780	180µm	13.4
FeCu1	750	175µm	10.3
4-1	780	54µm	4
4-1	750	52µm	5
FeCu3	780	185µm	31
FeCu3	750	140µm	5
5-2	780	59µm	104
5-2	750	44µm	5

influence on the grain size. The smaller grain size of alloys 4-1 and 5-2 comes from the additional alloying elements. Especially Si, V and Nb have an influence on the grain coarsening during the austenitisation isotherm at 950°C. Among those elements V and Nb form carbides and nitrides and therefore inhibit grain growth. Those carbides and nitrides remain undissolved up to temperatures of about 1000°C [63], [64]. The values from Table 4.3 will be used as the initial grain size for the simulations with MatCalc.

4.1.5 Observed cementite characteristics

Other observations that have been made during examining the SEM and optical microscope images will be described in short in this section. One particularity is the zig-zag morphology of grain boundary cementite. This has been seen quite often, like in Figure 4.19. This sample of alloy 4-1 was isothermal reacted at 780°C for 5000s. This form was already described in other studies [12], [9]. They suggested this would happen to minimise the interfacial energies by maximising the area of low energy facets.

During the examination of the samples, no Widmannstätten cementite was identified. There has only been grain boundary cementite at the former austenite grain boundaries. The studied T_{SC} and t_{SC} have been too high and too long, respectively, for the formation of Widmanstätten cementite. In the raw material, some Widmannstätten cementite has been found, see Figure 4.1.

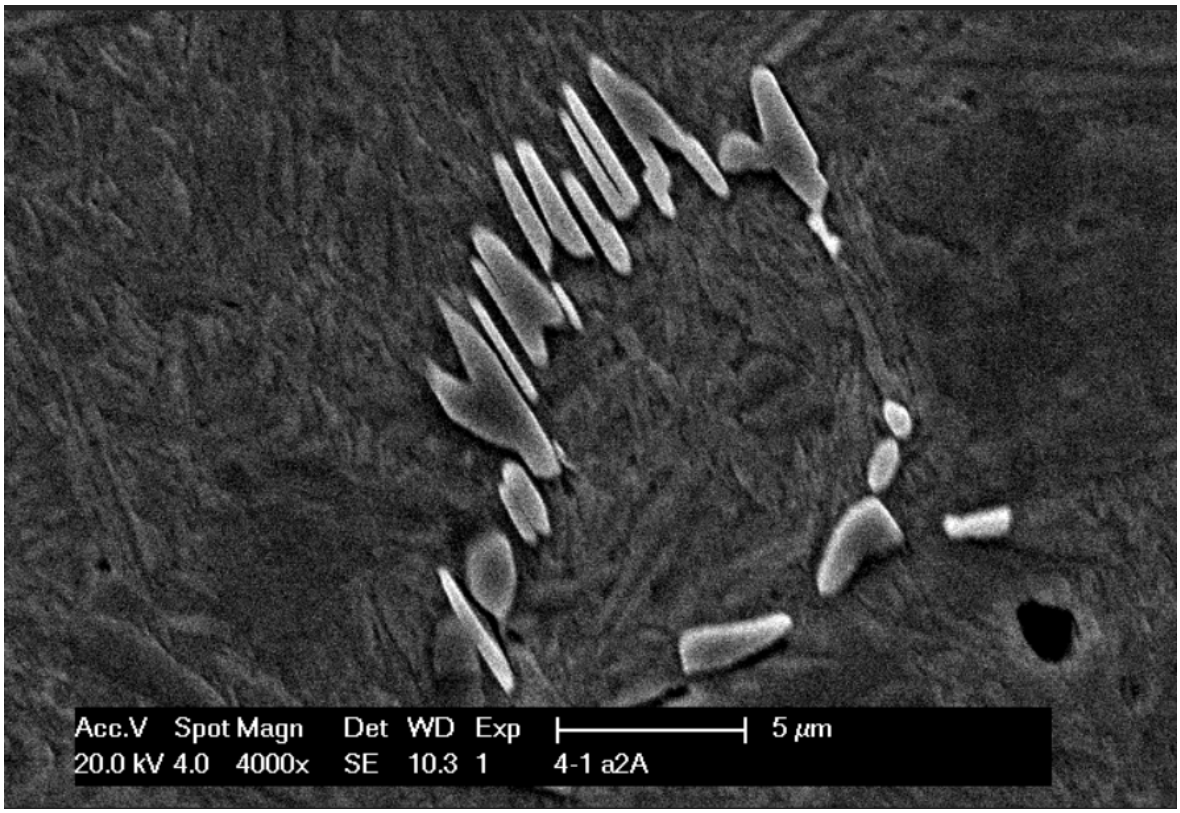

Figure 4.19: zig-zag morphology of grain boundary cementite, sample reacted at 780°C for 5000s.

4.1.6 Summary of the experimental investigations

The findings from chapter 4.1 are summarised as follows. The influence of the isothermal reaction temperature has been seen regarding the grain boundary cementite thickness and phase fraction. The large influence of alloying elements also appeared evident. Especially Si, Mn and Cr were important in that context. They can retard the cementite growth and play an important role in terms of continuity of the grain boundary cementite network [11], [26]. We detected the influence of Si on the continuity of cementite, but we could not deny for sure Cr having a similar effect, due to the composition of the tested alloys. The grain boundary cementite growth stagnated after a certain isothermal reaction time. We did not find clear evidence for the single elements or a combined effect. We could confirm that growth stops after about 10000 seconds and before the equilibrium fraction is reached. Probably, at least partly, the effect of the sluggish growth during long isothermal reacting times and the difference of experimental cementite thicknesses from the expected equilibrium state was also associated with complex inter-relations of alloyed solutes. Even after very long isothermal reacting times (studied 200000s), the equilibrium state was not reached. We suggested that the ledge mechanism contributed to the stagnating grain boundary cementite growth kinetics. The measured thickness values of the grain boundary cementite films were in

a narrow range quite constant. Only a few spikes were observed. From SEM images it was obvious that the grain boundary cementite film in alloys FeCu1 and FeCu3 was more continuous. The direct influence of the grain size on the grain boundary cementite thickness also has been seen. Grain size is controlled by alloying elements, leading to different austenite grain size of the alloys. The grain boundary cementite growth stagnates after a certain isothermal reaction time. Most of the time, the calculated equilibrium thickness is not reached, even after t_{SC} 200000s.

4.2 Computational thermokinetic calculations

The results from the simulations in MatCalc are presented here. We compared the obtained outcome of the simulation with the results from the experiments, see chapter 4.1.

4.2.1 Stepped equilibrium calculation

At first, we made a stepped equilibrium calculation in MatCalc to evaluate the phase fraction of the different phases depending on the temperature. In Figure 4.20 for alloy FeCu1 and alloy 4-1 and Figure 4.21 for alloys FeCu3 and 5-2, the fraction of each phase at a certain temperature at equilibrium can be seen. We used this information

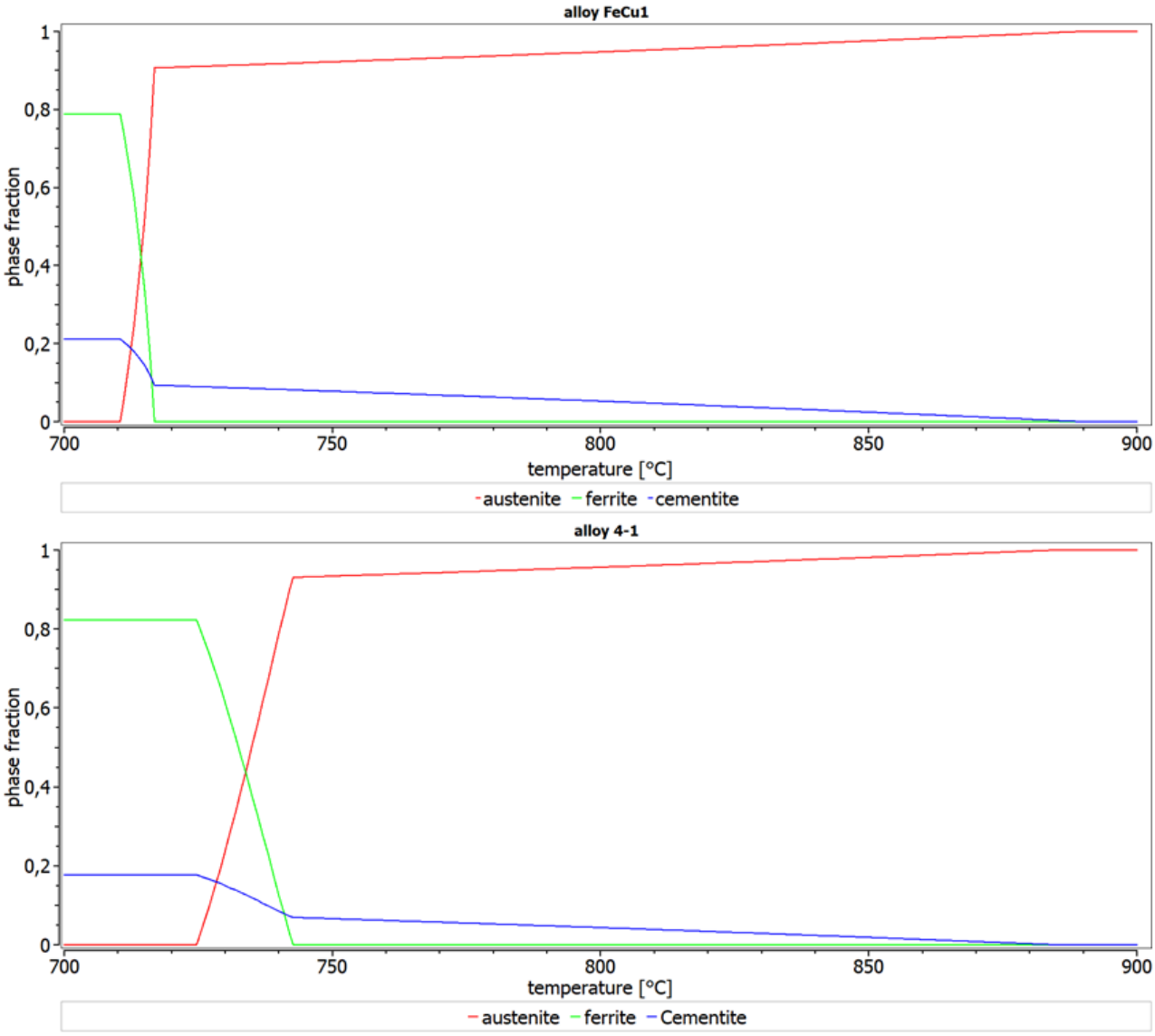

Figure 4.20: stepped equilibrium calculation of alloy FeCu1 (a) and alloy 4-1 (b) with MatCalc

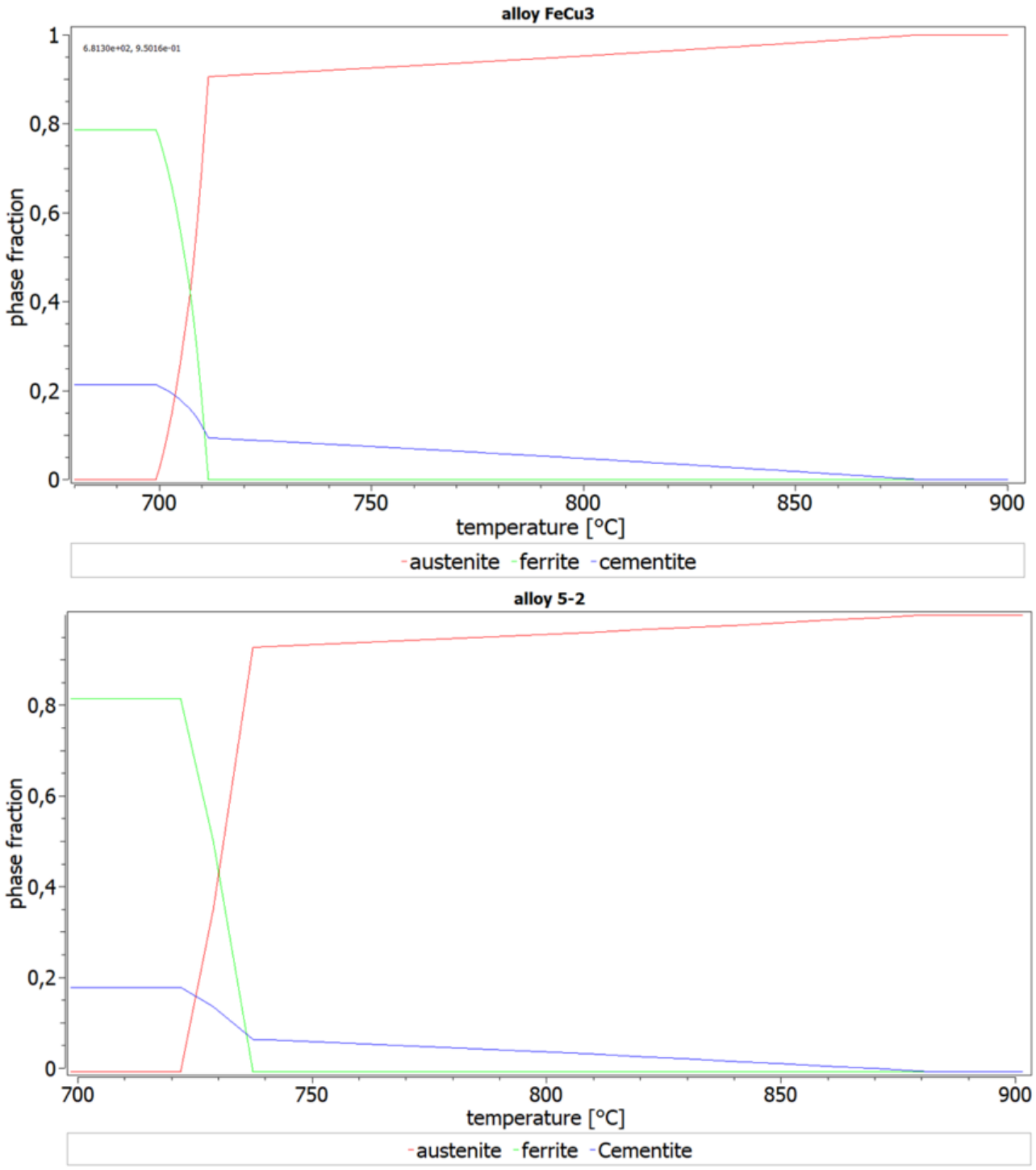

Figure 4.21: stepped equilibrium calculation of alloy FeCu3 and alloy 5-2 with MatCalc

as a reference for all further simulations. One can see in which temperature range cementite under equilibrium is stable. Equilibrium thermodynamics predict for all alloys that the fraction of cementite at 750°C is higher than at 780°C. Table 4.4 show the calculated equilibrium cementite phase fractions of the alloys for the isothermal reaction temperatures T_{SC} 780°C and 750°C.

Table 4.4: equilibrium cementite phase fraction at temperatures 780°C and 750°C

alloy	equilibrium phase fraction at 780°C	equilibrium phase fraction at 750°C
FeCu1	6.3 %	7.8 %
4-1	5.3 %	6.6 %
FeCu3	6.0 %	7.3 %
5-2	5.8 %	7.4 %

4.2.2 Comparison between the results from thermokinetic calculation with Matcalc and the outcome from the experiments

In this chapter, the results from the precipitation calculation are being presented. The simulation was carried out as described in chapter 3.3. The following results for each alloy are calculated with the same calculation parameters, only varying the composition.

Cementite thickness

Figures 4.22, 4.24 4.23 and 4.25 show a comparison of the results from the simulation of the grain boundary cementite thickness in MatCalc with the experiments for T_{SC} 780°C and 750°C for alloys FeCu1, 4-1, FeCu3 and 5-2, respectively. The experi-

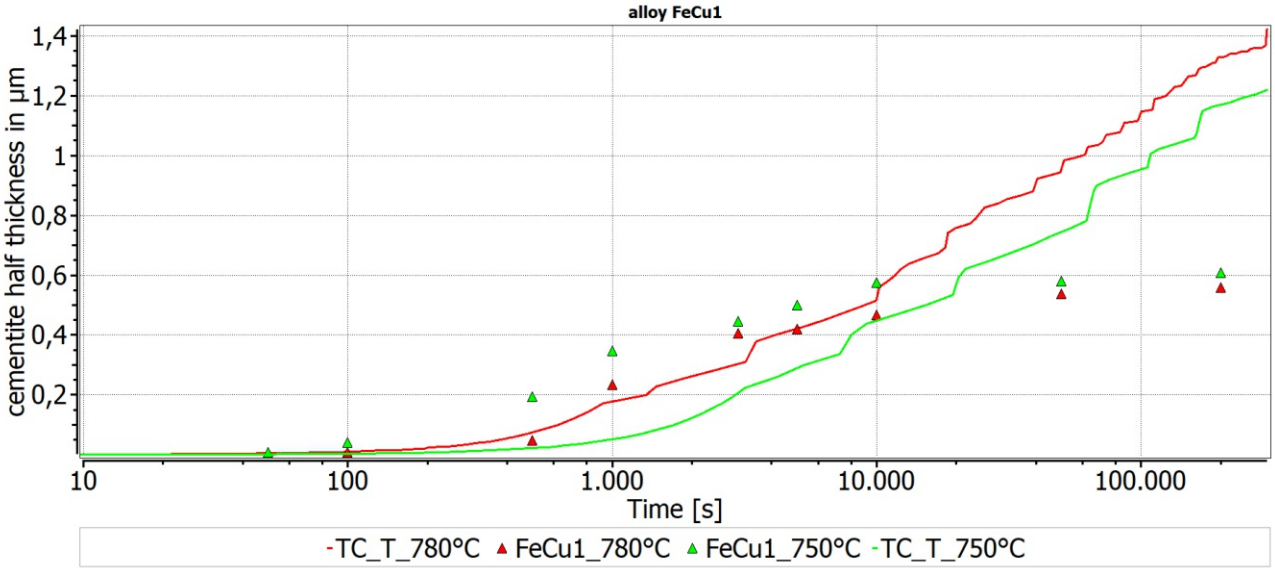

Figure 4.22: comparison of the grain boundary cementite thickness calculated in MatCalc and from the experiments for alloy FeCu1, isothermal reacted with 780°C and 750°C for 300000s, TC T 780°C (thickness cementite, temperature 780°C)

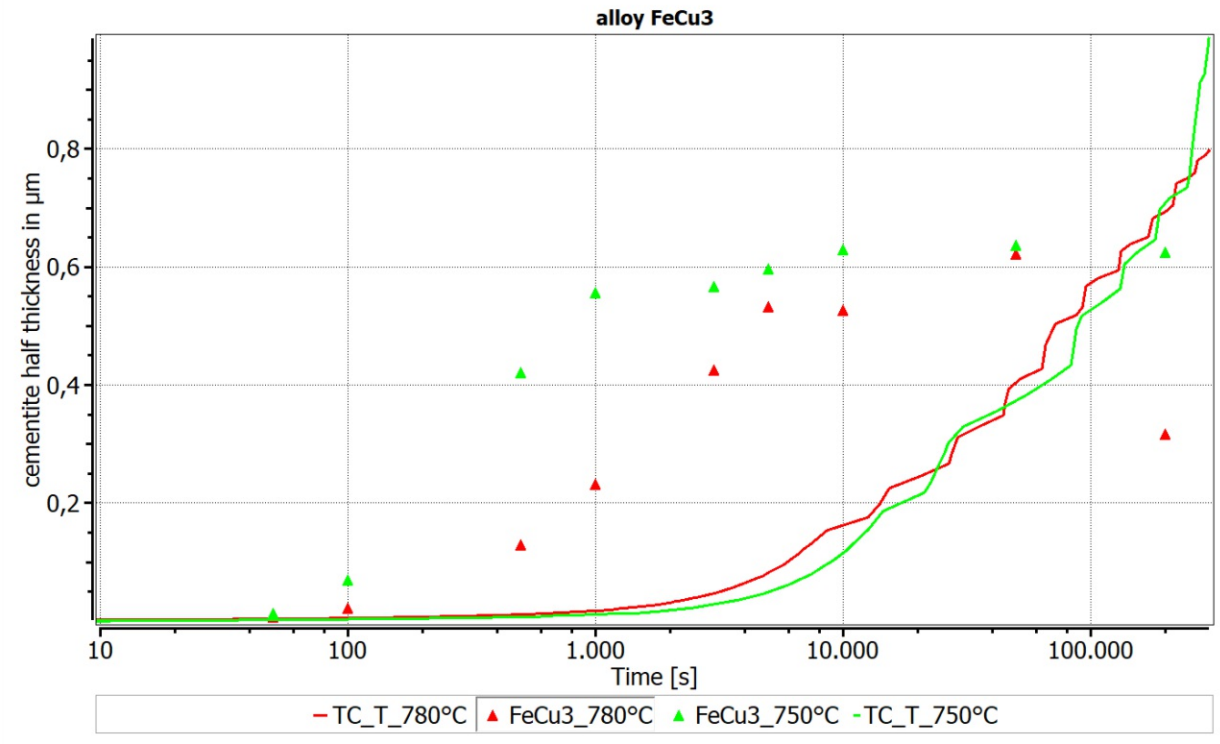

Figure 4.23: comparison of the grain boundary cementite thickness calculated in MatCalc and from the experiments for alloy FeCu3, isothermal reacted with 780°C and 750°C for 300000s, TC T 780°C (thickness cementite, temperature 780°C)

mental data was converted in 3D and adapted with GOC as described in chapter 3.2.3. The simulation for alloy FeCu1 fits quite well with the experiments until about 10000 seconds isothermal reaction time. The evolution of the cementite thickness in the simulation then continues, whereas the experiments showed that the evolution stagnates as soon a certain level is reached. For alloys 4-1, 5-2 and FeCu3 some deviation between simulation and experiment occurs. The simulated growth rate appears significantly lower than in the experiments, whereas the growth start may also be retarded, even though the latter is difficult to evaluate precisely. The simulated growth also does not stop at equilibrium state. When comparing the evolution of the cementite thickness of alloys FeCu1 and FeCu3 (Figures 4.22 and 4.23)) it becomes apparent that Cu retards the formation of SC in the simulation. These two alloys differ only in the amount of Cu, FeCu1 contains 0.5 w% Cu and FeCu3 2.0 w% Cu. In the experiments, this effect did not occur. Further information in chapter 4.2.4. Figures 5.9, 5.10, 5.11 and 5.12 in the appendix show simulation results of the SC thickness of the alloys with an isothermal reaction time of $3x10^9$ seconds. These plots show that the magnitude of SC thickness of the experiments is reached but only with a delay in the simulation of the alloys 4-1, FeCu3 and 5-2. These simulations also showed that the values of the experiments were exceeded by about a factor of two.

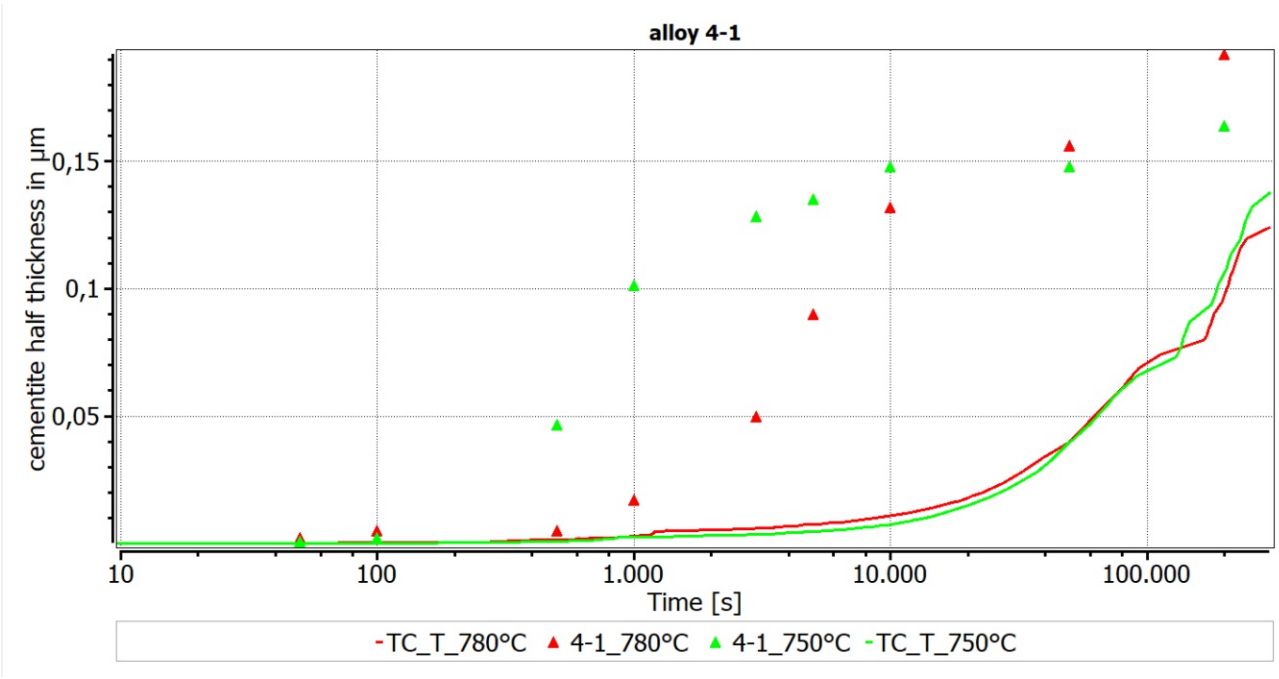

Figure 4.24: comparison of the grain boundary cementite thickness calculated in MatCalc and from the experiments for alloy 4-1, isothermal reacted with 780°C and 750°C for 300000s, TC T 780°C (thickness cementite, temperature 780°C)

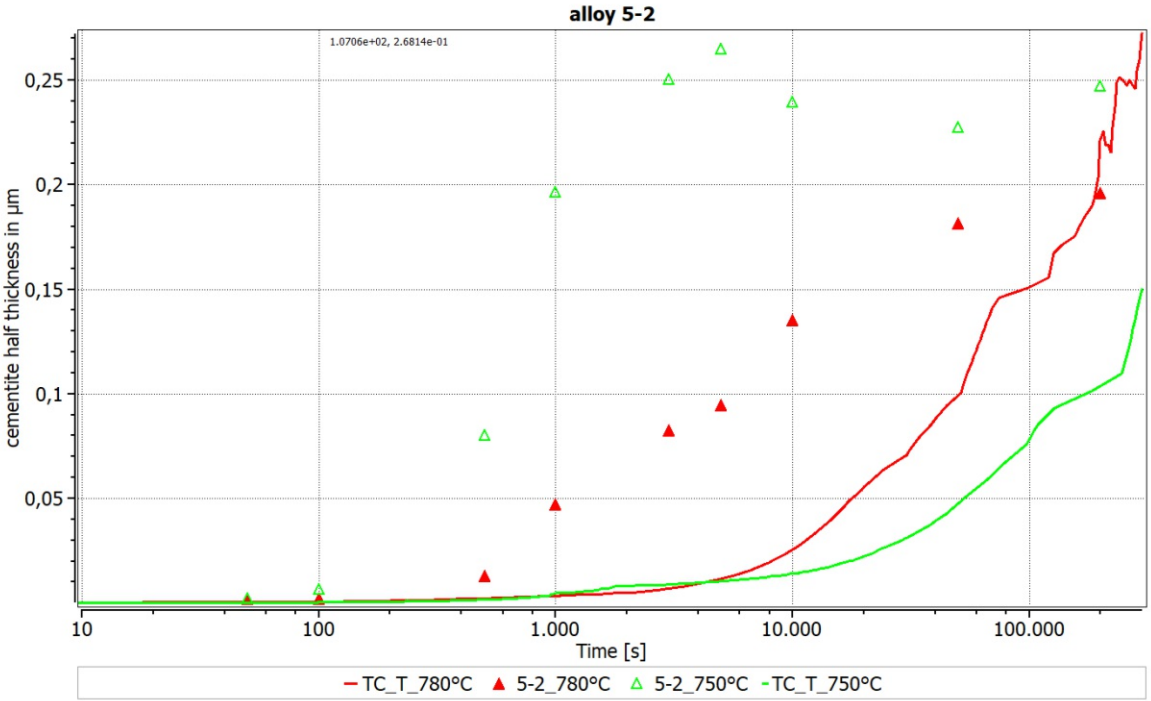

Figure 4.25: comparison of the grain boundary cementite thickness calculated in MatCalc and from the experiments for alloy 5-2, isothermal reacted with 780°C and 750°C for 300000s, TC T 780°C (thickness cementite, temperature 780°C)

Cementite fraction

Figures 4.26, Figure 4.28, 4.27 and 4.29 show a comparison between the results of the phase fraction from MatCalc and the experimental results. The triangles in the graphs show the results of the experiments. It is seen that the equilibrium phase fraction

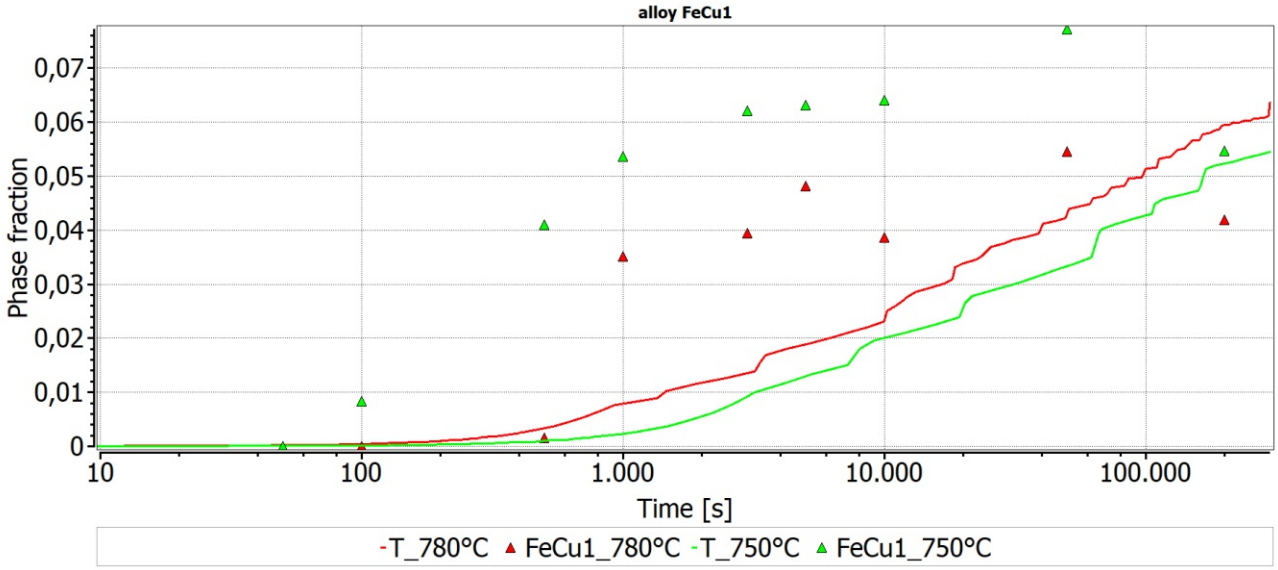

Figure 4.26: comparison of the phase fraction of grain boundary cementite calculated with MatCalc and from the experiments for alloy FeCu1, isothermally reacted at 780°C and 750°C for 300000s

nearly is reached for alloy FeCu1. For all the other alloys a quite large deviation from equilibrium exists. The behaviour of the plots of the phase fraction is similar to the plots of the cementite thickness. The growth of SC in the simulation starts with a delay, as observed in the plots of the cementite thickness and reaches equilibrium fraction with a delay. In the simulations, it was seen that the initial grain diameter plays an important role, which is a confirmation of the observations from the experiments. It has a significant influence on the available amount of carbon and potential nucleation sites.

The actual thickness of the *SC* film in the simulation is evaluated via the cementite phase fraction and the total grain boundary area(see Equation 3.3). Therefore a direct correlation exists between the simulated film thickness and the phase fraction. The only influencing parameter, besides the calculated phase fraction, is the initial austenite grain diameter (see equations 4.3 and 3.3). The used initial austenite grain diameter in the simulation are the ones evaluated in the experiments, see chapter 4.1.4.

The discrepancy of the inverted magnitude of phase fraction with temperature in the simulation, as compared to experimental results, and therefore also cementite thickness between the two isothermal reaction temperatures, is obvious. Theory suggests and

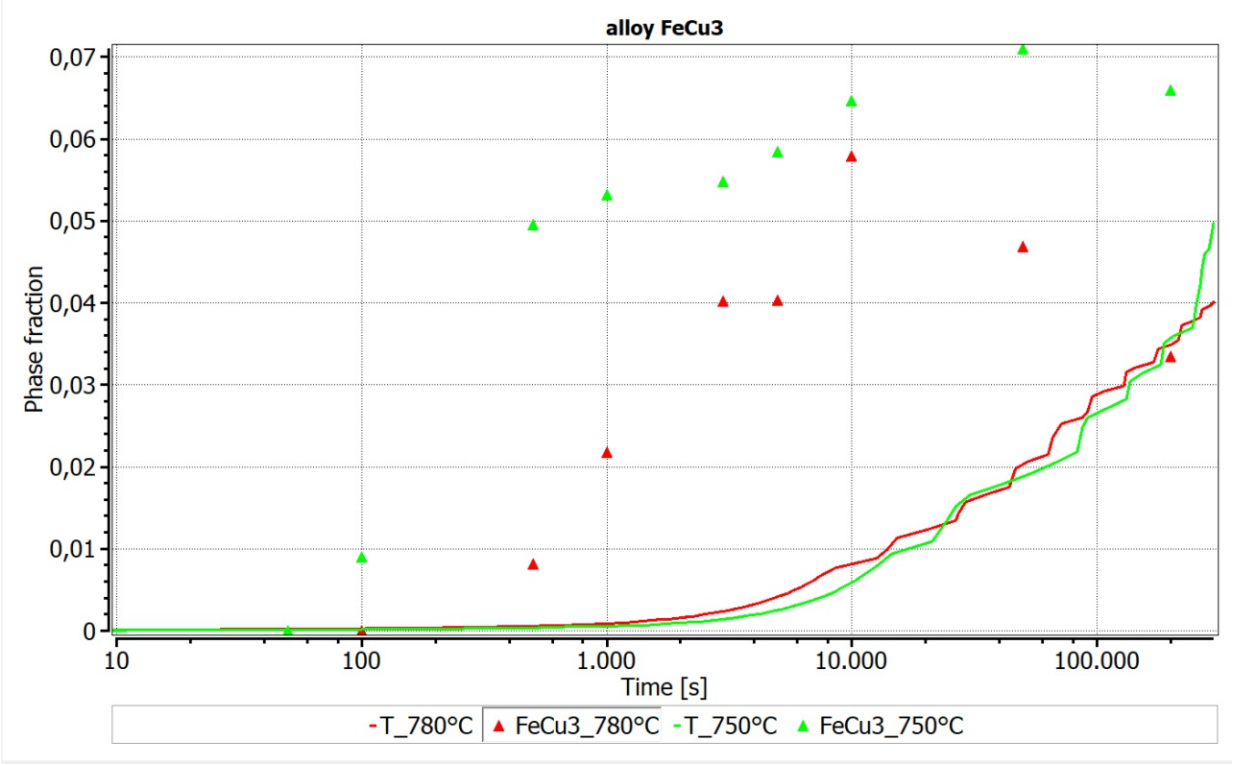

Figure 4.27: comparison of the phase fraction of grain boundary cementite calculated with MatCalc and from the experiments for alloy FeCu3, isothermally reacted at 780°C and 750°C for 300000s

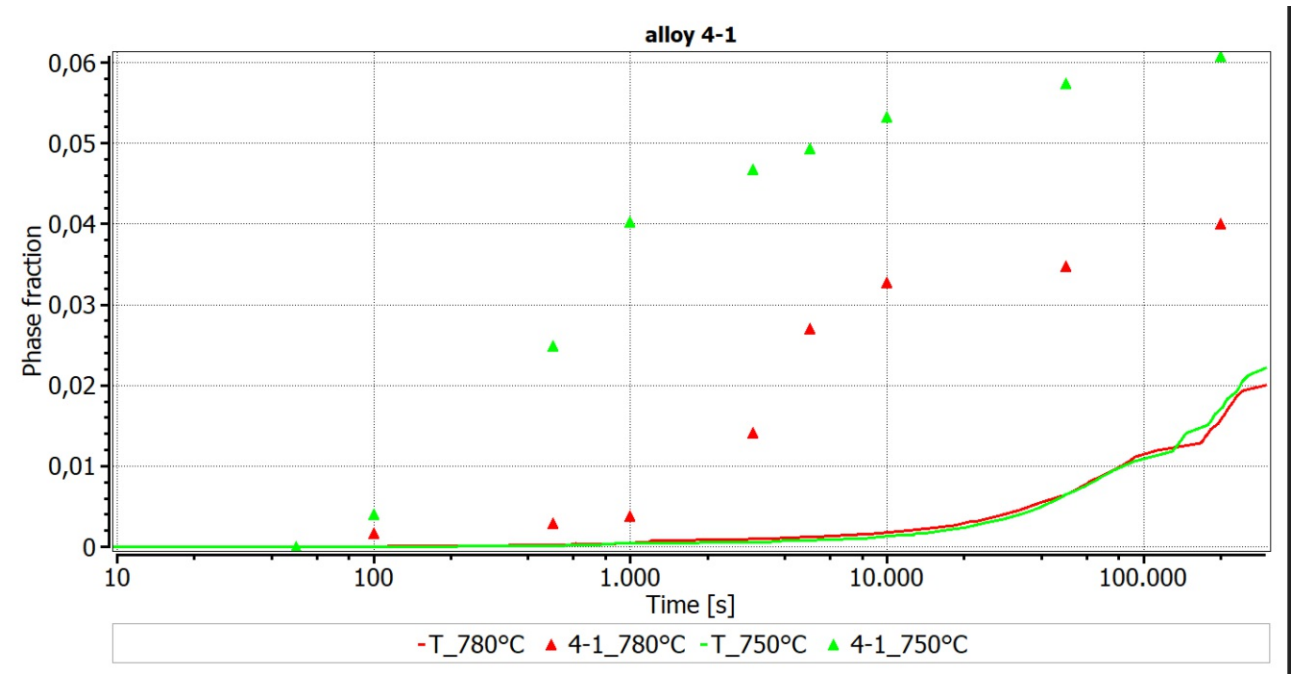

Figure 4.28: comparison of the phase fraction of grain boundary cementite calculated with MatCalc and from the experiments for alloy 4-1, isothermally reacted at 780°C and 750°C for 300000s

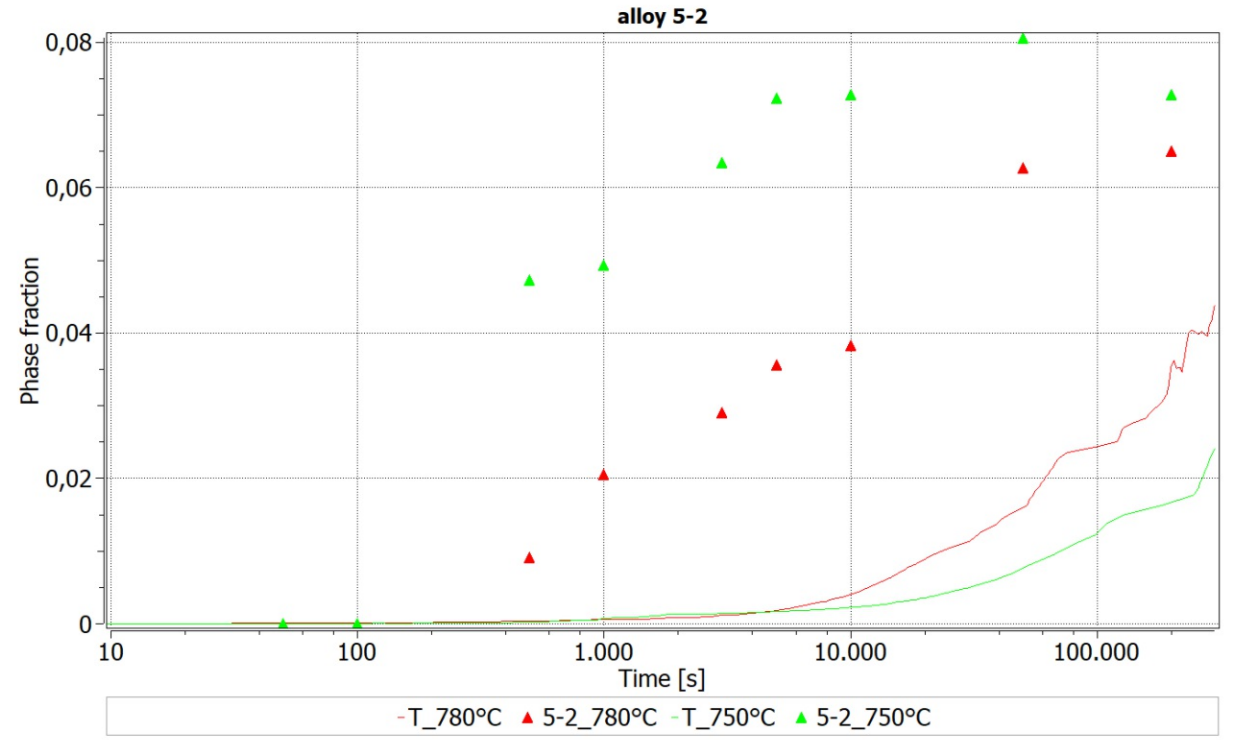

Figure 4.29: comparison of the phase fraction of grain boundary cementite calculated with MatCalc and from the experiments for alloy 5-2, isothermally reacted at 780°C and 750°C for 300000s

the experiments showed that basically at a lower isothermal reaction temperature more grain boundary cementite, due to the higher driving force, should form. Figures 4.30 and 4.31 for alloy FeCu1 and alloy 4-1, respectively, show the evolution of the chemical potential of Carbon in the austenite phase and the driving force of cementite. The same do Figure 4.32 and Figure 4.33 for alloy FeCu3 and 5-2, respectively. Driving

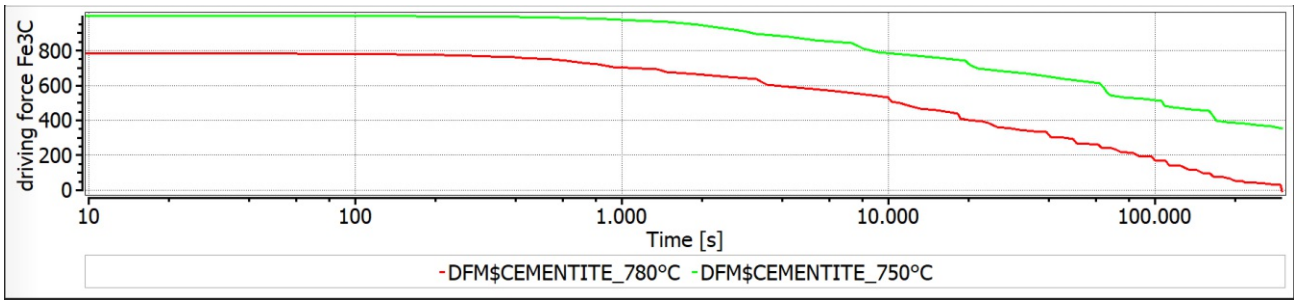

Figure 4.30: occurring chemical potential of C in austenite phase (MUP-FCCA1) and driving force of cementite (DFM-Cementite) in J/mole for the precipitation calculation of alloy FeCu1

force is an indicator of the tendency of a system to evolve and can be interpreted as the motivation of a system to evolve. As said before the driving force for 750°C T_{SC} is higher than for 780°C T_{SC}. So basically, taking only the driving force into

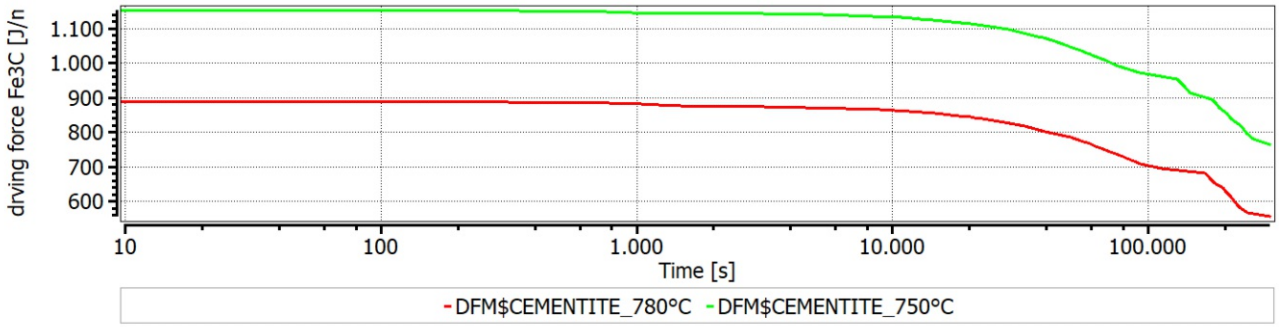

Figure 4.31: occurring chemical potential of C in austenite phase (MUP-FCCA1) and driving force of cementite (DFM-Cementite) in J/mole for the precipitation calculation of alloy 4-1

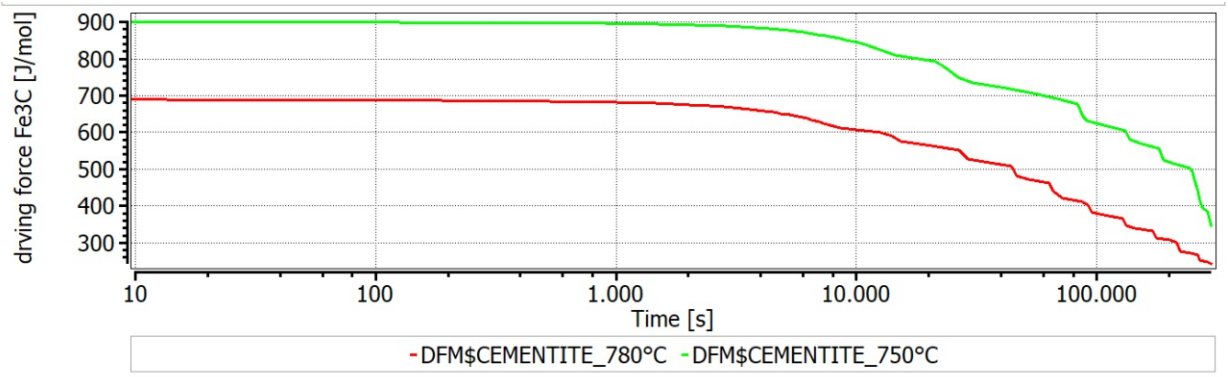

Figure 4.32: occurring chemical potential of C in austenite phase (MUP-FCCA1) and driving force of cementite (DFM-Cementite) in J/mole for the precipitation calculation of alloy FeCu3

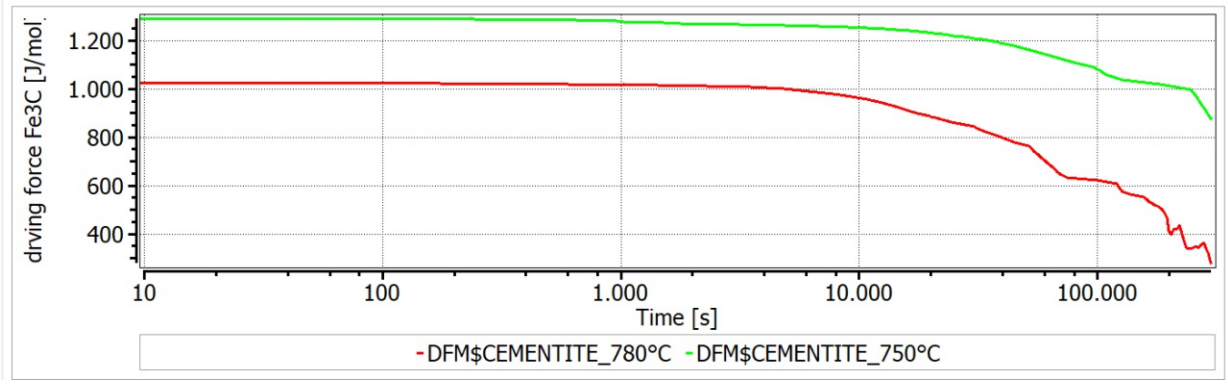

Figure 4.33: occurring chemical potential of C in austenite phase (MUP-FCCA1) and driving force of cementite (DFM-Cementite) in J/mole for the precipitation calculation of alloy 5-2

account, the system tends to build a higher amount of cementite at the lower isothermal reaction temperature. Also the behaviour of the chemical potential of the cementite phase point in that direction. The reason for the inverted behaviour of the cementite evolution in the simulation is not clear. A possible hypothesis is a slower alloying element distribution at 750°C due to smaller diffusion coefficient.

Another interesting investigation was the behaviour of the simulation towards the end of the reaction. The simulation with alloy FeCu1 reaches a state of saturation. This is also confirmed by the plot of the driving force (Figure 4.30). In contrast, for alloy 4-1 at the end of the simulation at 300000s, the driving force has still a quite high value. It does not reach zero as in the simulation for FeCu1. This means that a saturation state has not been reached yet and the cementite in simulation 4-1 will tend to grow further. The system has still some "motivation" for further growth. Alloys 5-2 and FeCu3 also tend to further growth just like alloy 4-1.

4.2.3 Investigations of MatCalc parameter adaptation

In this subsection, the findings from several simulation attempts with varying simulation parameters will be presented.

Parameter study

In this chapter, we will give an overview of the parameter in the simulation with MatCalc. We did this to examine the influence of the parameters on the result of the simulation. We evaluated the influence of the parameters on the results qualitatively. The simulations for the parameter variation were carried out with the composition of the alloy FeCu1 and at 780°C isothermal reaction temperature. The classification follows the notation and GUI architecture in MatCalc (Version 6.04 rel 0.0.46). The exact adjustment of the settings calculated can be seen in table 3.5. For further information regarding the simulation in MatCalc, see chapter 3.3.

- Precipitation domains
  - Initial grain diameter: This parameter depends on the production process and the anterior heat treatment. It directly influences the grain boundary thickness by affecting the amount of carbon per grain, further information in chapter 4.1.2. The initial grain size diameters were evaluated during the practical part of this work, see chapter 4.1.4.
  - Equilibrium dislocation density: The dislocation density directly influences the number of nucleation spots. With increasing dislocation density also the

phase fraction and SC thickness increases in the simulation. This value is dependent on the production process of the material.

- Phase status
  - Nucleation
    - Nucleation constant: The default value for this setting is one. A variation did not lead to significant change.
    - Nucleation site efficiency: The default value for this setting is one. Variating this setting did not lead to significant change.
    - Sites
      - Nucleation sites: This setting directly influences the number of nuclei. Depending on the chosen nucleation sites the diffusion geometry also gets influenced. In MatCalc the appropriate diffusion geometry can only be reached if grain boundary is selected as a nucleation site. Simulations showed that choosing grain boundary corners and edges as nucleation sites leads to a delay of the cementite formation in the simulation and a smaller number of precipitates. The phase fraction and thus also the SC thickness was lower, compared with the setting grain boundary.
      - Grain boundary diffusion geometry [60]:

        a) Random distribution (spherical): This setting led to an earlier and faster growth of the SC, compared with the default setting "Grain boundary (automatic)".

        b) Grain boundary (conical): This setting led to a delay in nucleation and thus slower growth, compared with the default setting "Grain boundary (automatic)".

        c) Grain boundary (automatic): This is the default setting. The gained results were closest to reality.
      - Grain boundary matrix diffusion enhancement factor(gb-mdef) [61]: A deviation from the default value (three for this simulation) influenced the precipitation kinetics. Increasing this value led to faster SC precipitation, whereas decreasing led to a delay.
    - Controls:
      - Suppress nucleation outside CNT regime: Choosing this setting did not influence the SC kinetics.

- Use volumetric misfit: Choosing this setting does not influence the SC kinetics.
- Ignore misfit stress during deformation: Choosing this setting did not influence the SC kinetics.
- Use heterogeneous site energy: Choosing this setting increased the accuracy of the results of the simulation compared with the experiments. Nucleation started earlier and growth proceeded faster [60], for further information see chapter 3.3.
- Incubation time constant: The default value for this setting is one. But a variation did not lead to significant change.
- Composition: The nucleation occurred a lot earlier and the growth a lot faster under para-equilibrium conditions than under ortho-equilibrium conditions, see chapter 4.2.3.

– Precipitate:

* Diffuse interface effect: With two phases in contact, some mixing of the phases is expected rather than a sharp interface. In this diffusive interface, the number of broken bonds is different than at a sharp interface, which is accounted for by this setting. Choosing the setting "diffuse interface effect" together with T_{crit} provided an "alternative" to the setting "use heterogeneous site energy" when aiming for accurate results. [65]

  Regular solution T_{crit}[K]: T_{crit} is defined as the highest temperature at which two phases are present in the system. Good values for T_{crit} were between 1100 and 1400 K to achieve accurate results compared to reality. With higher T_{crit}, SC growth was more sluggish, whereas with lower values the simulated SC growth was excessive.

Type of nucleation equilibrium composition and alloying elements

An important parameter influencing precipitation simulations is the choice of para-equilibrium or ortho-equilibrium nucleation composition state [66]. It changes the way substitutional and interstitial alloying elements are considered in the simulation. Under paraequilibrium conditions, only diffusion of interstitial elements, such as carbon, is possible, whereas all substitutional elements are "frozen". Paraequilibrium conditions occur at temperatures where diffusion for substitutional elements is not possible. Under equilibrium or orthoequilibrium conditions full equilibrium occurs without any

constraints, which means that partitioning of substitutional alloying elements is necessary for precipitation. Both conditions are only an approximation to reproduce reality. Following Bhadhesia it is quite likely that at the interface neither of these two conditions occurs. It would be more likely that a mixture between those idealised states prevails[14, chapter 4]). This was also confirmed by Hillert and Ågren [35]. Figure 4.34 shows a precipitation simulation for alloy FeCu1 where the red line shows the evolution for ortho-equilibrium state and the green line for paraequilibrium state. Nucleation oc-

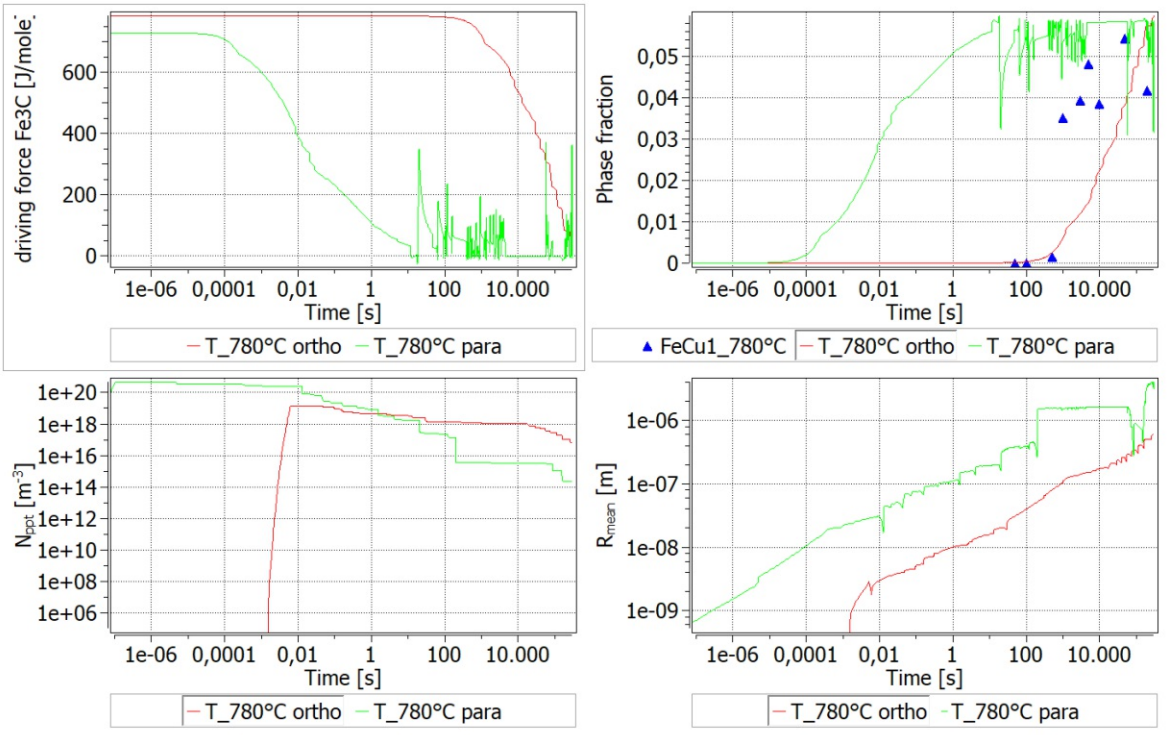

Figure 4.34: comparison of precipitation simulation between ortho- (red) and paraequilibrium (green) composition state for alloy FeCu1 at 780°C isothermal reacted

curs a lot earlier and growth a lot faster under paraequilibrium conditions than under ortho-equilibrium conditions. After having reached proximity to the equilibrium fraction, the phase fraction function begins to oscillate. This effect comes from numerical issues in the calculation. The situation changes when a small amount of silicon is added to the system in the simulation, and the precipitation completely stops. In the simulation, this effect appears with an amount of Si bigger than 0.1 w%. Kozeschnik et. al [30] report that Silicon would change the Gibbs free energy of the system considerably. They explain the retardation of cementite precipitation caused by a small amount of silicon as following, "... Cementite, when it forms under para-equilibrium conditions, traps the Silicon as it grows."[30] Therefore the speed of the cementite precipitation decreases in comparison to equilibrium conditions.

Evaluation of the austenite grain boundary area

One important task was to get an accurate comparison between the data from the experiment and the calculated values from MatCalc. In MatCalc, it is not possible to simulate directly the growth of a film surrounding a grain. Therefore the actual grain boundary cementite half-thickness was calculated via the phase fraction and the austenite grain boundary area. The number of grains, n_G, in a 1 m^3 volume can be described only through the input variable d, see Eq. 4.1. The variable d is the grain diameter.

$$n_G = \frac{1m^3}{V_{SG}} = \frac{1}{8d^3\sqrt{\frac{2}{10^3}}} \tag{4.1}$$

$$V_{SG} = 8\sqrt{2} * (\frac{d}{\sqrt{10}})^3 \tag{4.2}$$

The initial grain diameter d is kept constant during the calculation, which also means that the initial number of grains is the same as at the end of the simulation. This assumption can be made because the actual grain growth at the reaction temperatures T_{SC} is negligible, see Table 3.3. With the surface area from a single grain, A_{SG}, Formula 2.111 [37, p.85], the total grain boundary area then is:

$$A_G = n_G\frac{A_{SG}}{2} = \frac{1}{8d^3\sqrt{\frac{2}{10^3}}}\frac{1}{2}(\frac{d^2}{10}(8+12\sqrt{3})) \tag{4.3}$$

4.2.4 Retardation of cementite evolution due to substitutional solutes Cu or Mn

Examining the role of substitutional solutes in complex steels for cementite kinetics is important. Moreover, simulation is validated by comparison with experiments. It is interesting to see the simulated retardation due to substitutional elements such as Si, Mn, or Cu. Even small amounts of substitutional alloying elements have a big influence on the behaviour of the simulated cementite kinetics. Figure 4.35 shows the contrast between two almost identical simulations. The red curve shows the result of the regular FeCu1 composition and the green one of pure Fe-C. For the pure Fe-C simulation, the Cu and Mn content was decreased to 0.0001 w% to avoid numerical inconsistencies. The blue points in the right upper quarter show the result of the phase fraction from the experiments with alloy FeCu1 and 780°C. The red points in the left upper quarter show the results for the SC half-thickness of the experiments with FeCu1 at T_{SC} 780°C. The green points show the result from Heckel and Paxton [9], for Steel F (binary Fe-C) and T=800°C. The different behaviour of the data from Heckel and Paxton can be explained as follows. The isothermal reaction temperature

for the data from Heckel and Paxton was 800°C and not 780°C. Heckel and Paxton

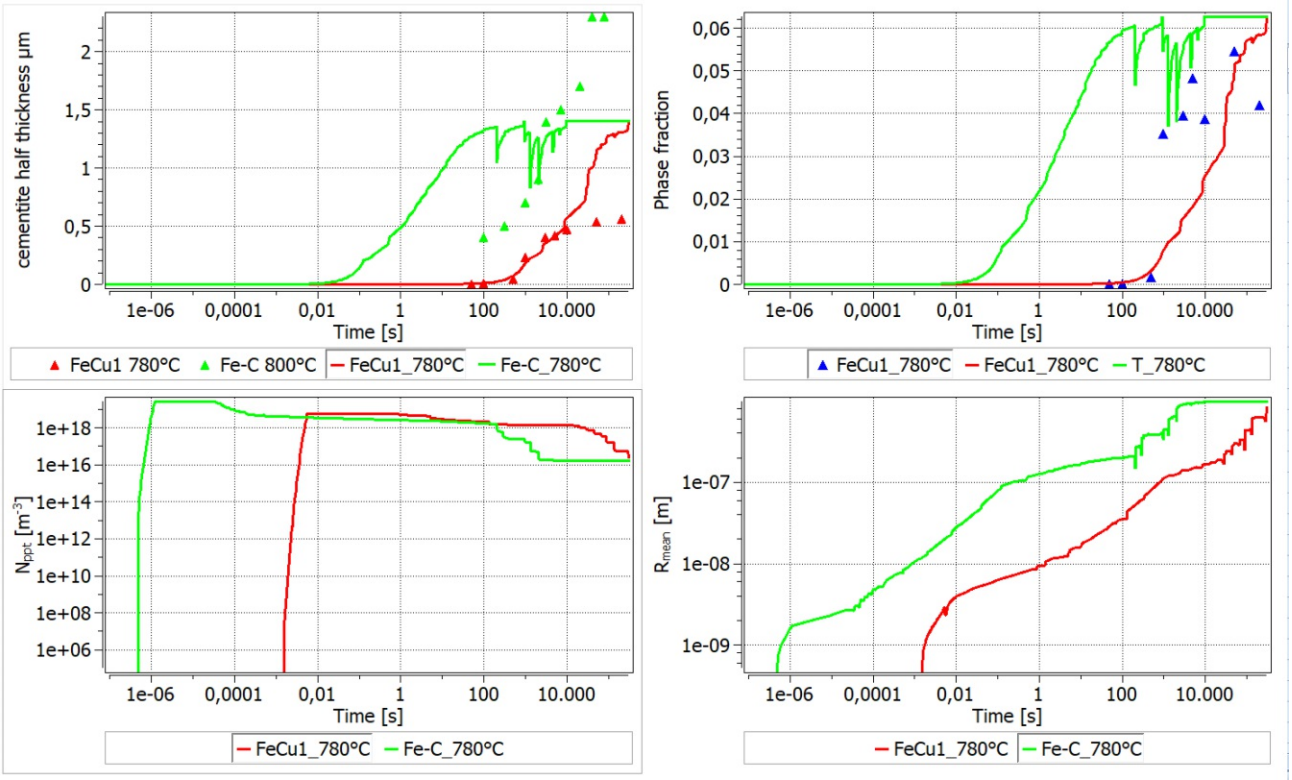

Figure 4.35: comparison of precipitation simulation between between alloy FeCu1 (red line) and binary Fe-C with 0.0001 w% Cu and 0.0001 w% Mn (green line) at 780°C isothermally reacted, data from Heckel and Paxton, Steel F, 800°C (green points) [9] and experimental results (red and blue points)

converted the data following Equation 3.1 and did not convert the data with factor G, see chapter 3.2.3. When comparing the result of the simulation with the data from Heckel and Paxton for the binary Fe-C composition, it seems as if the growth in the simulation would be faster. No further data of experimental results with binary Fe-C were available, therefore a more precise assumption can not be made. The left lower quarter shows the number of nuclei. There it gets apparent that nucleation in the binary Fe-C starts a lot earlier than in the regular FeCu1. When observing the plots in figures 4.35, 4.36, 4.37 one needs to be aware of the logarithmic scale at the axis of abscissae. Taking the logarithmic scale into account the plot of the mean radius (R_{mean}[m]) in figure 4.35 shows a delay in the formation of cementite of several orders of magnitude between the two reviewed alloys. The same can be said about the number of nuclei (N_{ppt}) in figure 4.35. It becomes obvious that the substitutional alloying elements Mn and Cu have a tremendous delaying influence compared to basic Fe-C, and change the shape of the kinetic curve enormously.

Figure 4.36 shows a simulation of the cementite film half thickness and the driving force of cementite in the precipitation domain. The green curve stands for the alloy

FeCu1 with 1w%Mn and 0.5 w%Cu and the red curve for the same composition, but with only 0.0001w%Mn and 0.5 w%Cu.

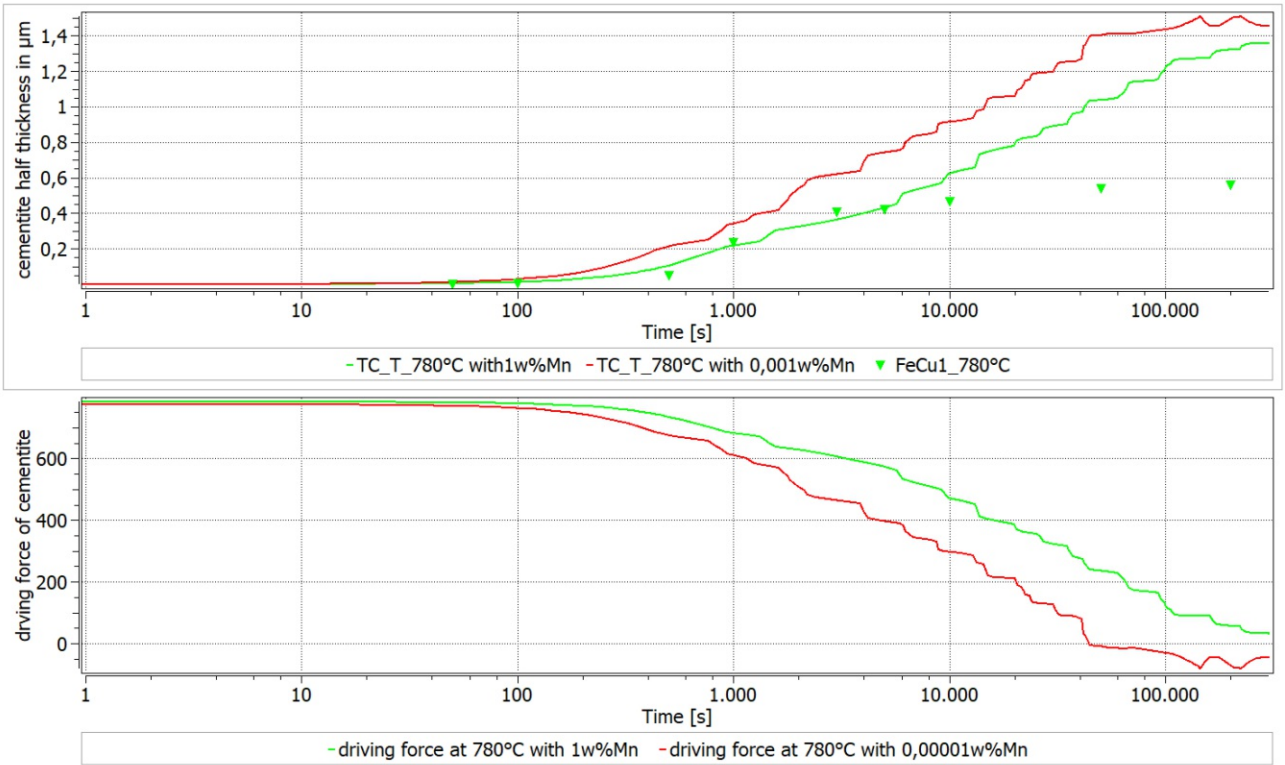

Figure 4.36: influence of manganese content on the evolution of cementite and the driving force of cementite, green line stands for the regular composition of alloy FeCu1 and the red line stands for a composition with only 0.0001w%Mn. The green points show the results of the SC half thickness of the experiments with FeCu1

The green points represent the results from the experiments with FeCu1 and T_{SC} 780°C. The Cu content is kept constant. With a lower Mn content a higher amount of cementite precipitates. In the lower half of Figure 4.36, the driving force shows the retarding influence of the Mn. At the initial state, the driving forces tend to be the same, the one with 1 w% Mn (green line) is even a bit higher, implying that this composition is more likely to induce precipitation. With an increasing fraction of already precipitated cementite the driving force decreases, until under equilibrium, the driving force becomes zero. In MatCalc, a negative driving force of a phase would mean that this phase is not stable under these particular circumstances. Even though some retarding effect of substitutional elements on the cementite evolution has been shown also experimentally, one needs to be careful with the interpretation of the very strong simulative retardation. Further investigations are required to decipher possible reasons that may have caused this effect in the simulation. Figure 4.37 shows a comparison of the experimental and simulation results of FeCu1 and FeCu3. Green and red represent

the alloys FeCu1 and FeCu3, respectively, which only differ by the amount of Copper in the composition. The experimental results of those two alloys at T_{SC} 780°C do not deviate, neither do they at 750°C. Reviewing the simulation results, it gets apparent that the higher amount of Cu in FeCu3, 2.0 w% compared to 0.5 w% Cu in Fecu1, retards the SC formation. In the simulation for FeCu1 (0.5 w% Cu) already retarda-

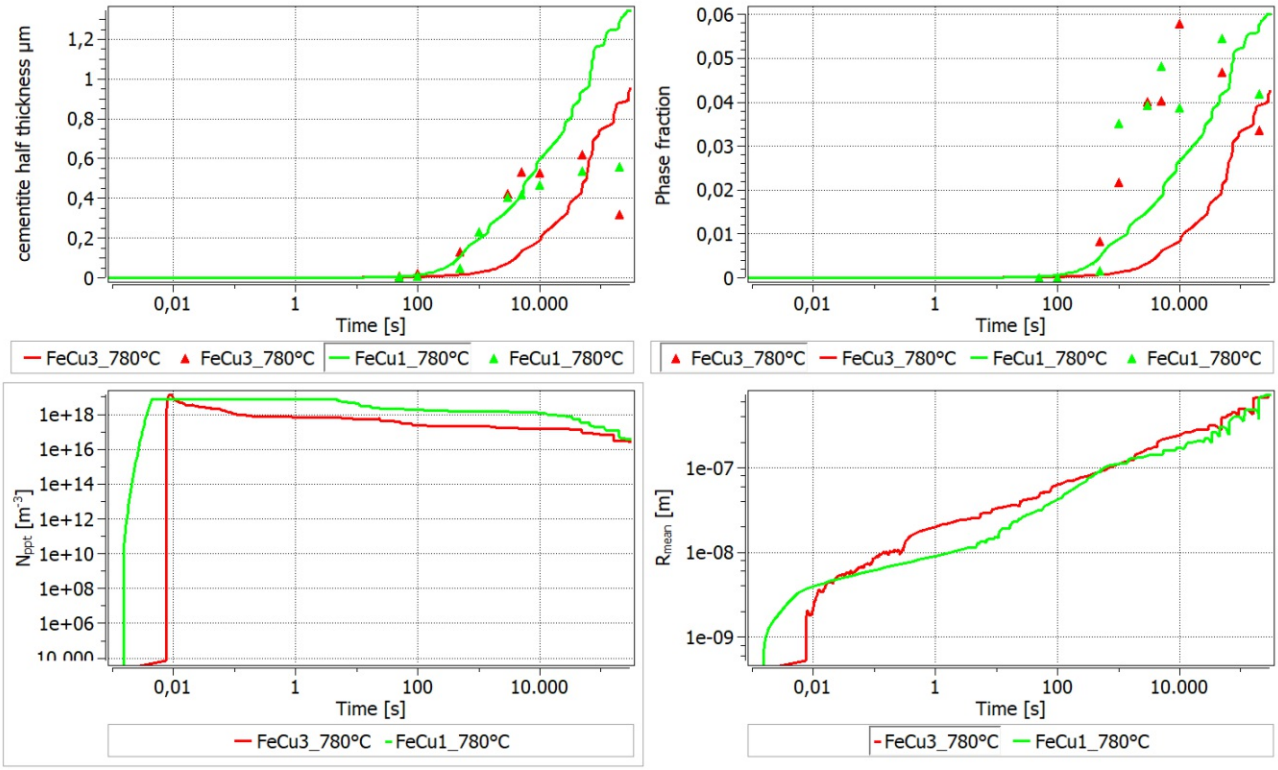

Figure 4.37: influence of Copper content on the evolution of cementite and the driving force of cementite, green line represents FeCu1 with 0.5 w% and the red line stands for FeCu3 with 2 w% Cu

tion occurs, see Figure 4.35, which increases with an increasing amount of Cu in the composition. We observed a retarding behaviour for all made simulations for Cu and Mn, see Figures 4.35, 4.36 and 4.37, which increases with increasing alloying element content.

4.2.5 Influence of Vanadium on the formation of grain boundary cementite

We found an interesting shape of cementite in alloy 5-2 for T_{SC} 750°C. Figure 4.38 shows typically observed forms for t_{SC} 500s (a) and t_{SC} 10000s (b) and T_{SC} 750°C, also reported in chapter 4.1.2. Bhadeshia and Honeycombe [14] state that about 1.0 w%V could dissolve in austenite. We first considered that carbides would not play a role for this quasi-lamellar cementite shape. Taking the composition of alloy 5-2 into

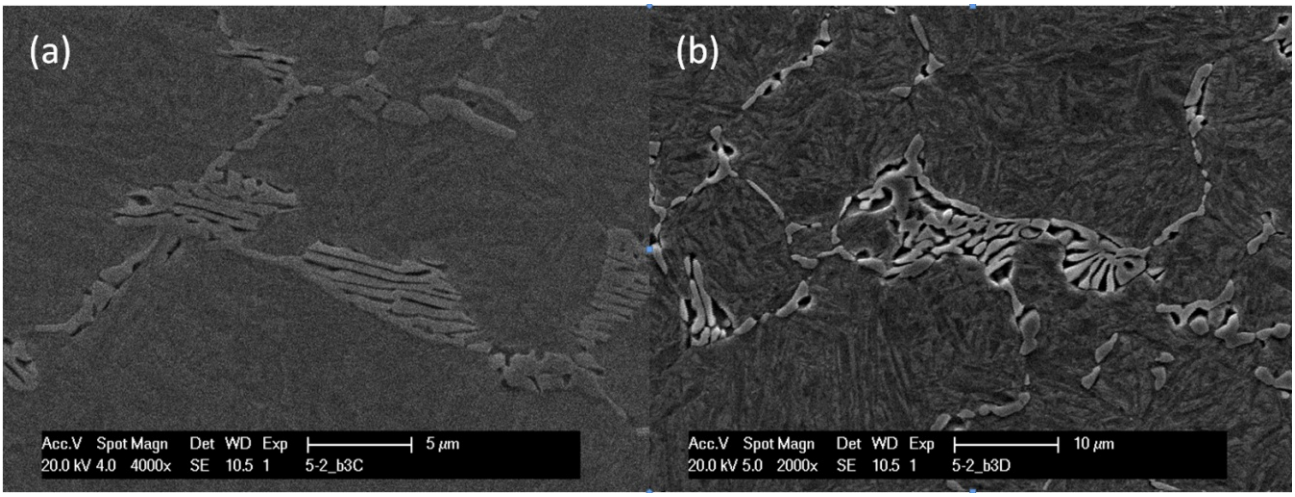

Figure 4.38: shape of grain boundary cementite in alloy 5-2 isothermally reacted at 750°C, a) reaction duration t_{SC} 500s, b) reaction duration t_{SC} 10000s

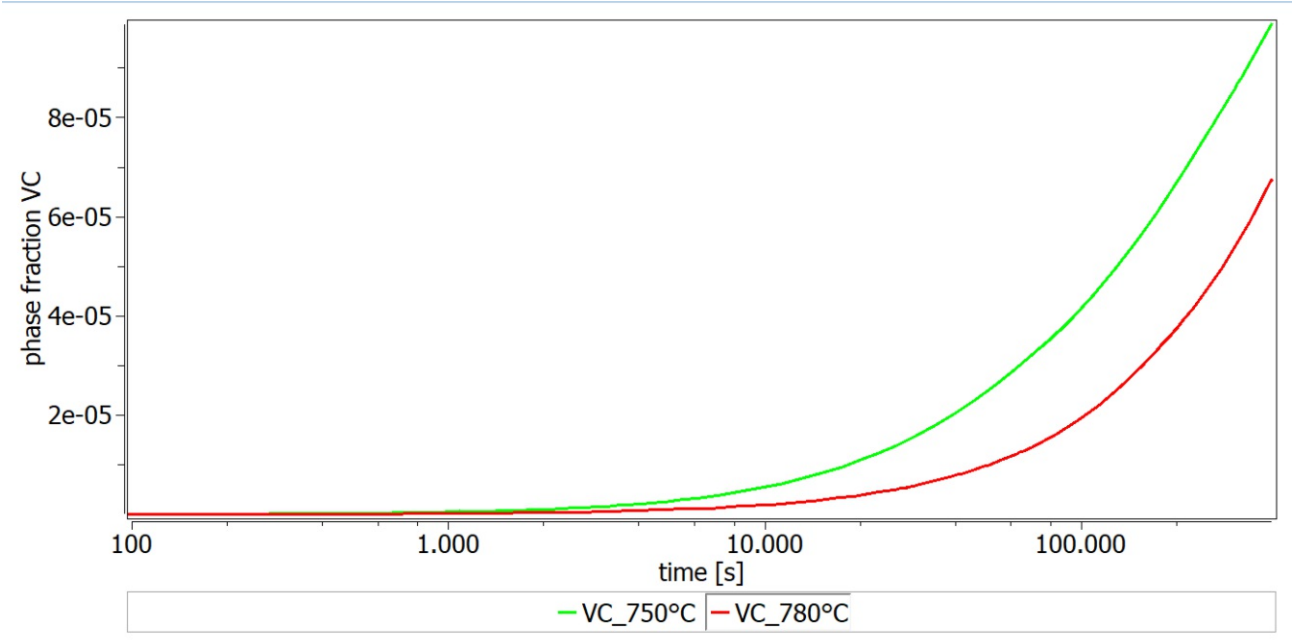

Figure 4.39: comparison of the phase fraction evolution of VC in alloy 5-2 isothermally reacted at 780°C and 750°C

account, one possible explanation for this could be due to vanadium-carbides. It is indeed interesting to see the influence of the temperature. At T_{SC} 780°C we did not see that shape, whereas at 750°C it occurred for all isothermal reaction durations.

We made a stepped equilibrium and a precipitation simulation with VC as an additional phase. All the other settings were kept as described in chapter 3.3. Following Lagneborg et al. [67] the relevant phase is VC. They [67] also stated that the solubility of VC in austenite is higher compared with other microalloying elements. Vanadium is more likely to precipitate in ferrite and does not readily precipitate in γ. The stepped equilibrium simulation did not lead to an awareness of the different behaviour depending on the temperature. Under equilibrium conditions, VC starts to form at 970°C. Figure 4.39 shows the result of the microstructure simulation.

The phase fraction of VC is higher at 750°C than at 780°C. The driving force for VC is about 5 times higher than for cementite. To surely negate the influence of V_2C_3 we made the same simulations regarding this compound. The equilibrium simulation showed that it does not become thermodynamically stable. Neither did it precipitate in the microstructure simulation. Executing a material analysis of the structure with EDX or electron energy loss spectroscopy (EELS) could provide further information.

5 Summary and Outlook

We carried out heat treatment experiments for four different alloys with two different isothermal reaction temperatures and nine different durations. We analysed the heat-treated samples in an optical and scanning electron microscope. Accompanying the physical experiments, we executed thermokinetic simulations in MatCalc, covering the same parameters and alloy compositions as for the heat treatments. The results from the evaluation in MatCalc was then evaluated with the results from the physical experiments. We tried to assess the influence of substitutional alloying elements, such as Si, Cu or Mn, on the formation of secondary cementite in reality and simulation.

Summing up the heat treatment experiments, we can say that the formation of secondary grain boundary cementite follows an exponential growth with saturation. In general, the cementite fraction increased with decreasing isothermal reaction temperature. During the examination of the micrographs, the importance of converting the SC thickness, measured in a 2D sectional plane, into 3D to achieve accurate results became apparent. The experiments showed that the initial austenite grain size affects the SC thickness but does not affect the phase fraction. We spotted a correlation between Si and discontinuity of the secondary grain boundary cementite. The alloying elements in alloy 4-1 seemed to favour a quick growth of single spots around the grains. The duration till a continuous film is built increases, compared with less complex steel concerning alloying such as FeCu1. A similar influence of Cr on the continuity can not be negated because of the for this question improper alloy composition. Regarding the retarding of coarsening of cementite growth by Cr and Mn, we can not make a clear statement, which results from the similar content of Cr and Mn of the alloys. For answering these topics more accurately, one needs to do further experiments with different alloy compositions. Our research also showed that cementite growth stopped before it reached the equilibrium fraction and that further growth stagnated after about 10000 seconds of annealing time. We did not find clear evidence for only one element causing this behaviour, neither for a combined effect. We can say that Mn, Cr and Si play a role in terms of continuity of the grain boundary cementite and retarding the coarsening of cementite. Combining the results from the experiments in this work and the results regarding retardation by the ledge-mechanism from other authors ([44], [8], [12]), we suggested that the ledge-mechanism, at least partially, contributes to the stagnating

grain boundary cementite growth kinetics. For this work available and diffusive model provides us with good trends but does not provide accurate predictions.

The microstructure simulation for FeCu1 fitted well with the experiments until about 10000 seconds. The simulations for the other alloys showed a delay in growth till the formation started. By comparing the simulation results of alloy FeCu1 and FeCu3 it became apparent that Cu retarded the cementite formation in the simulation. The simulations for all alloys had in common that they did not stop at the level of the experiments, but exceeded by about a factor of two. Even though some retarding effect of substitutional elements on the cementite evolution has been shown also experimentally, one needs to be careful with the interpretation of the very strong simulative retardation. Further investigations are required to decipher possible reasons that may have caused this effect in the simulation. The addition or increase of substitutional alloying elements Mn and Cu lead to a retardation of the secondary cementite formation in the simulation.

Further research on this topic can be done by executing additional heat treatments with different alloy compositions. Executing heat treatment experiments with a binary Iron-Carbon alloy would illustrate the actual influence of alloying elements on the SC formation. Outperforming a three-dimensional analysis of the grain boundary cementite would provide further insights into the formation mechanism of SC and allow a more accurate determination of the SC kinetics. Accomplishing a material analysis of the samples with EDX or EELS would also provide further information, especially regarding possible trajectories of alloying elements during the transformation process. The development of a simulative model treating the ledge-mechanism is ongoing work in the CDL-IPE.

Bibliography

[1] Wolfgang Weißbach, Michael Dahms, and Christoph Jaroschek. *Werkstoffkunde: Strukturen, Eigenschaften, Prüfung*. Lehrbuch. Springer Vieweg, Wiesbaden, 19., vollst. überarb. und erw. aufl. edition, 2015.

[2] Richard J. Fruehan, editor. *Steelmaking and refining volume*, volume / the AISE Steel Foundation ; 2 of *The making, shaping and treating of steel*. AISE Steel Foundation, Pittsburgh, Pa., [elektronische ressource], 11. ed. edition, 1998.

[3] P. Mayrhofer. Werkstoffkunde metallischer werkstoffe.

[4] Hans-Jürgen Bargel. *Werkstoffkunde*. Springer-Lehrbuch. Springer Vieweg, Berlin, 12., bearbeitete auflage, korrigierter nachdruck edition, 2018.

[5] F. Wever. On the influence of the elements on the polymorphism of iron. *Archiv für das Eisenhüttenwesen 2*, pages 748–793, 1928-1929.

[6] Ericsson T. *Principles of Heat treating of Steels*. ASM International, 1991.

[7] Georg Stechauner. *Simulation of precipitation in steel : von Georg Stechauner*. Wien, 2017.

[8] G. Spanos, W. T. Reynolds, and R. A. Vandermeer. The role of ledges in the proeutectoid ferrite and proeutectoid cementite reactions in steel. *Metallurgical Transactions A*, 22(6):1367–1380, 1991.

[9] R.W. Heckel and H.W. Paxton. Rates of growth of cementite in hypereutectoid steels. *Transactions of the metallurgical society of aime*, (vol. 218):pp. 799–806, 1960.

[10] worldsteel association. total production of crude steel in 2018.

[11] T. Ando and G. Krauss. The isothermal thickening of cementite allotriomorphs in a 1.5cr 1c steel. *Acta Metallurgica*, 29(2):351–363, 1981.

[12] G. Spanos* and M. V. Kral. The proeutectoid cementite transformation in steels. *International Materials Reviews*, 54(1):19–47, 2009.

[13] H.K.D.H. Bhadeshia and Robert Honeycombe, editors. *Steels: Microstructure and Properties*. Butterworth-Heinemann, s.l., 2017.

[14] H.K.D.H. Bhadeshia and Robert Honeycombe. *Steels: Microstructure and Properties*. Butterworth-Heinemann, s.l., 2017.

[15] H. K. D. H. Bhadeshia. Cementite. *International Materials Reviews*, 65(1):1–27, 2020.

[16] M.V Kral and G. Spanos. Three-dimensional analysis of proeutectoid cementite precipitates. *Acta Materialia*, 47(2):711–724, 1999.

[17] H. I. Aaronson. The decomposition of austenite by diffusional processes. *Interscience*, pages 387–546, 1962.

[18] C. A. Dube, H. I. Aaronson, and R. F. Mehl. La formation de la ferrite proeutectoïde dans les aciers au carbone. *Revue de Métallurgie*, 55(3):201–210, 1958.

[19] K. D. Clarke. Austenite formation and microstructural control in low-alloy steels. In Saleem Hashmi, editor, *Comprehensive Materials Processing*, pages 345–361. Elsevier Science, Burlington, 2014.

[20] Eberhard Roos, Karl Maile, and Michael Seidenfuß. *Werkstoffkunde für Ingenieure: Grundlagen, Anwendung, Prüfung*. Lehrbuch. Springer Vieweg, Berlin, 6., ergänzte und bearbeitete auflage edition, 2017.

[21] R. Dabrowski. New high hardness mn-cr-mo-v tool steel. *Archives of Metallurgy and Materials*, (52(1)):87–92, 2007.

[22] K. H. Jürgen Buschow. *Encyclopedia of materials: Science and technology*. Elsevier, Amsterdam, 2001.

[23] Kirsten Bobzin. *Oberflächentechnik für den Maschinenbau*. Wiley-VCH, Weinheim, 1. aufl. edition, 2013.

[24] S. Ashida. Effect of cobalt addition on hypereutectoid steel wire transf ormation behavior and drawability of yutaka kanetsuk. 2001.

[25] K. Han, T. D. Mottishaw, G.D.W. Smith, D. V. Edmonds, and A. G. Stacey. Effects of vanadium additions on microstructure and hardness of hypereutectoid pearlitic steels. *Materials Science and Engineering: A*, 190(1-2):207–214, 1995.

[26] Guo-Hong Zhang, Jae-Yong Chae, Kwan-Ho Kim, and Dong Woo Suh. Effects of mn, si and cr addition on the dissolution and coarsening of pearlitic cementite during intercritical austenitization in fe-1mass%c alloy. *Materials Characterization*, 81:56–67, 2013.

[27] Taira NAKANO, Hiroshi KAWATANI, and Shushi KINOSHITA. Effects of chromium, molybdenum and vanadium on spheroidization of carbides in 0.8% carbon steel. *Transactions of the Iron and Steel Institute of Japan*, 17(2):110–115, 1977.

[28] J. M. Beswick. The effect of chromium in high carbon bearing steels. *Metallurgical Transactions A*, 18(11):1897–1906, 1987.

[29] Kwan-Ho Kim, Jae-Seung Lee, and Duk-Lak Lee. Effect of silicon on the spheroidization of cementite in hypereutectoid high carbon chromium bearing steels. *Metals and Materials International*, 16(6):871–876, 2010.

[30] E. Kozeschnik and H. K. D. H. Bhadeshia. Influence of silicon on cementite precipitation in steels. *Materials Science and Technology*, 24(3):343–347, 2008.

[31] H. L. Yi, Z. Y. Hou, Y. B. Xu, D. Wu, and G. D. Wang. Acceleration of spheroidization in eutectoid steels by the addition of aluminum. *Scripta Materialia*, 67(7-8):645–648, 2012.

[32] François E. Cellier. *Continuous system modeling*. Springer, New York and Berlin, 1991.

[33] Adolf Fick. Ueber diffusion. *Annalen der Physik und Chemie*, 170(1):59–86, 1855.

[34] Alfred B. Pippard. *Elements of classical thermodynamics: For advanced students of physics*. Univ. Pr, Cambridge, repr edition, 1981.

[35] M. Hillert and J. Ågren. On the definitions of paraequilibrium and orthoequilibrium. *Scripta Materialia*, 50(5):697–699, 2004.

[36] H. K. D. H. Bhadeshia and J. W. Christian. Bainite in steels. *Metallurgical Transactions A*, 21(3):767–797, 1990.

[37] E. Kozeschnik. *Modeling Solid-state Precipitation*. Momentum Press, 2013.

[38] Jeremy R. H. Tame. *Approaches to Entropy*. Springer Singapore, Singapore, 2019.

[39] H. L. Lukas, Bo Sundman, and Suzana G. Fries. *Computational thermodynamics: The CALPHAD method*. Cambridge University Press, Cambridge, 2007.

[40] M. Hillert. The role of interfacial energy during solid-state phase transformations. *Jernkontorets Annaler*, 141:757–789, 1957.

[41] C. ZENER. Kinetics of the decomposition of austenite. *Trans. AIME*, 167:550–595, 1946.

[42] John W. Cahn, W.B Hillig, and G.W Sears. The molecular mechanism of solidification. *Acta Metallurgica*, 12(12):1421–1439, 1964.

[43] HI Aaronson, C Laird, KR Kinsman. *Phase transformations: ASM, Metals Park, OH, 1970*. 1970.

[44] G. Krauss T. Ando. Solid-solid phase transformations: (eds. h. i. aaronson et al.). *TMS-AIME*, pages 573–577, 1982.

[45] Struers. metallographical analysis.

[46] Günter Petzow and Veronika Carle. *Metallographisches, keramographisches, plastographisches Ätzen*, volume 1 of *Materialkundlich-technische Reihe*. Borntraeger, Berlin, nachdr. der 6., vollst. überarb. aufl. edition, 2006.

[47] Image J. Wayne Rasband. Imagej.

[48] Drawboard Pty Ltd. Drawboard pdf.

[49] Robert L. Fullman. Aime 1993. In *Trans*, volume vol. 197, page p.447.

[50] M. Vogric, E. Kozeschnik, J. Svoboda, S. Zamberger, W. Wei, E. Povoden-Karadeniz, unpublished research. *State of the art of grain boundary cementite modeling*. PhD thesis, 2020.

[51] Zoch Macherauch, Zoch, Macherauch and Eckard Macherauch. Korngrößenermittlung. In *Praktikum in Werkstoffkunde*, pages 75–81.

[52] E04 Committee. Astm-e112-2010 test methods for determining average grain size, 2010.

[53] Matcalc, https://www.matcalc.at/start/.

[54] Thermo-calc, https://thermocalc.com/.

[55] E. Povoden-Karadeniz. Thermodynamic database mc_fe_v2.060.tdb, 2016.

[56] E. Povoden-Karadeniz. Mobility database mc_fe_v2.060.tdb, 2018.

[57] Bruno Predel, Michale Hoch, and Monte Pool. *Phase diagrams and heterogeneous equilibria: A practical introduction*. Engineering materials and processes. Springer, Berlin, 2004.

[58] Kozeschnik E., et al. Matcalc – a simulation tool for multicomponent thermodynamics, diffusion and phase transformation kinetics. In *Mathematical Modelling of Weld Phenomena*, pages pp. 349–361.

[59] E. Kozeschnik, J. Svoboda, R. Radis, and F. D. Fischer. Mean-field model for the growth and coarsening of stoichiometric precipitates at grain boundaries. *Modelling and Simulation in Materials Science and Engineering*, 18(1):015011, 2010.

[60] E. Kozeschnik. Techpaper #2011002: Treatment of heterogeneous nucleation, 2011.

[61] E. Kozeschnik. Techpaper #2011004: Diffusion in heterogeneous precipitation, 2011.

[62] Eckard Macherauch and Hans-Werner Zoch. Praktikum in werkstoffkunde: 91 ausführliche versuche aus wichtigen gebieten der werkstofftechnik, 2011.

[63] T. Gladman. *The physical metallurgy of microalloyed steels*, volume 792 of *Book / The Institute of Materials*. Maney, London, 2002.

[64] Mehran Maalekian. *The Effects of Alloying Elements on Steels (I)*. PhD thesis, Technische Universität Graz, Graz, October 2007.

[65] P. Warczok. Techpaper #2014001: Evaluation of interfacial energies, 2014.

[66] Ernst Kozeschnik and John M. Vitek. Ortho-equilibrium and para-equilibrium phase diagrams for interstitial / substitutional iron alloys. *Calphad*, 24(4):495–502, 2000.

[67] R. Lagneborg, T. Siwecki, S. Zajc, and B. Hutchinson. The role of vanadium in microalloyed steels. *Scandinavian Journal of Metallurgy*, 28:186–241, 1999.

Appendix

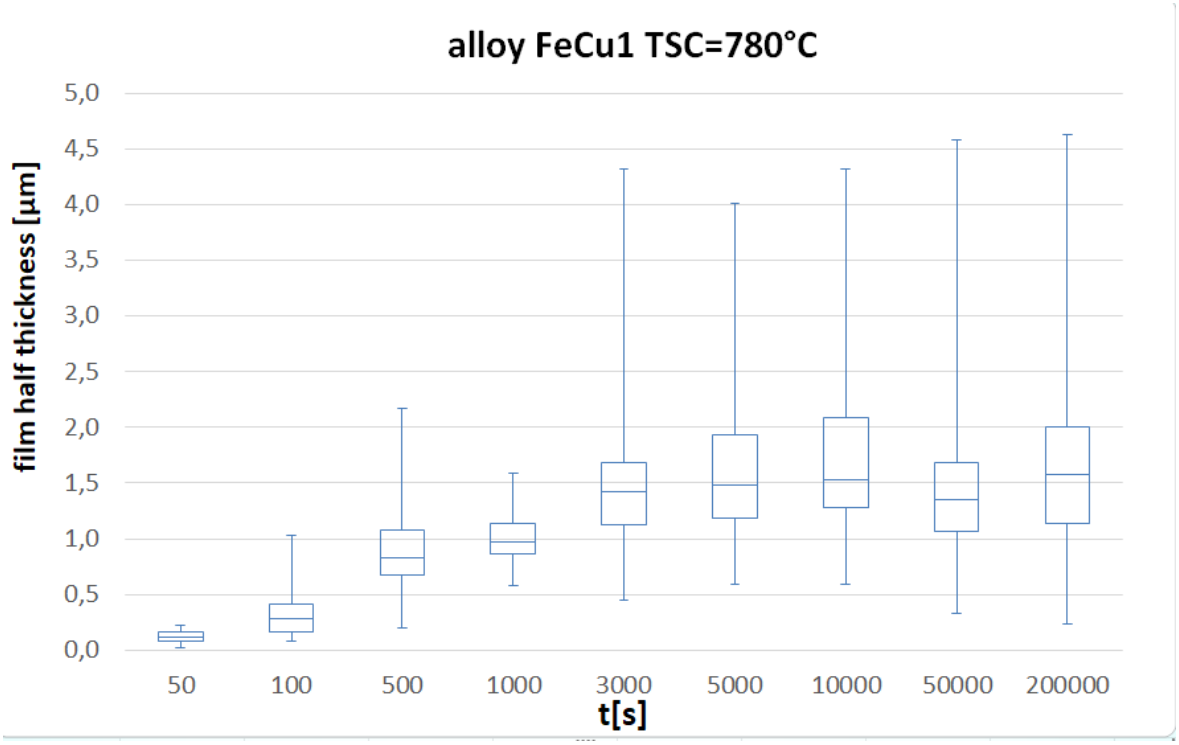

Figure 5.1: secondary cementite half thickness of alloy FeCu1 at 780°C plotted as box-plot graph

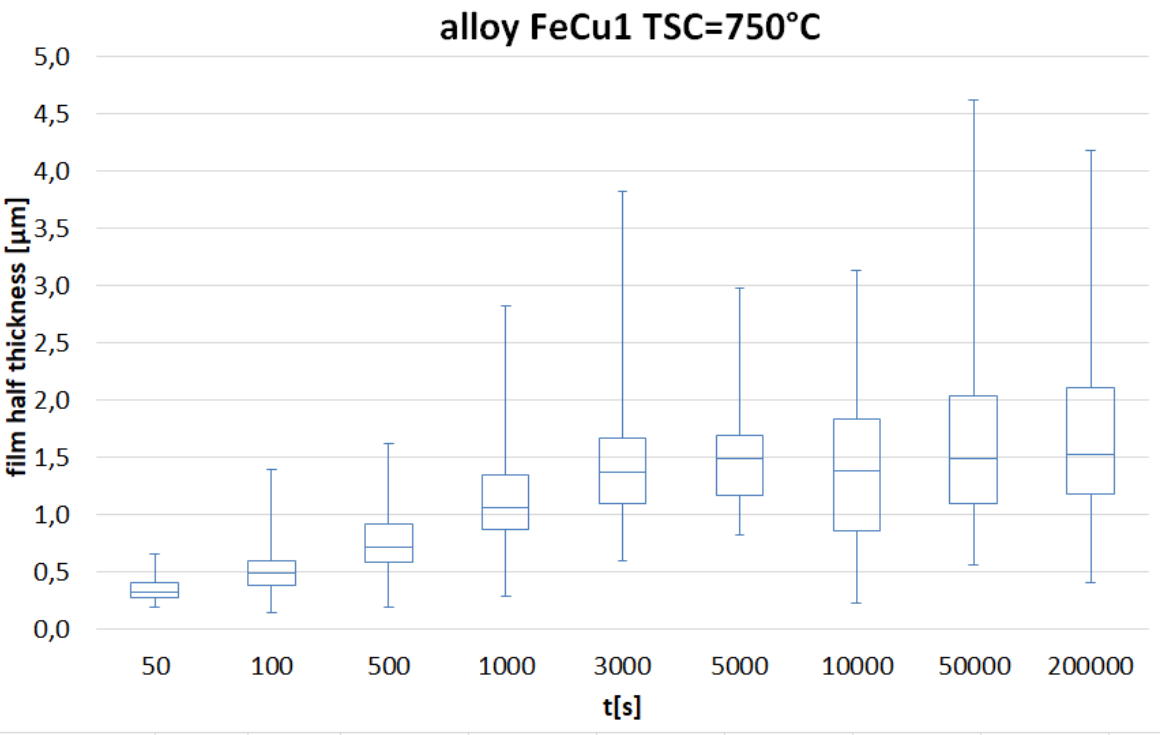

Figure 5.2: secondary cementite half thickness of alloy FeCu1 at 750°C plotted as boxplot graph

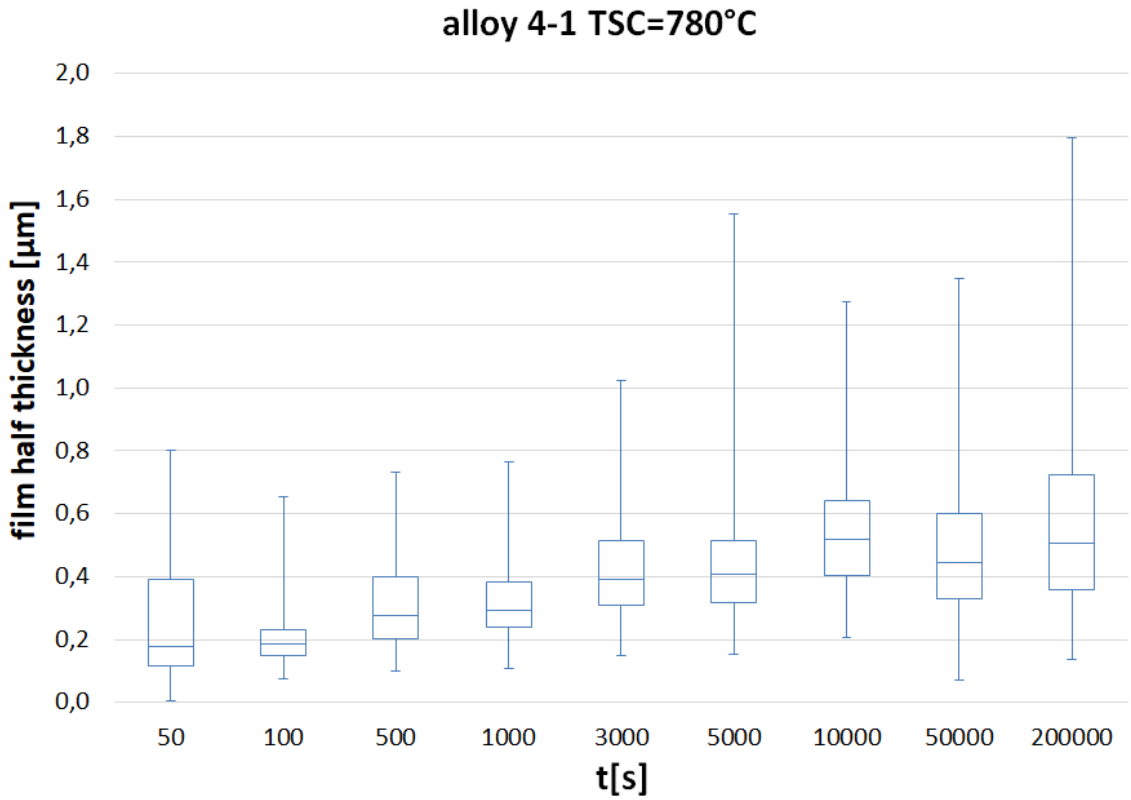

Figure 5.3: secondary cementite half thickness of alloy 4-1 at 780°C plotted as boxplot graph

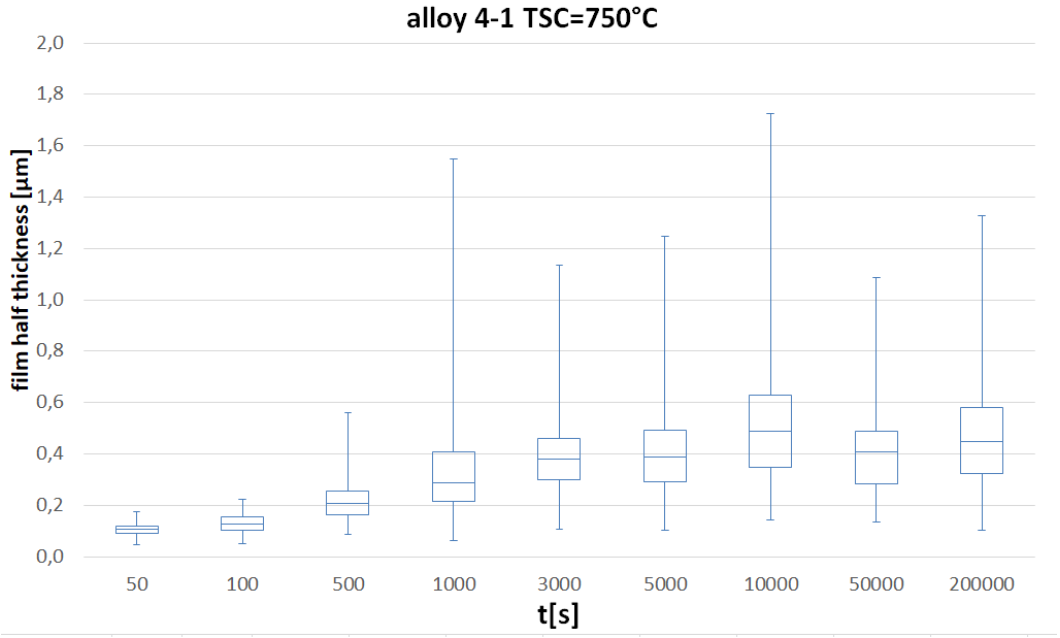

Figure 5.4: secondary cementite half thickness of alloy 4-1 at 750°C plotted as boxplot graph

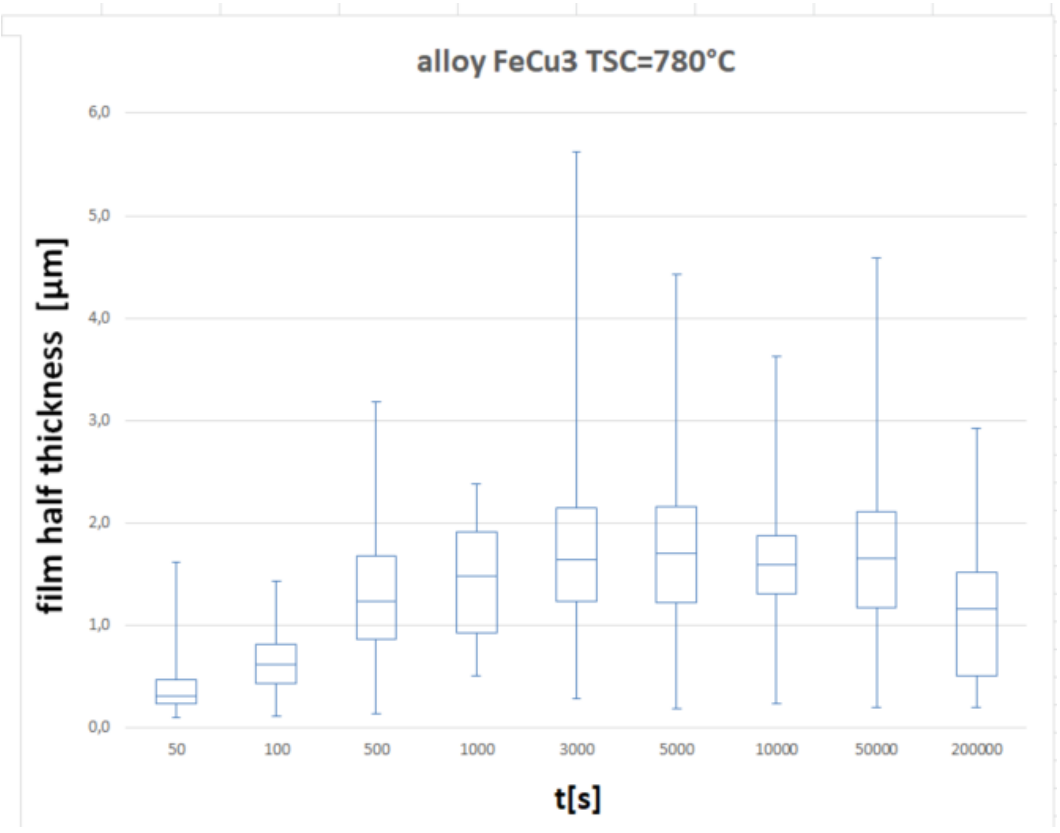

Figure 5.5: secondary cementite half thickness of alloy FeCu3 at 780°C plotted as boxplot graph

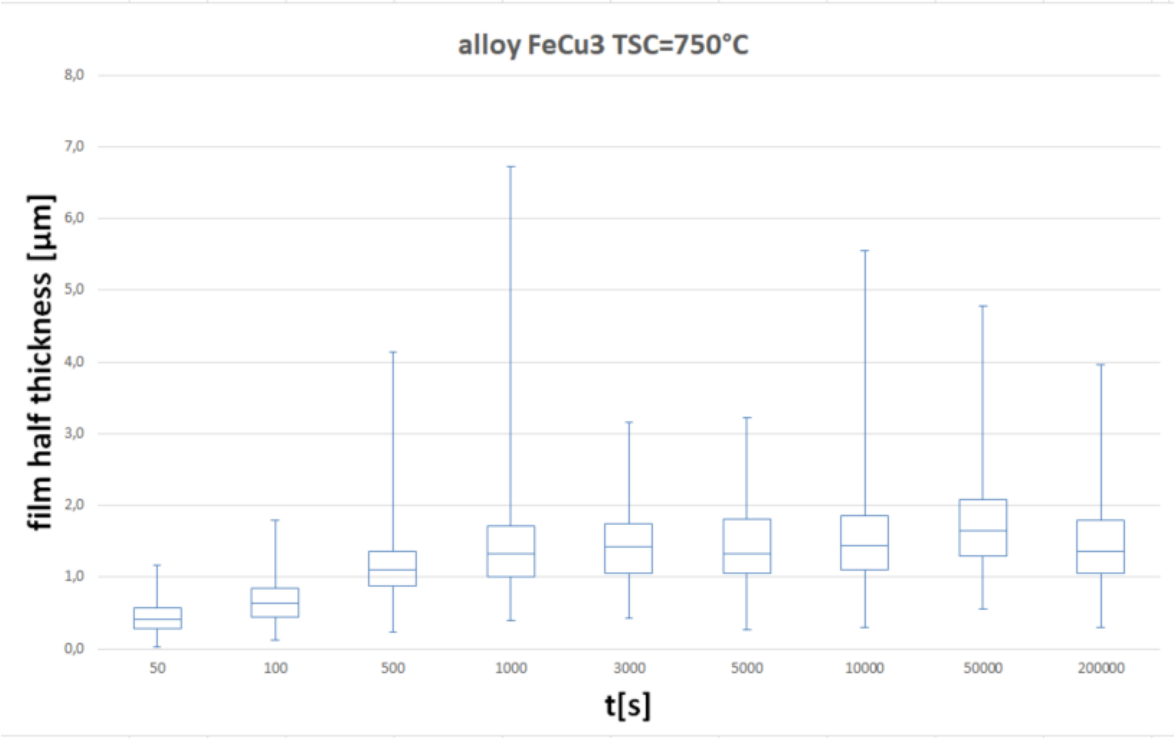

Figure 5.6: secondary cementite half thickness of alloy FeCu3 at 750°C plotted as boxplot graph

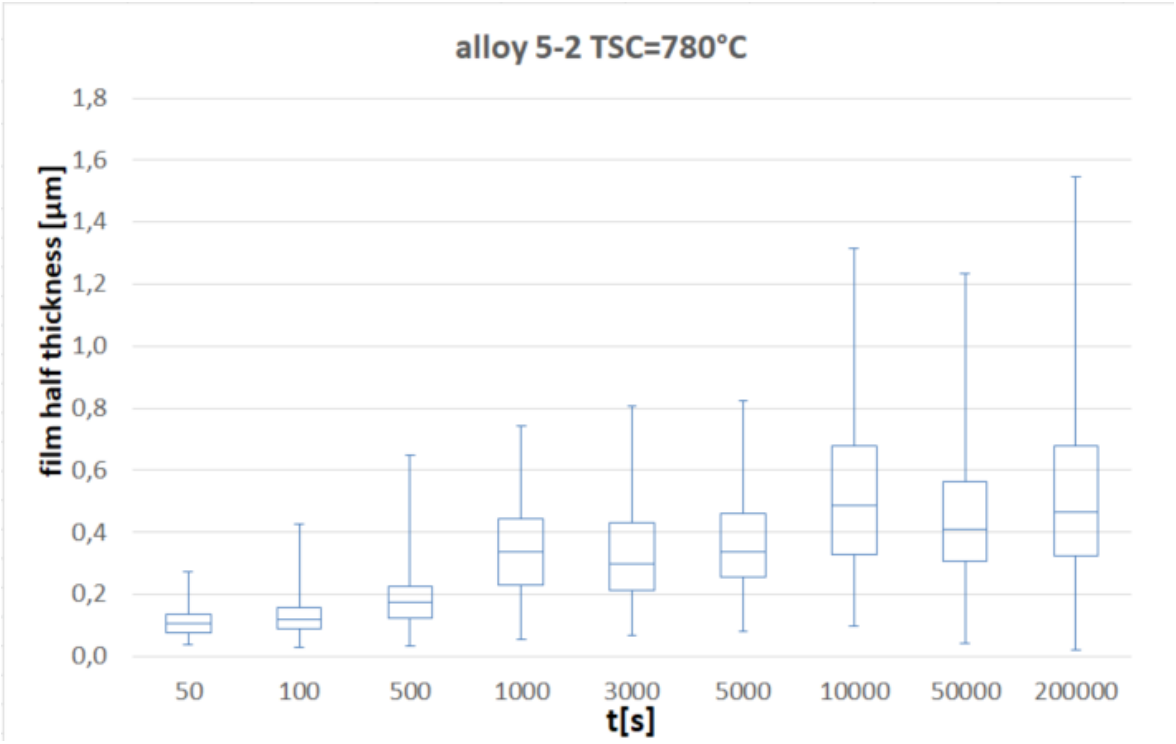

Figure 5.7: secondary cementite half thickness of alloy 5-2 at 780°C plotted as boxplot graph

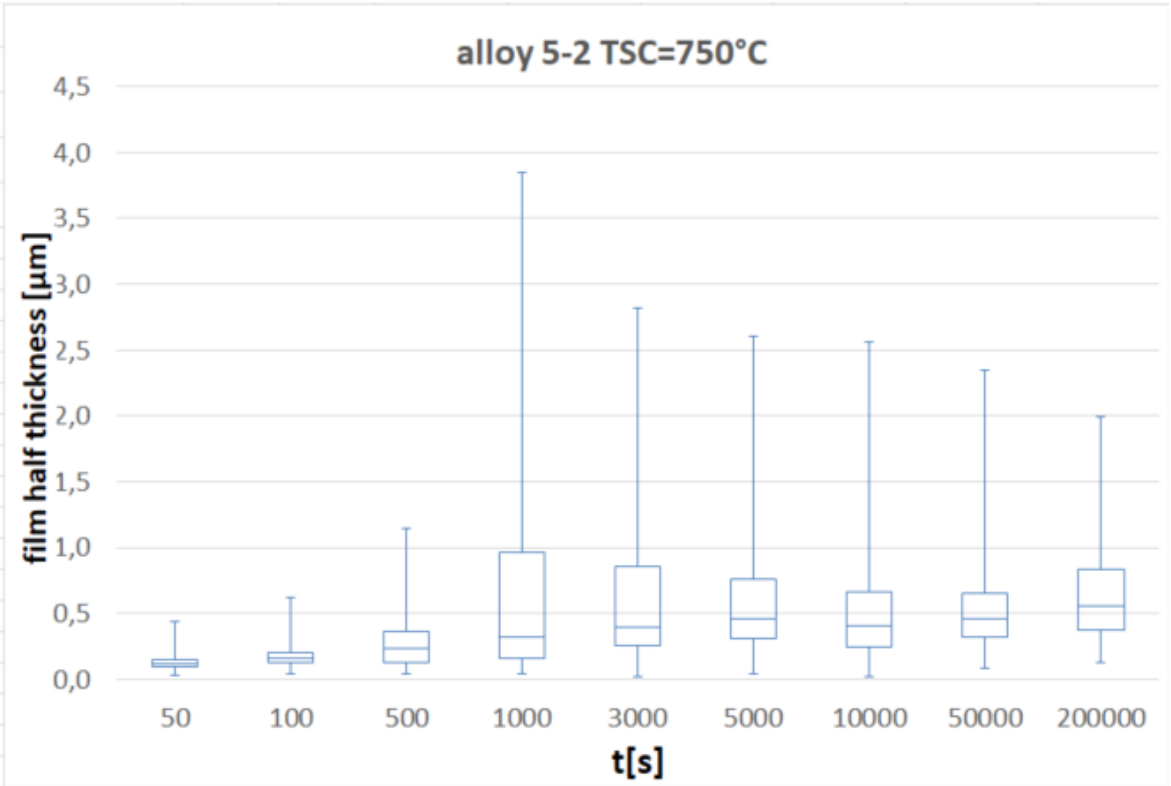

Figure 5.8: secondary cementite half thickness of alloy 5-2 at 750°C plotted as boxplot graph

Table 5.1: listing of all executed experiments, part 1

Nr	T_{aust}[s]	t_{aust}[s]	$\frac{dt}{dt1}$[K/s]	T_{SC}[°C]	t_{SC}[s]	$\frac{dt}{dt2}$[K/s]	sample	note
1	1050	1800	70	800	500	70	4-1/A1b	pretest
2	1050	1800	70	800	500	70	4-1/A1a	
3	1050	1800	70	800	500	70	FeCu1/bA3α	
4	1050	1800	70	800	500	70	FeCu1/bA3γ	
5	1050	1800	70	800	500	70	FeCu1/bA3δ	
6	1050	1800	100	800	500	100	FeCu1/bA1α	
7	1050	1800	100	800	500	100	FeCu1/bA1β	
8	950	1800	100	800	500	100	FeCu1/bA1γ	
9	950	1800	100	800	700	100	FeCu1/bA1δ	
10	950	1800	100	800	1000	100	FeCu1/bA5α	
11							FeCu1/bA5β	
12	950	1800	75	800	1200	100	FeCu1/bA5γ	
13							FeCu1/bA5δ	
14	950	1800	40	800	1200	100	FeCu1/b2Bα	
15							2-1/A5a	
16	950	1800	30	780	1200	100	FeCu1/bB2γ	
17	950	1800	30	800	1000	100	FeCu1/bB2δ	
18	950	1800	30	800	1000	100	4-1/A5a	
19	950	1800	15	780	500	100	FeCu1/b4Bα	
20	950	1800	15	780	300	100	FeCu1/b4Bβ	
21	950	1800	15	780	5000	100	FeCu1/b6Bγ	
22	950	1800	15	780	100	100	FeCu1/b4Bδ	
23	950	1800	15	780	10000	100	FeCu1/b6Bα	
24	950	1800	15	780	10	100	FeCu1/b6Bβ	
25	950	1800	15	780	1000	100	FeCu1/b4Bγ	
26	950	1800	15	780	5000	100	FeCu1/b6Bδ	
27	950	1800	15	750	1000	100	FeCu1/bB1α	
28	950	1800	15	750	3000	100	FeCu1/bB1β	
29	950	1800	15	750	500	100	FeCu1/bB1γ	
30	950	1800	15	750	5000	100	FeCu1/bB3δ	
31	950	1800	15	750	100	100	FeCu1/bB3α	
32	950	1800	15	750	10000	100	FeCu1/bB3β	
33	950	1800	15	750	50	100	FeCu1/bB3γ	
34	950	1800	15	780	1000	100	4-1 a3A	
35	950	1800	15	780	3000	100	4-1 b3A	
36	950	1800	15	780	500	100	4-1 b5A	
37	950	1800	15	780	5000	100	4-1 a2A	
38	950	1800	15	780	100	100	4-1 a4A	
39	950	1800	15	780	10000	100	4-1 a6A	
40	950	1800	15	780	50	100	4-1 b2A	
41	950	1800	15	750	1000	100	4-1 b4A	
42	950	1800	15	750	3000	100	4-1 b6A	
43	950	1800	15	750	500	100	4-1 a2B	

Table 5.2: listing of all executed experiments, part 2

Nr	T_{aust}[s]	t_{aust}[s]	dt/dt1[K/s]	T_{SC}[°C]	t_{SC}[s]	dt/dt2[K/s]	sample	note
44	950	1800	15	750	5000	100	4-1 a4B	
45	950	1800	15	750	100	100	4-1 a6B	
46	950	1800	15	750	10000	100	4-1 b2B	
47	950	1800	15	750	50	100	4-1 b4B	
48	950	1800	15	780	3000	100	FeCu1/bB5α	
49	950	1800	15	780	50000	100	FeCu1/b1Bδ	
50	950	1800	15	750	50000	100	FeCu1/b5Bβ	
51	950	1800	15	780	200000	100	FeCu1/bB5γ	
52	950	1800	15	750	200000	100	FeCu1/bB5δ	
53	950	1800	15	780	50000	100	4-1 a1B	
54	950	1800	15	750	50000	100	4-1 a3B	
55	950	1800	15	780	200000	100	4-1 b1B	
56	950	1800	15	750	200000	100	4-1 b3B	
57	950	1800	15	780	3000	100	FeCu1/b2Aα	
58	950	1800	15	780	50000	100	FeCu1/b2Aβ	
59	950	1800	15	780	50000	50000	4-1 a5B	
60	950	1800	15	780	50000	50000	4-1 b5B	
61	950	1800	15	780	50000	100	FeCu1/b2Aγ	
62	950	1800	15	780	1000	100	5-2 b1A	
63	950	1800	15	780	3000	100	5-2 b1B	
64	950	1800	15	780	500	100	5-2 b1C	
65	950	1800	15	780	5000	100	5-2 b1D	
66	950	1800	15	780	100	100	5-2 b2A	
67	950	1800	15	780	10000	100	5-2 b2B	
68	950	1800	15	780	10000	100	5-2 a4B	t_H=6h
69	950	1800	15	780	10000	100	5-2 a6B	t_H=6h
70	950	1800	15	780	50	100	4-1 b2C	
71	950	1800	15	750	1000	100	5-2 b2D	
72	950	1800	15	750	3000	100	5-2 b3B	
73	950	1800	15	750	500	100	5-2 b3C	
74	950	1800	15	750	5000	100	5-2 b4A	
75	950	1800	15	750	100	100	5-2 b4B	
76	950	1800	15	750	10000	100	5-2 b3D	
77	950	1800	15	750	50	100	5-2 b4C	
78	950	1800	15	780	1000	100	FeCu3/bA1α	
79	950	1800	15	780	3000	100	FeCu3/bA1β	
80	950	1800	15	780	500	100	FeCu3/bA1γ	
81	950	1800	15	780	5000	100	FeCu3/bA1δ	
82	950	1800	15	780	100	100	FeCu3/bA3α	
83	950	1800	15	780	10000	100	FeCu3/bA3γ	
84	950	1800	15	780	50	100	FeCu3/bA3δ	
85	950	1800	15	750	1000	100	FeCu3/bA5α	

Table 5.3: listing of all executed experiments, part 3

Nr	T_{aust}[s]	t_{aust}[s]	dt/dt1[K/s]	T_{SC}[°C]	t_{SC}[s]	dt/dt2[K/s]	sample	note
86	950	1800	15	750	3000	100	FeCu3/bA5β	
87	950	1800	15	750	500	100	FeCu3/bA5γ	
88	950	1800	15	750	5000	100	FeCu3/bA5δ	
89	950	1800	15	750	100	100	FeCu3/bA2α	
90	950	1800	15	750	10000	100	FeCu3/bA2β	
91	950	1800	15	750	50	100	FeCu3/bA2γ	
92	950	1800	15	780	50000	100	5-2 b4D	
93	950	1800	15	780	200000	100	5-2 b5A	
94	950	1800	15	750	50000	100	5-2 b5B	
95	950	1800	15	750	200000	100	5-2 b5C	
96	950	1800	15	780	50000	100	FeCu3/bA2δ	
97	950	1800	15	780	200000	100	FeCu3/bA4α	
98	950	1800	15	750	50000	100	FeCu3/bA4β	
99	950	1800	15	750	200000	100	FeCu3/bA4γ	
100	950	1800	15	780	3000	100	FeCu3/bA4δ	
101	950	1800	15	780	200000	100	FeCu3/bA6α	
102	950	1800	15	780	10000	100	FeCu3/bA6β	

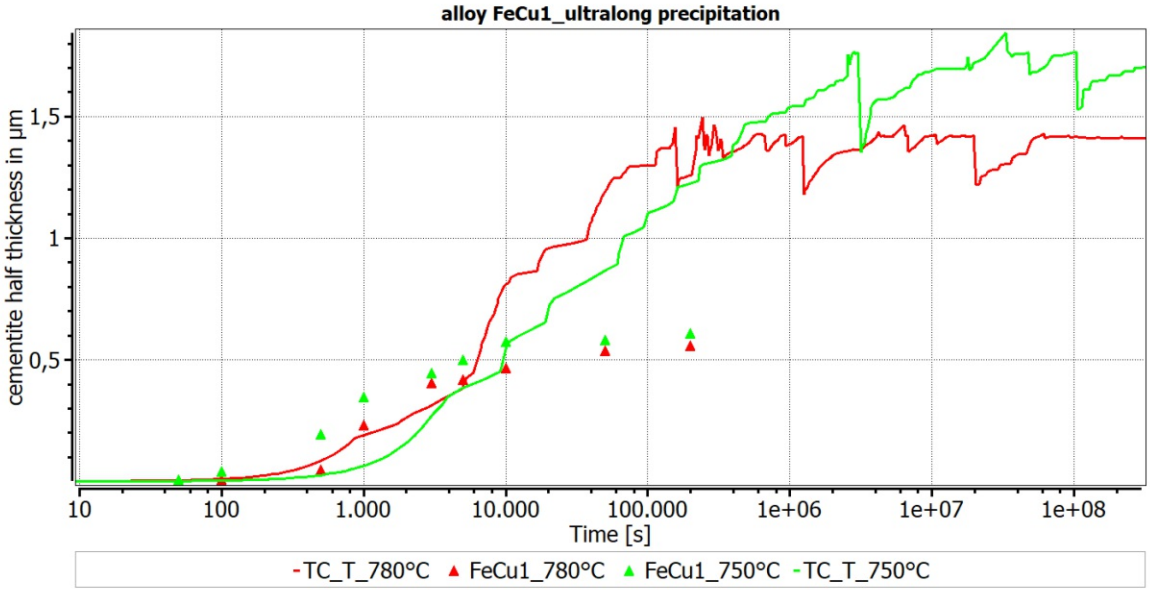

Figure 5.9: ultralong microstructure simulation of alloy FeCu1

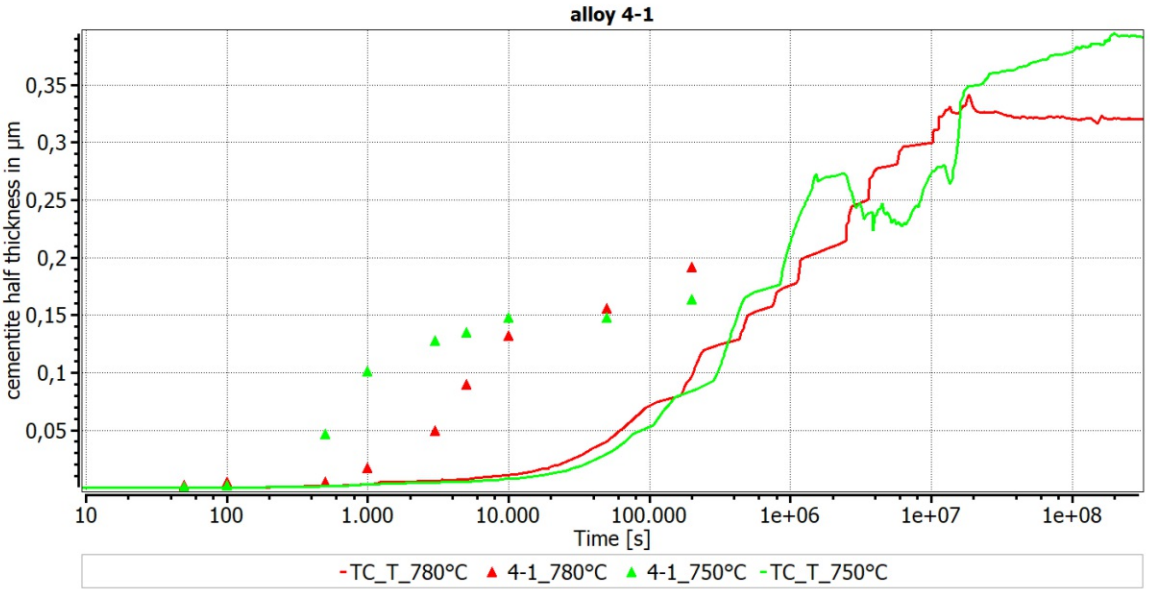

Figure 5.10: ultralong microstructure simulation of alloy 4-1

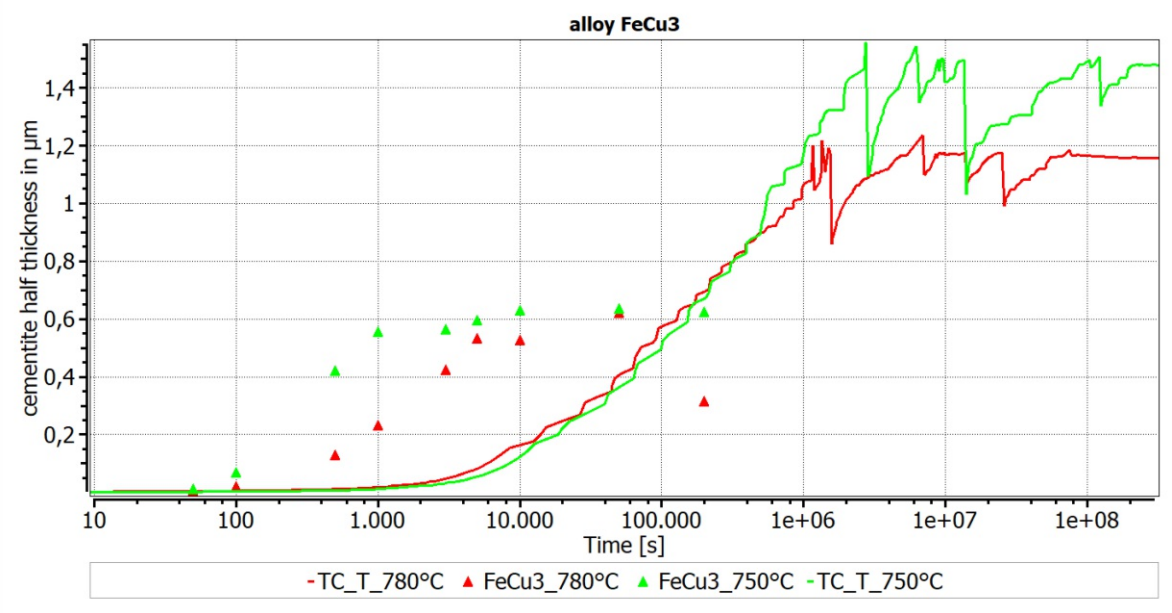

Figure 5.11: ultralong microstructure simulation of alloy FeCu3

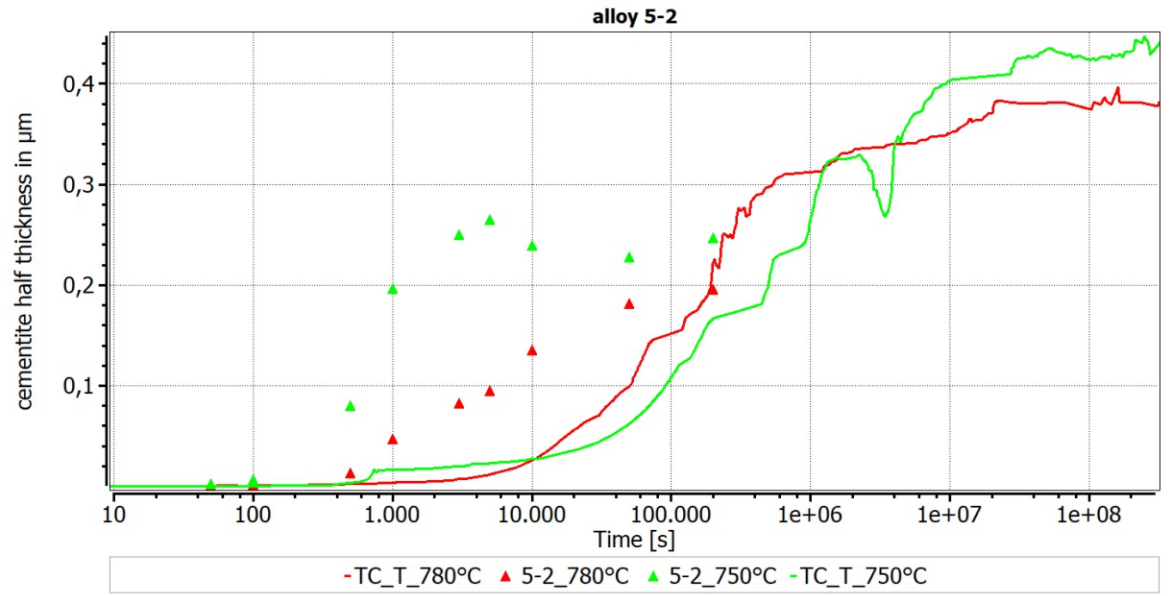

Figure 5.12: ultralong microstructure simulation of alloy 5-2

MatCalc-script

The following Script was used for the simulation in MatCalc for the cementite evolution simulation with alloy 5-2.

```
$Matcalc-Version 4.04 rel 0.049
$Script Version 1.0
$testausdruck
$This script executes a precipitation calculation to evaluate the growth
of secondary cementite.
$The simulation is carried out with alloy 5-2 at 780°C and 750°C isothermally
for 3 e+05s.
$
$$Composition in weight%
C=1.055
Cr=0.209
Mn=  1.274
Si=0.924
V=0.143
$$
$use-module core
new-workspace


@$************************************ $ enter workspace info
@$************************************
@ set-workspace-info cementite growth
@ set-workspace-info +Calculation of cementite growth
@ set-workspace-info +in alloy 5-2
@ set-workspace-info +with phases , FCC_A1 and CEMENTITE.


$************************************** SYSTEM SETUP ***********
$*****************************************************************

$$*************************************************************
DATABASES, CHEMICAL COMPOSITION, SELECTED PHASES
*************************************************************$$
```

```
open-thermodynamic-database mc_fe.tdb


open-thermodynamic-database file-name=mc_fe.tdb
select-elements elements= FE C  CR  MN  Si V
$ Components: Fe, C, Cr, Mn, Si, V
select-phases  FCC_A1 CEMENTITE
$ Phases:  austenite, cementite
read-thermodynamic-database
read-mobility-database mc_fe.ddb

set-reference-element FE
enter-composition weight-percent C=1.055 Cr=0,209  Mn=1,274 Si=0,924 V=0,143
set-automatic-startvalues
set-temperature-celsius temperature=950
calculate-equilibrium


$$**********************************************************************

setting up precipitation domains
**********************************************************************
$$

create-precipitation-domain austenite
set-precipitation-parameter  austenite thermodynamic-matrix-phase=FCC_A1


$ setting up the precipitation domain.
set-precipitation-parameter austenite equilibrium-dislocation-density=1e12
set-precipitation-parameter austenite initial-grain-diameter=50e-6
set-precipitation-parameter austenite initial-subgrain-diameter=50e-6
set-precipitation-parameter austenite subgrain-elongation-factor=1
set-precipitation-parameter austenite grain-evolution-model
=no-grain-structure-evolution

$für grain-evolution, (Korngröße nicht konstant während Simulation)
$set-precipitation-parameter austenite grain-evolution-model=single-class
```

```
$$**********************************************************************
setting up precipitation phase
**********************************************************************$$


$setting up precipitate phase
create-new-phase CEMENTITE precipitate
set-precipitation-parameter CEMENTITE_P0 number-of-size-classes=50
set-precipitation-parameter CEMENTITE_P0 nucleation-model
=classical-nucleation-theory
set-precipitation-parameter  CEMENTITE_P0 nucleation-sites=grain-boundaries
set-precipitation-parameter CEMENTITE_P0 gb-spherical-mdef=3.0
set-precipitation-parameter  CEMENTITE_P0 nucleus-composition-model
=ortho-composition
set-precipitation-parameter CEMENTITE_P0
use-heterogeneous-site-energy-in-nucleation=yes

$$**********************************************************************
Zementitdicke aus Phasenanteil und Korngrenzfläche definieren
**********************************************************************$$

$Korngrenzfläche wie im Buch von Ernst definieren
$volume of an isolated grain
set-function-expression  VSG$austenite=8*(2/(10^3))^(0,5)*(GD$austenite)^3
$surface area of an isolated grain
set-function-expression  ASG$austenite
=1/(8*(2/(10^3))^(0,5)*(GD$austenite)^3)*(1/2)*((GD$austenite^2)/10*(8+12*(3)^(0.
$Zementitdicke berechnet mit der Austenit-Korngrenzfläche nach der Formel von
Ernst Kozeschnik (Buch S. 85) über den Durchmesser der Austenitkörner GD$austenit
Anzahl der Körner (NG) auch berechnet über den Durchmesser der Austenitkörner
set-function-expression thickness$cementite=F$CEMENTITE_P0/(2*ASG$austenite)
$Alternative Berechnung der Dicke mit NG von Matcalc und AG über d (Durchmesser
set-function-expression thickness$cementite_NGMC=F$CEMENTITE_P0/(2*Grain_Area$Aus

$$**********************************************************************
GRAPHICAL OUTPUT
**********************************************************************
```

```
new-gui-window p1
$ allgemeine Einstellungen der x-Achse, für alle Plots gültig.
set-gui-window-property . default-x-axis-for-all-plots=yes
set-gui-window-property . default-x-axis-title=Time [s]
set-gui-window-property . default-x-axis-type=log
set-gui-window-property . default-x-axis-scaling=0.001..300000

set-plot-option . series new buffer T$c
set-plot-option . series rename series-index=0 new-name=T_780°C
set-plot-option . y-axis-title=Temperature [°C]
$grid linien werden eingeblendet
set-plot-option . grid major enable-x-axis=yes
set-plot-option . grid major enable-y-axis=yes

$zweites Fenster
create-new-plot xy-plot .
set-plot-option . y-axis-title=Phase fraction
set-plot-option . grid major enable-x-axis=yes
set-plot-option . grid major enable-y-axis=yes
set-plot-option 2 axis x-axis-scaling=10..300000
set-plot-option . series new buffer f$cementite_p0

set-plot-option 2 series rename series-index=0 new-name=T_780°C
$set-plot-option . series rename series-index=0 new-name=T_780°C
$set-plot-option . series rename 0 Cementite

create-new-plot xy-plot .
set-plot-option . y-axis-title=N<sub>ppt</sub> [m<sup>-3</sup>]
set-plot-option . y-axis-type=log
set-plot-option . grid major enable-x-axis=yes
set-plot-option . grid major enable-y-axis=yes
set-plot-option . series new buffer num_prec$cementite_p0
set-plot-option . series rename series-index=0 new-name=T_780°C
$set-plot-option . series rename 0 Cementite

create-new-plot xy-plot .
set-plot-option . y-axis-title=R<sub>mean</sub> [m]
set-plot-option . y-axis-type=log
```

```
set-plot-option . grid major enable-x-axis=yes
set-plot-option . grid major enable-y-axis=yes
set-plot-option . series new buffer r_mean$cementite_p0
set-plot-option . series rename series-index=0 new-name=T_780°C
$set-plot-option . series rename 0 Cementite

new-gui-window p1
$ allgemeine Einstellungen der x-Achse, für alle Plots gültig.
set-gui-window-property . default-x-axis-for-all-plots=yes
set-gui-window-property . default-x-axis-title=Time [s]
set-gui-window-property . default-x-axis-type=log
set-gui-window-property . default-x-axis-scaling=0,01..300000

set-plot-option . series new buffer thickness$cementite
set-plot-option . series rename series-index=0 new-name=TC_T_780°C  $$ TC= thickn
set-plot-option . y-axis-title=cementite half thickness in µm
set-plot-option . y-axis-factor=1e+06
set-plot-option . grid major enable-x-axis=yes
set-plot-option . grid major enable-y-axis=yes

$$*****************************************************************

Importieren von Versuchsdaten
*****************************************************************$$

$Dilatometerexperiment mit 780°C

$create-calc-buffer new-buffer-name="FeCu1_780°C "
create-global-table new-table-name=5-2_780°C
$ Creating table

$ This command imports the data from the text file
$ Specify the path, if the source data is not in the working directory
$import-global-table table-name=exp_data file-name=t0_exp_temperatures.txt
$ Angabe der Zementitfilmdicke erfolgt in 3D und Einbeziehen des Parameters G


add-table-entry table-name=5-2_780°C x-value=50 y-value=0,0020*1e-06
```

```
add-table-entry table-name=5-2_780°C x-value=100 y-value=0,0021*1e-06
add-table-entry table-name=5-2_780°C x-value=500 y-value=0,0129*1e-06
add-table-entry table-name=5-2_780°C x-value=1000 y-value=0,047*1e-06
add-table-entry table-name=5-2_780°C x-value=3000 y-value=0,0825*1e-06
add-table-entry table-name=5-2_780°C x-value=5000 y-value=0,0947*1e-06
add-table-entry table-name=5-2_780°C x-value=10000 y-value=0,1354*1e-06
add-table-entry table-name=5-2_780°C x-value=50000 y-value=0,1818*1e-06
add-table-entry table-name=5-2_780°C x-value=200000 y-value=0,1961*1e-06
$ In the current plot (".), new series with the table/experimental data
from "Exp_data" table is plotted
set-plot-option . series new table-experimental-data table-name=5-2_780°C
set-plot-option . series rename series-index=1 new-name=5-2_780°C

create-global-table new-table-name=5-2_750°C
add-table-entry table-name=5-2_750°C x-value=50 y-value=0,0022*1e-06
add-table-entry table-name=5-2_750°C x-value=100 y-value=0,0067*1e-06
add-table-entry table-name=5-2_750°C x-value=500 y-value=0,0803*1e-06
add-table-entry table-name=5-2_750°C x-value=1000 y-value=0,1966*1e-06
add-table-entry table-name=5-2_750°C x-value=3000 y-value=0,2504*1e-06
add-table-entry table-name=5-2_750°C x-value=5000 y-value=0,2649*1e-06
add-table-entry table-name=5-2_750°C x-value=10000 y-value=0,2397*1e-06
add-table-entry table-name=5-2_750°C x-value=50000 y-value=0,2276*1e-06
add-table-entry table-name=5-2_750°C x-value=200000 y-value=0,2471*1e-06

set-plot-option . series new table-experimental-data table-name=5-2_750°C
set-plot-option . series rename series-index=2 new-name=5-2_750°C

create-global-table new-table-name=phase_fraction_5-2_780
add-table-entry  table-name=phase_fraction_5-2_780  x-value=50 y-value=0
add-table-entry  table-name=phase_fraction_5-2_780  x-value=100 y-value=0
add-table-entry  table-name=phase_fraction_5-2_780  x-value=500 y-value=0,0091
add-table-entry  table-name=phase_fraction_5-2_780  x-value=1000 y-value=0,0206
add-table-entry  table-name=phase_fraction_5-2_780  x-value=3000 y-value=0,029
add-table-entry  table-name=phase_fraction_5-2_780  x-value=5000 y-value=0,0356
add-table-entry  table-name=phase_fraction_5-2_780  x-value=10000 y-value=0,0383
add-table-entry  table-name=phase_fraction_5-2_780  x-value=50000 y-value=0,0627
add-table-entry  table-name=phase_fraction_5-2_780  x-value=200000 y-value=0,065
set-plot-option 2 series new table-experimental-data
```

```
table-name=phase_fraction_5-2_780
set-plot-option 2 series rename series-index=1 new-name=5-2_780°C

new-gui-window p1
$ allgemeine Einstellungen der x-Achse, für alle Plots gültig.
set-gui-window-property . default-x-axis-for-all-plots=yes
set-gui-window-property . default-x-axis-title=Time [s]
set-gui-window-property . default-x-axis-type=log
set-gui-window-property . default-x-axis-scaling=10..300000

set-plot-option . y-axis-title= chem. potential. of C in fcc_A1 [J/mole]
set-plot-option . y-axis-type=lin
set-plot-option . y-axis-factor=1
set-plot-option . grid major enable-x-axis=yes
set-plot-option . grid major enable-y-axis=yes
set-plot-option . series new buffer  MUP$FCC_A1$C
set-plot-option . series rename series-index=0 new-name=MUP$FCC_A1$C_780°C

create-new-plot  xy-plot .
set-plot-option . y-axis-title= drving force of cementite  [J/mol]
set-plot-option . y-axis-type=lin
set-plot-option . y-axis-factor=1
set-plot-option . grid major enable-x-axis=yes
set-plot-option . grid major enable-y-axis=yes
set-plot-option . series new buffer  DFM$CEMENTITE
set-plot-option . series rename series-index=0
new-name=DFM$CEMENTITE_780°C   $driving force cementite

new-gui-window p1
$ allgemeine Einstellungen der x-Achse, für alle Plots gültig.
set-gui-window-property . default-x-axis-for-all-plots=yes
set-gui-window-property . default-x-axis-title=Time [s]
set-gui-window-property . default-x-axis-type=log
set-gui-window-property . default-x-axis-scaling=0,001..300000

set-plot-option . y-axis-title= chem. diff. coeff. of C in fcc_A1 [m^2/s]
set-plot-option . y-axis-type=lin
set-plot-option . y-axis-factor=1
```

```
set-plot-option . grid major enable-x-axis=yes
set-plot-option . grid major enable-y-axis=yes
set-plot-option . series new buffer  D$FCC_A1$C
set-plot-option . series rename series-index=0 new-name=D$FCC_A1$C_780°C

create-new-plot  xy-plot .
set-plot-option . y-axis-title= chem. diff. coeff. of Mn in fcc_A1 [m^2/s]
set-plot-option . y-axis-type=lin
set-plot-option . y-axis-factor=1
set-plot-option . grid major enable-x-axis=yes
set-plot-option . grid major enable-y-axis=yes
set-plot-option . series new buffer  D$FCC_A1$MN
set-plot-option . series rename series-index=0 new-name=D$FCC_A1$Mn_780°C


create-new-plot  xy-plot .
set-plot-option . y-axis-title= concentration of C in FCC_A1
set-plot-option . y-axis-type=lin
set-plot-option . y-axis-factor=1
set-plot-option . grid major enable-x-axis=yes
set-plot-option . grid major enable-y-axis=yes
set-plot-option . series new buffer  C$FCC_A1$C
set-plot-option . series rename series-index=0 new-name=C$FCC_A1$C_780°C
$concentration of Ci in austenite

create-new-plot  xy-plot .
set-plot-option . y-axis-title= chemical potential of element
set-plot-option . y-axis-type=lin
set-plot-option . y-axis-factor=1
set-plot-option . grid major enable-x-axis=yes
set-plot-option . grid major enable-y-axis=yes
set-plot-option . series new buffer MUP$FCC_A1$C
set-plot-option . series rename series-index=0 new-name=MUP$FCC_A1$C_780°C $


$$**********************************************************************

starting simulation 1
```

```
**********************************************************************$$

set-simulation-parameter end-time=3e+05

$für Isotherme-Simulation bei 780°C
set-simulation-parameter isothermal-temperature=780

set-simulation-parameter temperature-in-C=yes

start-precipitate-simulation

$$**********************************************************************
Simulation with 750°C, duplicating and adapting the plots for comparison
**********************************************************************$$

$duplicate and lock all series
set-gui-window-property 2 duplicate-and-lock-plot-series
set-gui-window-property 3 duplicate-and-lock-plot-series
set-gui-window-property 4 duplicate-and-lock-plot-series
set-gui-window-property 5 duplicate-and-lock-plot-series

$Umbenennen der neuen Serien nach duplicate and lock.
set-plot-option 1 series rename series-index=1 new-name=T_750°C
set-plot-option 2 series rename series-index=2 new-name=T_750°C
set-plot-option 3 series rename series-index=1 new-name=T_750°C
set-plot-option 4 series rename series-index=1 new-name=T_750°C
set-plot-option 5 series rename series-index=3 new-name=TC_T_750°C
$ TC= thickness Cementite_Grainboundary Area from ernst book
, Simulation isotherm with 750°C$
set-plot-option 6 series rename series-index=1 new-name=MUP$FCC_A1$C_750°C
set-plot-option 7 series rename series-index=1 new-name=DFM$CEMENTITE_750°C

set-plot-option 8 series rename series-index=1 new-name=D$FCC_A1$C_750°C
set-plot-option 9 series rename series-index=1 new-name=D$FCC_A1$Mn_750°C
set-plot-option 10 series rename series-index=1 new-name=C$FCC_A1$C_750°C
set-plot-option 11 series rename series-index=1 new-name=GMP$CEMENTITE_750°C

$ Experimental Data der SC phase fraction
```

```
create-global-table new-table-name=phase_fraction_5-2_750
add-table-entry  table-name=phase_fraction_5-2_750  x-value=50 y-value=0
add-table-entry  table-name=phase_fraction_5-2_750  x-value=100 y-value=0
add-table-entry  table-name=phase_fraction_5-2_750  x-value=500 y-value=0,0473
add-table-entry  table-name=phase_fraction_5-2_750  x-value=1000 y-value=0,0494
add-table-entry  table-name=phase_fraction_5-2_750  x-value=3000 y-value=0,0635
add-table-entry  table-name=phase_fraction_5-2_750  x-value=5000 y-value=0,0723
add-table-entry  table-name=phase_fraction_5-2_750  x-value=10000 y-value=0,0728
add-table-entry  table-name=phase_fraction_5-2_750  x-value=50000 y-value=0,0806
add-table-entry  table-name=phase_fraction_5-2_750  x-value=200000 y-value=0,0728
set-plot-option 2 series new table-experimental-data
table-name=phase_fraction_5-2_750
set-plot-option 2 series rename series-index=3 new-name=5-2_750°C

$*********************************************************************
$ SAVING WORKSPACE and starting simulation 2
$*********************************************************************
set-simulation-parameter end-time=3e+05

$für Isotherme-Simulation bei 750°C
set-simulation-parameter isothermal-temperature=750

set-simulation-parameter temperature-in-C=yes

start-precipitate-simulation

save-workspace  alloy5-2_cementite_prec_780°C_750°C
```